AD-A171 214 EFFECT OF HYDROGEN ON THE MECHNICAL PROPERTIES AND FRACTURE BEHAVIOR OF H..(U) ILLINOIS UNIV AT URBANA DEPT OF MATERIALS SCIENCE F ZEIDES ET AL. JUL 86 1/2

UNCLASSIFIED N00014-83-K-0468 F/G 11/6 NL

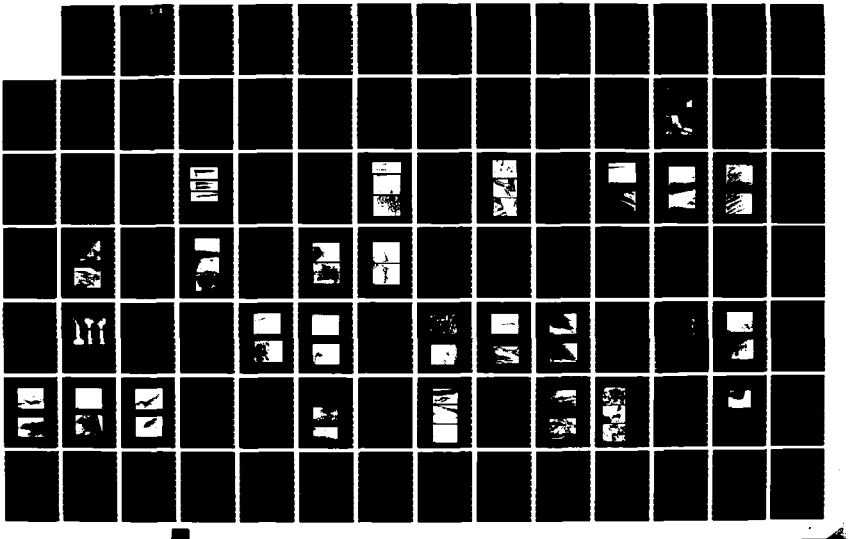

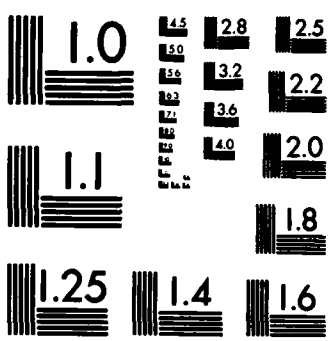

MICROCOPY RESOLUTION TEST CHART
NATIONAL BUREAU OF STANDARDS-1963-A

EFFECT OF HYDROGEN ON THE MECHANICAL PROPERTIES AND FRACTURE BEHAVIOR OF HIGH PURITY ALUMINUM

Technical Report

July 1986

Office of Naval Research
Contract N00014-83-K-0468

Felix Zeides
H.K. Birnbaum

University of Illinois
Department of Materials Science
Urbana, IL 61801

EFFECT OF HYDROGEN ON THE MECHANICAL PROPERTIES AND FRACTURE BEHAVIOR OF HIGH PURITY ALUMINUM

BY

FELIX ZEIDES

M.S., Polytechnical Institute of Tomsk, 1972

THESIS

Submitted in partial fulfillment of the requirements
for the degree of Doctor of Philosophy in Metallurgical Engineering
in the Graduate College of the
University of Illinois at Urbana-Champaign, 1986

Urbana, Illinois

Abstract

A study of hydrogen effects was conducted on 99.999% pure aluminum. Hydrogen was introduced into the material by means of a corrosion process. Two corrosive media were used; deionized pure water and an alkaline solution. The former was used for dynamic hydrogen charging during mechanical tests and the latter for hydrogen precharging. The corrosion reaction in the dynamic charging was intensified by application of weak ultrasonic oscillations.

It was found that hydrogen changed the response of the material to plastic deformation causing softening and plastic deformation localization on the macroscale and slip line coarsening as well as an increase in their waviness on the microscale. Hydrogen did not cause an earlier onset of the macroscopic plastic instability, i.e. necking.

Hydrogen modified the fracture mode changing it from a totally ductile, chisel point type to a more brittle transgranular or intergranular fracture. The fracture started only after the onset of necking. The hydrogen induced fracture modification is believed to result from the plastic deformation modification and from the effect of hydrogen on microvoid nucleation. Some fracture surfaces were covered with a film that was occasionally fragmented by a network of cracks ("mud crack pattern"). This phenomenon is believed to be a post fracture effect caused by adhesive wear between opposite fracture surfaces.

Hydrogen charging resulted in the formation of bulk vacancy clusters, a linear dimensions shrinkage and grain growth. This was interpreted as evidence for vacancy production during the corrosion reaction and for a significant hydrogen-vacancy binding enthalpy.

Acknowledgement

I sincerely thank my advisor, Professor Howard K. Birnbaum for his unfailing support, guidance and stimulation. His role in bringing this work to completion cannot be overstated.

I thank Dr. Baruch Cina of Israel Aircraft Industries, to whom I am indebted for the initial inspiration for this study.

I owe special thanks to my wife, Sophia, for her encouragement and patience, and to my children, Natalia and Dana, for their forebearance.

This research was supported by the Office of Naval Research under Contract N00014-83-K-0468 and the Department of Metallurgy and Mining Engineering.

TABLE OF CONTENTS

CHAPTER PAGE

1. INTRODUCTION

Aluminum base alloys in general and high strength aluminum alloys in particular experience premature failure when stressed in a corrosive environment. Structural parts subjected to sustained loads break at levels much lower than their designed strength. Total elongation and reduction in fracture area were decreased in slow strain tensile tests when neutral environments were changed to corrosive media. This failure process was generally considered to result from stress corrosion cracking and several possible mechanisms were offered to explain the phenomena.

In the last decade, a great deal of attention has been directed towards a hydrogen embrittlement mechanism to account for these failures. Despite the considerable evidence that hydrogen adversely influences the ductility of aluminum alloys, there is very little known about the reasons for these effects.

Most commercial aluminum alloys are very complicated systems with many significant structural parameters. Some of these important parameters are the type, size and distribution of bulk precipitates and constituent particles, the chemical composition of grain boundaries, the type, size and distribution of precipitates on grain boundaries, the width of the precipitate free zone (PFZ) adjacent to the grain boundary and the distribution of alloying elements in the PFZ, and the composition and the properties of the surface oxide. It is very difficult, if not impossible, to change one of those parameters independently of the others. Despite this, a great many attempts have been undertaken to relate the above parameters to the sensitivity of the alloy to environmental embrittlement. Based on these studies there is no doubt that variation of some of the

structural parameters affects the environmental fracture resistance. While some of these relations have been characterized, the basic mechanism of environmental fracture is not known.

Use of pure aluminum, with its inherent simplicity of structure, is very advantageous for studying the basic mechanisms of environmental embrittlement. However, except for liquid metal embrittlement, pure aluminum is generally thought to be immune to environmental embrittlement at room temperature. A goal of the present study is to demonstrate that pure aluminum is in fact sensitive to environmental embrittlement and to begin a study of the mechanism of embrittlement.

2. LITERATURE SURVEY

2.1 Hydrogen Solubility

The solubility of hydrogen in aluminum in equilibrium with the gas phase is very low when compared to other metals. There is generally good agreement in the reported data indicating that the solubility in the solid is about 1 at ppm at 660°C (the melting point) and 1 atm pressure of hydrogen gas and about ten times higher in the melt (1-4). Extrapolating the reported results to room temperature we arrive at 10^{-8} - 10^{-6} at ppm for the solid solubility in equilibrium with one atmosphere of gaseous H_2. The enthalpy of solution obtained from solubility curves are 0.41 eV, 0.67 eV, 0.67 eV and 1.52 eV from Refs. (1), (14), (64) and (4) respectively, and that theoretically derived by Larsen and Norskov (15) is 1.3 eV.

2.2 Hydrogen Diffusion

Reported values for the preexponential D_0, and activation enthalpy, ΔH, for hydrogen diffusion in high purity aluminum scatter significantly; values of D_0 range from 4.6×10^{-2} to 1.2×1^{-5} cm^2/sec and ΔH values have been reported in the range of 0.38 to 1.45 eV (4-10). The scatter band narrows considerably if the data reported by Ransley thirty years ago (6) are discarded. In this case, the range of D_0 is 4.6×10^{-2} to $1.3 \times 10^{1} cm^2/sec$ and the reported activation enthalpy values lie between 0.38 and 0.7 eV. The above data were obtained in the high temperature range, 633-898°K, using a desorption method with one exception where a permeation technique was employed (10). Extrapolating to room temperature the diffusivity is found to be 5×10^{-22} cm^2/sec from the Ransley data and in the range of 0.96×10^{-11} to 2.4×10^{-8} cm^2/sec from the other

sources. The first experimental result obtained at room temperature by permeation methods gave $2x10^{-7}$ cm^2/sec (10). It was concluded, in the study by Hashimoto (10), which used permeation methods, that the diffusion mechanism in the high temperature range differed from that near room temperature. From the fact that the diffusion coefficient obtained by extrapolation to room temperature was four orders of magnitude less than that obtained experimentally and from the observation that the observed diffusion activation enthalpy of about 0.61 eV at high temperatures was very close to that of vacancy mobility in Al, it was suggested (10) that hydrogen diffused as a H-vacancy pair in the high temperature range and as a single H interstitial atom at low temperature, i.e., near room temperature. A diffusivity of 2.2 x 10^{-10} cm^2/sec has been reported recently from a room temperature permeation study (62).

For the low purity aluminum, smaller diffusion coefficients were reported; giving D_o in the range $2x10^{-2}$ to $2.5x10^2$ cm^2/sec, and activation enthalpies ranging from 0.52 to 0.93 eV (7,11,12). Extrapolating to room temperature gives diffusion coefficients ranging from $5.8x10^{-14}$ to $4.6x10^{-12}$ cm^2/sec.

2.3 Sites for Location of H Solutes

2.3.1 Grain Boundaries

The only known direct experimental evidence concerning H interactions with grain boundaries in Al was achieved by autoradiography with tritium saturated samples (13). Tritium was preferentially located at subgrain and grain boundaries produced by high temperature metal processing. In this case, small voids were found at high tritium sites indicating that they were places where the tritium precipitated from solid solution. Fresh boundaries produced by cold work and subsequent low temperature

anneals were not deposition sites for tritium. It was concluded that the presence of impurity atoms at grain boundaries was necessary for the tritium enrichment.

In another study, hydrogen solubility reduction with grain growth was discussed (14). Interpreting their results, the authors concluded that the hydrogen binding enthalpy to the grain boundaries was about 0.15 eV.

2.3.2 Vacancies

Interaction of hydrogen with vacancies has attracted much more attention than either hydrogen-dislocation or hydrogen-grain boundary interactions. Recent theoretical calculations showed that hydrogen atoms should reside near the tetrahedral site around a vacancy with the binding energy of about 1 eV (15,16). The latest calculations show H_B(H-Vac) = 0.5 eV (78). The direct experimental evidence has been provided by the channeling technique (17). Indirect evidence for a hydrogen-vacancy interaction has been found in recent diffusion experiments (10).

The interaction of hydrogen with a group of vacancies has been shown in quenching experiments where the hydrogen presence changed the supersaturated vacancies' precipitation form from loops to voids (18).

2.3.3 Dislocations

No conclusive evidence is present for hydrogen-dislocation binding in pure aluminum. Foster et al. found using autoradiography that tritium was located along slip bands in the necked region of tensile specimens (13). However, they found numerous small voids on the grain boundaries that presumably contained all the tritium prior to the deformation. In this case, their results could be interpreted by the alignment of voids along a shear band.

Albrecht et al. considered the depth of embrittled layer in 7075 alloy after cathodic precharging with simultaneous straining and concluded that their results could be explained only by dislocation transport of hydrogen (20).

2.3.4 Voids and Bubbles

It was found by quenching and implantation experiments that the presence of hydrogen (or helium) in the lattice is necessary for void formation (21-23). In all these reports vacancy supersaturation is assumed as a pre-condition to the void nucleation. Low dose helium injection (0.1, 1.0, 10 appm) alone did not cause any void formation whereas a subsequent aluminum ion bombardment gave rise to void formation at all three helium concentrations (23). The effect of temperature on the void size and distribution was consistent with homogeneous nucleation; void size increased and void density decreased with increases in the temperature (23,24). In no case have dislocations punched out from the voids been reported. However, high pressure hydrogen bubbles have been reported to occur at grain boundary precipitates in high strength aluminum alloys (52). In this case, hydrogen bubble formation and subsequent dislocation injection into the surrounding matrix occurred under the action of an electron beam of the transmission electron microscope.

An important piece of evidence has been reported in quenching experiments by Shimomura et al. (18). They found that the concentration of voids was proportional to the square root of the hydrogen partial pressure in the gas atmosphere (hydrogen-helium mixture). This result suggests that a single hydrogen atom at a vacancy cluster enabled the void to nucleate.

2.3.5 Hydrides

Aluminum and hydrogen form AlH and AlH_3 hydrides but only AlH_3 is known to exist in a solid form (25). It has been reported in polymeric and crystalline forms (25). The crystalline form has been identified as hexagonal with lattice dimensions a = 4.449 A and c = 11.804 A (25). The hydride is unstable and very slowly decomposes into the elements at room temperature. The rate of decomposition increases with temperature and in the presence of irradation by γ, x-rays or electrons. It takes about 200 min to decompose commercially available AlH_3 powder at 140°C and only 10 min when the AlH_3 is γ-ray preirradiated (26). The hydride decomposes in 20-50 sec in the transmission electron microscope (27).

In two cases, the hydride has been reported to form in solid aluminum supersaturated with hydrogen. In the first case, hydrogen (deuterium) was introduced in high purity aluminum by ion bombardment (28). While additional x-ray diffraction peaks were ascribed to AlH_3 the authors reported lattice parameters of a = 2.90 A and c = 4.55 A which are different from those determined for AlH_3. In the second case, AlH_3 was reported to occur on the fracture surface of an Al-Zn-Mg alloy precharged with hydrogen and broken in argon (29). In this case, the hydride lattice parameters were again found to be a = 2.90 A and c = 4.55 A as in the first case. The surface layer believed to be the hydride was fragmented by a crack network in the pattern commonly observed on the stress corrosion fracture surface of 7XXX aluminum alloys and which is known as the "mud crack pattern." Other researchers suggest, however, that the fragmented layer is composed of aluminum hydroxide (54).

2.4 Environmentally-Assisted Embrittlement

The term "brittleness" as used in this paper refers to the deformation which accompanies the fracture process rather than the total strain to failure. Furthermore, its use refers to the degree of general deformation which accompanies fracture rather than the microscopic deformation localized at the crack tip.

The amount of macroscopic plastic deformation which is exhibited by a specimen can be divided in two parts; that which precedes crack nucleation and that which occurs during crack propagation. In recent years most efforts have focussed on the latter part, probably due to its importance in the prevention of catastrophic types of failure of structural parts and due to the modern design philosophy which assumes the preexistence of microcracks in the structural parts.

As a result of being exposed to some specific environments, metallic materials often exhibit premature fracture related to environmentally enhanced embrittlement. Such types of fracture as stress corrosion cracking (SCC) and liquid metal embrittlment (LME) need specific corrosive environments while hydrogen embrittlement (HE) is directly related to the presence of hydrogen regardless of the environment from which it is derived. An operating mechanism has not been well established in any of the three types of environmentally related fracture and in fact there may be several operative mechanisms in each case.

Stress corrosion cracking was commonly related to a dissolution process at the crack tip; however, the possible role of absorbed hydrogen received much recent attention (30). In the case of liquid metal embrittlement, the possible role of the adsorbed liquid metal was attributed either to reduction

in the cohesive energy or to the enhancement and localization of plastic flow at the crack tip (31). Similarly, hydrogen embrittlement in non hydride forming metals is assumed to result either from cohesive strength reduction (32) or enhanced crack tip plasticity (33). Direct evidence for the latter has been obtained lately in the in-situ experiments (34-37). In hydride forming metals, the embrittlement is caused by the hydride precipitation at the crack tip (38).

2.4.1 Environmentally-Assisted Embrittlement in Aluminum and its Alloys

2.4.1.1 Liquid Metal Embrittlement

Aluminum and its alloys are sensitive to liquid metal embrittlement in specific metals. Liquid gallium was shown to penetrate along grain boundaries and cause total disintegration of pure aluminum even in the absence of applied load (39). Liquid mercury acts in a similar but much less severe manner and reduces overall ductility from 76% to 54% (40). Lynch investigated LME in monocrystals of Al-6%Zn-3%Mg alloy and found it purely mechanical in nature (41). The fractures were cleavage-like, macroscopically parallel to {100} planes and propagated in <110> directions. Extensive slip was found to occur at the crack tip on {111} planes intersecting the cracks. The fracture surface was shown to be composed of shallow dimples. These observations provided support for the mechanism according to which the adsorbed liquid metal species reduces the shear strength and induces localized slip at the crack tip resulting in a locally duct fracture.

2.4.1.2 Stress Corrosion Cracking

Stress corrosion cracks have never been reported for pure aluminum. For a long time the preferential anodic dissoluton mechanism dominated the

explanations of SCC in aluminum alloys (42). Plastic deformation was incorporated into this mechanism as a factor causing fracture of the passive film (30). In the last 10-15 years, however, a great deal of attention has been directed towards a hydrogen embrittlement approach. Such findings as reversible embrittlement, high sensitivity to the loading mode, occurrence of brittle cracks at low moisture levels which are unable to cause a condensate at a crack tip, and hydrogen liberation from preembrittled alloys broken in vacuum provided evidence for a possible role of hydrogen in stress corrosion process (19,43-45). The role of corrosion processes, according to this approach, is merely to provide hydrogen at the metal surface. The fact that SCC still occurs in the loading mode III (pure torsion), although with much less severity than in the mode I (pure tension), is taken as evidence that anodic dissolution is possible and may be the dominant mechanism at some loading and environmental conditions (44). This conclusion is somewhat questionable as it is very difficult to achieve a pure mode III loading. The fracture path in SCC failures which occur in high strength Al alloys in service is generally intergranular (46). In slow strain rate experiments, transgranular fracture has been reported and appears to be related to conditions under which low levels of absorbed hydrogen were produced (47).

The SCC fracture surfaces are commonly covered with a cracked brittle layer known as the "mud crack pattern." The nature of this layer is unclear.

2.4.1.3 Hydrogen Embrittlement

As mentioned earlier, there is persuasive evidence for hydrogen embrittlement in high strength aluminum alloys. Previous research has focussed upon the role of various microstructural parameters, such as oxide films, grain boundaries and precipitates, in the hydrogen embrittlement

process. Analysis of these results suggests, however, that they relate to the rate controlling steps rather than to the mechanics of hydrogen embrittlement process.

Previous mechanical property tests did not reveal any influence of gaseous hydrogen on the mechanical properties of aluminum (48). Blister formation on the surface of commercially pure aluminum (1100 aluminum alloy) has been interpreted as an indication of hydrogen embrittlement (49). Blister cross sections and the morphology of the internal surfaces were studied and it was concluded that the internal delamination leading to the blister formation was an intergranular fracture accompanied by plastic deformation. Since the blisters were formed at 773°K, aluminum hydride is very unlikely to be involved.

In 1956, 1100 aluminum was reported to disintegrate along grain boundaries above 200°C in a water vapor atmosphere (50). The severity of the attack was reduced by coupling aluminum to more cathodic metals. It has been concluded that the attack was mechanical damage caused by hydrogen penetrating along grain boundaries.

It was found in recent in-situ TEM experiments on pure aluminum and on 7XXX series alloys that hydrogen induced crack propagation by enhanced plasticity at the crack tip (51), suggesting a localized ductile mechanism for hydrogen embrittlement. On the other hand, a thin specimen of high strength aluminum alloy was cracked in a stress corrosion test conducted in moist air and then studied in the transmission electron microscope. No dislocations were found along the crack and totally brittle behavior was suggested (43).

The study of hydrogen precharged thin samples in the transmission electron microscope revealed interaction of dissolved hydrogen with an electron beam resulting in bubble nucleation and growth (52,53).

Aluminum hydride has been reported on the fracture surface of a pre-embrittled high strength aluminum alloy (29). Morphologically it resembled the "mud crack pattern" common to stress corrosion cracks. This finding opens the possibility of a hydride related mechanism of hydrogen embrittlement in aluminum base alloys.

The suggestion of hydrogen induced lattice decohesion is often advocated, however, without direct experimental evidence.

3. EXPERIMENTAL PROCEDURE

3.1 Sample Preparation

Super Raffinal aluminum, 99.999% pure, ingots were used throughout this research. These ingots, purchased in 1961, were supplied with chemical analyses by the manufacturer. The only detectable elements were Si, Fe and Cu with corresponding concentrations of 1, 2.2 and 1 ppm. This material was sufficiently pure to allow recrystallization at room temperature. The ingots were cut into pieces, cold rolled at room temperature to thicknesses of 0.08, 0.25 and 0.5 mm and then used in the cold rolled form or annealed at 550°C.

The thinnest sheets were used for a study of the effects of pure water on an ultrasonic field on fracture. Several tensile specimens, in the form of a double cantilever beam, were prepared from the 0.25 mm thick sheets. A major part of the study was carried out using the 0.5 mm thick sheet. Two types of tensile specimens were cut from this sheet; (1) specimens having a variable gauge section width (type I), and (ii) those with a uniform gauge section (type II). The geometry and dimensions of these specimens are given in Figure 1.

3.2 Slow Strain Rate Tensile Tests with Simultaneous Hydrogen Charging

The tensile specimens used for these experiments were tested while immersed in deionized water contained in a plastic container and subjected to an ultrasonic field. A Branson cleaner, Model 220, has been adapted for the purpose of producing this ultrasonic field. The stainless steel bath has been taken out of the cleaner and the plastic container with the lower grip was

Fig. 1. Geometry and dimensions of tensile specimens.

Fig. 2. A schematic illustration of a test assembly. (1) an ultrasonic bath; (2) a lower grip made out of Macor; (3) an upper grip made out of Macor; (4) a plastic container; (5 and 6) bolt made out of Lexan (7) specimen.

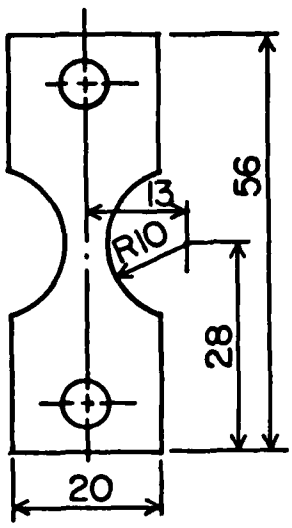

Type I

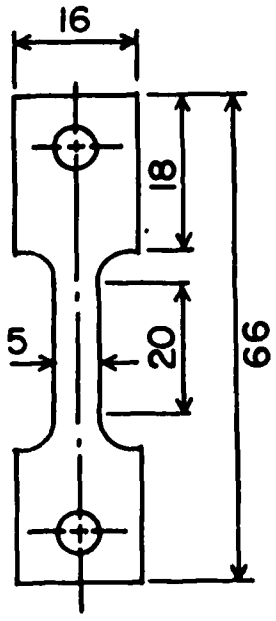

Type II

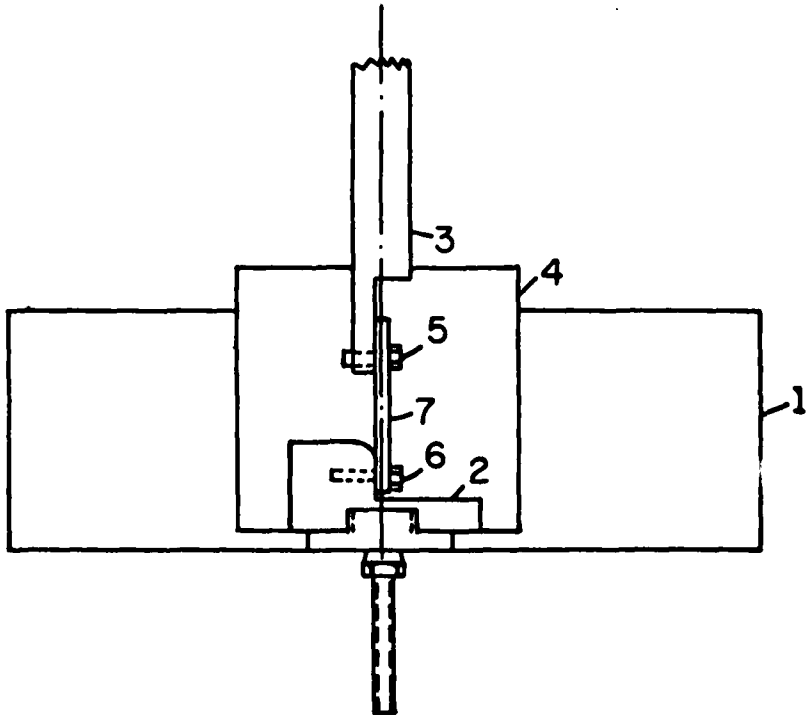

mounted in it as shown schematically in Figure 2. No metallic parts other than the specimen were present in the plastic container during the testing to avoid electrolytic currents. The whole assembly was mounted on a MTS machine. The specimens used in this part of the study were mainly of type I notched from one side in the middle of the gauge length. The notch was made 0.25 mm wide and 0.75 mm deep using a spark erosion machine.

3.3 Slow Tensile Tests With Hydrogen Precharged Specimens

Hydrogen was introduced into tensile specimens by charging in NaOH solutions saturated with Al ions. The pH of the solutions was chosen to be in the chemically active region according to the Pourbaix diagram for Al. In general a solution having pH 12 was used. The solution pH was monitored with PHydration Papers. To reduce pitting during the charging, the solution was stirred with a Porta-Stir magnetic stirrer.

After charging for times sufficient to allow H diffusion throughout the specimen thickness, the tensile specimens were strained in air in the same assembly as that used for the dynamic charging. The specimens were coated with silicone oil before and during the straining to prevent contact with humidity in the atmosphere.

The hydrogen content of the charged samples was determined by the vacuum extraction technique with a liquid nitrogen trap to condense any water vapor which may have been evolved from the specimens. Specimens for the hydrogen analyses usually were melted to reduce the time of the analyses and to increase its precision.

4. RESULTS AND DISCUSSION

4.1 Degradation and Hydrogen Charging of Thin Sheet Specimens in an Ultrasonic Water Bath

In the first part of the work 0.08 mm thick sheet specimens were exposed to pure deionized water in an ultrasonic field without the application of an external stress. While no measure of the ultrasonic field intensity was carried out, it was not particularly intense as it was produced by a 220 W Branson Model with an input power of 125 W. Damage in the form of cracks, surface blisters and cavitation-erosion pits was observed in these unstressed specimens as shown in the typical examples given in Figures 3 and 4. Cracks were formed at the grain boundaries and were accompanied by a significant amount of plastic deformation as judged from the crack opening displacements and from the fracture morphology. While some of the fracture surfaces looked much smoother than that seen in Fig. 4, there almost always was evidence for plastic deformation in the form of surface shear lips and crack openings. Cracking of the sheets was especially severe if the specimens were quenched from elevated temperatures and cathodically charged with hydrogen before being placed in the ultrasonic bath. In this case, a specimen having an area of about 15x15 mm was totally disintegrated in about 10-15 min. Grains were observed to fall out of the sheet during the exposure to the ultrasonic bath. Continuous twisting and bending of a thin strip was observed in the ultrasonic bath indicating a substantial nonuniform plastic deformation was probably caused by the cavitation.

It has been found that a very large amount of hydrogen absorption took place during the exposure to the ultrasonic bath. For example, about 8,000 appm of hydrogen was measured after the exposure to the ultrasonic field in pure H_2O

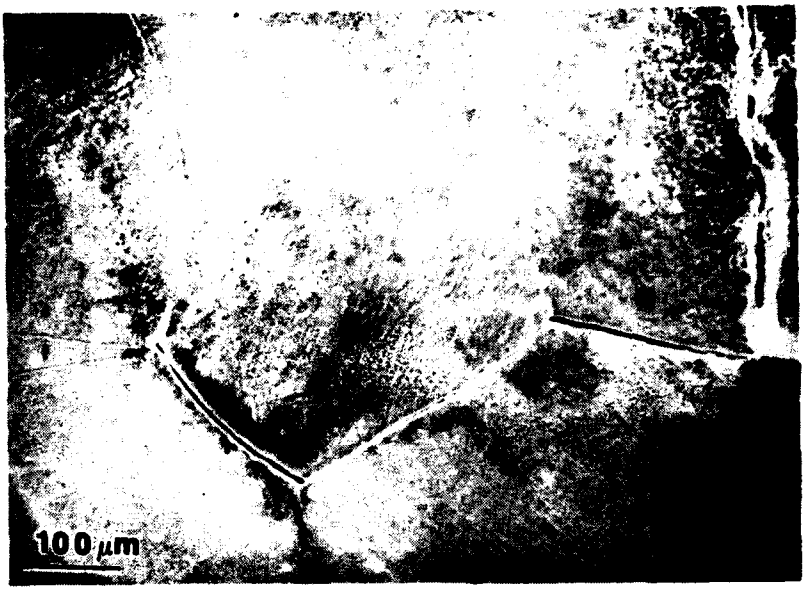

Figure 3. A view of the surface of a 0.08 thick sheet after a treatment in an ultrasonic bath. Notice grain boundary cracks. Some of the cracks are open which indicates a large amount of grain boundary sliding. Before the ultrasonic treatment the sample was quenched from 600°C into ice water and then cathodically charged with hydrogen

Figure 4. The same sample as in Figure 3. A view on the open grain boundary crack at the edge of the sheet. A fracture "A" and a sheet surface "B"are seen.

for about a week. Based on these observations, the ultrasonic bath containing deionized water was used to charge specimens during the mechanical property tests.

4.2 Slow Strain Rate Tests with Simultaneous Hydrogen Charging

4.2.1 Macroscopic Deformation Behavior

A systematic study of such macroscopic deformation parameters as the ultimate tensile stress, total elongation to fracture, amount of uniform elongation up to the onset of necking and elongation during localized necking, has been carried out for type I specimens with the results given in Figures 5 and 6. The hydrogen charging during the tensile tests was carried out using an ultrasonic field and deionized H_2O as previously discussed. As a reference, similar tests were carried out in silicone oil with and without the ultrasonic field. In the silicone oil environment, no effect of the ultrasonic field was observed. It should be kept in mind, however, that ultrasonic oscillations are expected to be stronger in water than in silicone oil due to the difference in their viscosity and therefore a possible effect of the ultrasonic vibration on the mechanical behavior cannot be completely ruled out in our tests. The value of the ultimate tensile stress is decreased by hydrogen charging at all of the deflection rates studied. The decrease in the ultimate tensile stress is most pronounced for tests carried out in H_2O with the ultrasonic field but decreases are also seen in precharged specimens.

Figure 6 represents the dependence of the total elongation to fracture and its components; uniform elongation prior to necking (as indicated by the irreversible load drop*) and elongation during the localized necking

*The reversible load drops indicate a burst of plastic instability during the uniform stages of deformation.

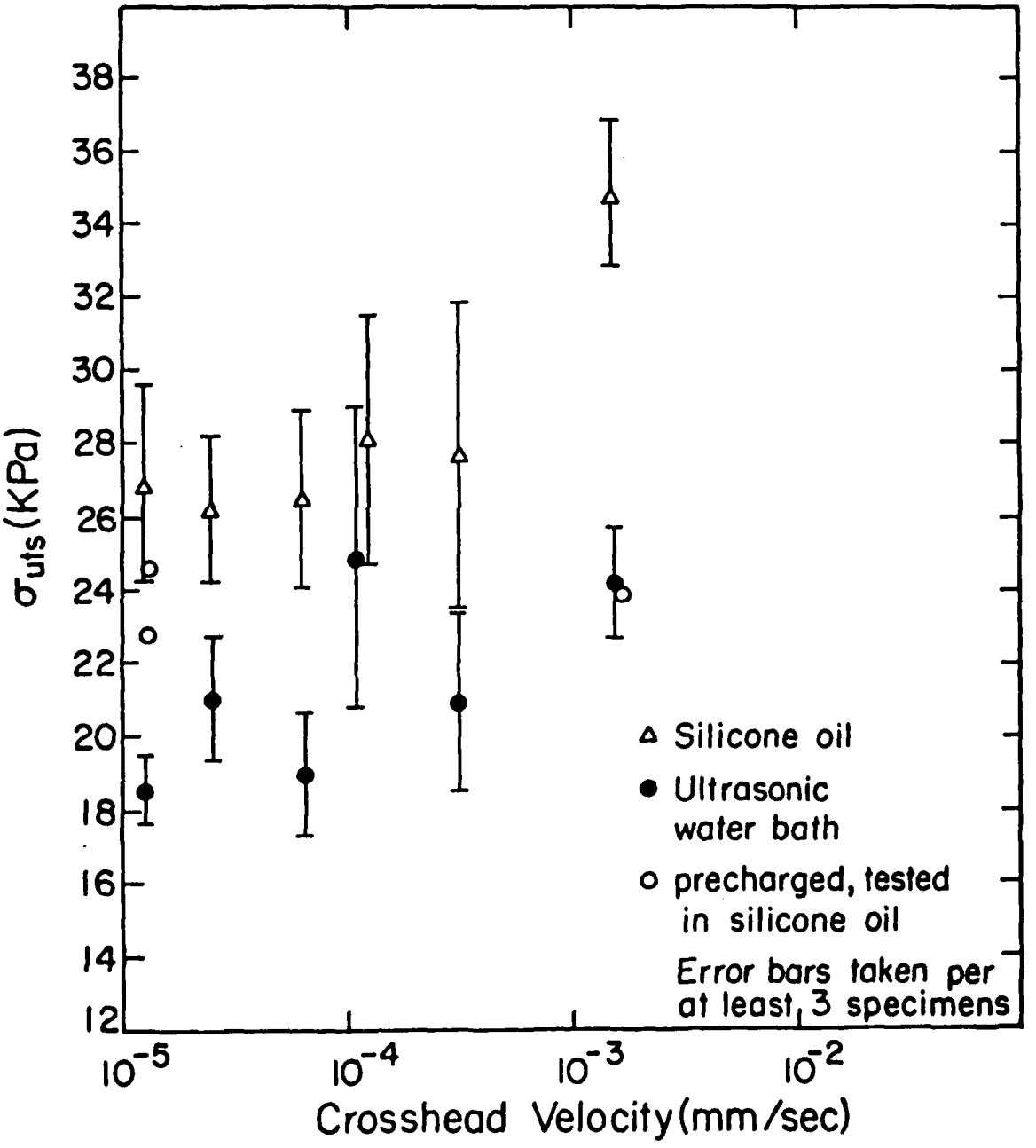

Fig. 5. Ultimate tensile stress of the type I specimens as function of the deflection rate.

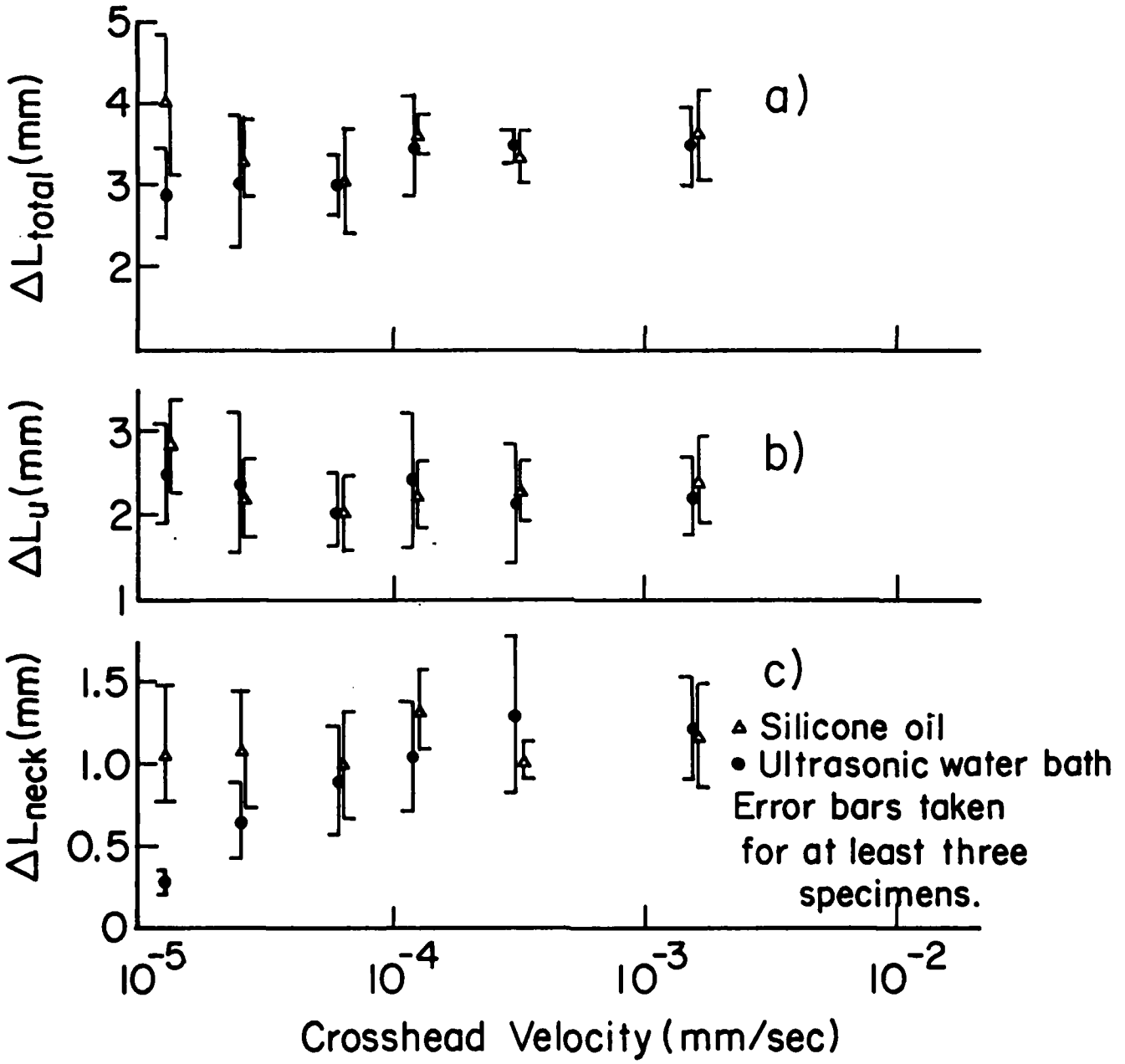

Figure 6. Deflection of the cross head (a) till break (b) during uniform deformation (c) in plastic instability region

ΔL_{total} - total deflection to break
ΔL^{u}_{neck} - deflection during uniform deformation
ΔL^{u}_{neck} - deflection in necking period.

to fracture, on the elongation rate. The only difference between the two groups appears at the local necking stage. At deflection rates below 1.25×10^{-4} mm sec^{-1}, a decrease in the amount of plastic deformation in the necking stage is observed. Such a tendency doesn't appear in the reference group of specimens tested in silicone oil. However, due to the large error in the results, the difference between the two groups is statistically significant only at the slowest crosshead velocity, 1.25×10^{-5} mm sec^{-1}.

Bursts of plastic instability were observed during the uniform elongation of specimens tested in water in an ultrasonic bath. These could be seen on the load deflection curves of the slowest strain rate tests and were manifested either by fast erratic movement of the chart recorder pen or by the slower load drops, with the greatest load drops occurring towards the onset of necking. Much less pronounced bursts of plasticity were observed in the control group tested in silicone oil.

4.2.2 Fracture Behavior

Cracks usually developed from the notch root. At all deflection rates, the cracks began propagating after the onset of macroscropic localized necking. This was confirmed by correlating the onset of visible cracks to the load-deflection chart. Whereas in neutral environments the cracks generally started after a substantial delay after the necking began, the cracks in the ultrasonic water bath tests proceeded immediately or shortly after the load drop development.

Specimens tested in silicone oil with or without application of ultrasonic oscillations, in laboratory air and in water without ultrasonic application fractured in a completely ductile manner with a chisel point type

of fracture (100% reduction in area). In some specimens tested at the lowest deflection rate, small areas which differed from the chisel point fracture have been detected during the SEM observation. The reduction in area was still close to 100%.

Specimens tested in the ultrasonic water bath showed a completely different behavior. Only at the highest extension rate used, 1.6×10^{-3} mm sec^{-1} was the fracture sometimes of the chisel point type. At all the slower deflection rates tests fracture occurred before complete necking. The lower the extension rate, the smaller was the extent of necking that preceded the fracture (Figure 7). As also can be seen from Figure 7, the crack initiated when total or almost total necking developed at the notch root. One specimen with two very sharp notches cut from the two opposite sides was tested at a deflection rate of 1.25×10^{-5} mm sec^{-1} to determine whether severe necking occurs prior to crack initiation even for a sharp crack-like notch. Even in this case almost total necking at the root notch preceded the crack nucleation. The amount of plastic deformation which developed before the initiation of the fracture was evaluated quantitatively by measuring the reduction in thickness of specimens 1 mm from the notch root (Figure 8).

The crack path was primarily transgranular. However, for the three slowest extension rates, 6.2, 2.55 and 1.25×10^{-5} mm sec^{-1}, the crack propagated initially in a transgranular fashion and then changed to a predominantly intergranular mode towards the end of the fracture process (Figure 9). The appearance of the transgranular fracture surfaces varied, particularly when observed at high magnifications of about 1,000 X and higher. Some typical fractographs are shown in Figures 10-12.

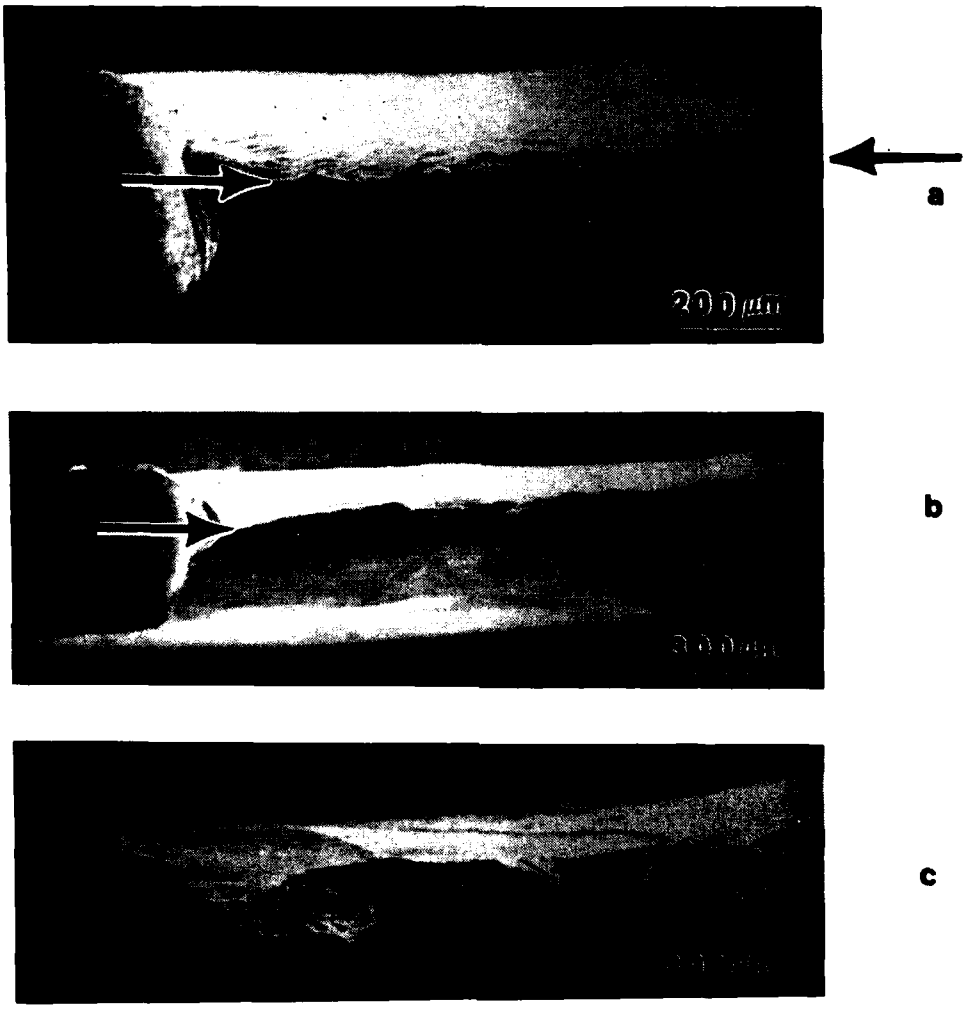

Figure 7. Fracture appearance of specimens tested at different cross head rates. A notch surface is seen on the left part of the pictures. Crack propagation is from left to right. a) Cross head rate 1.6×10^{-3} mm/sec; b) cross head rate 3.2×10^{-4} mm/sec; c) cross head rate 6.35×10^{-5} mm/sec. Fracture in (a) and (b) is indicated by the arrows.

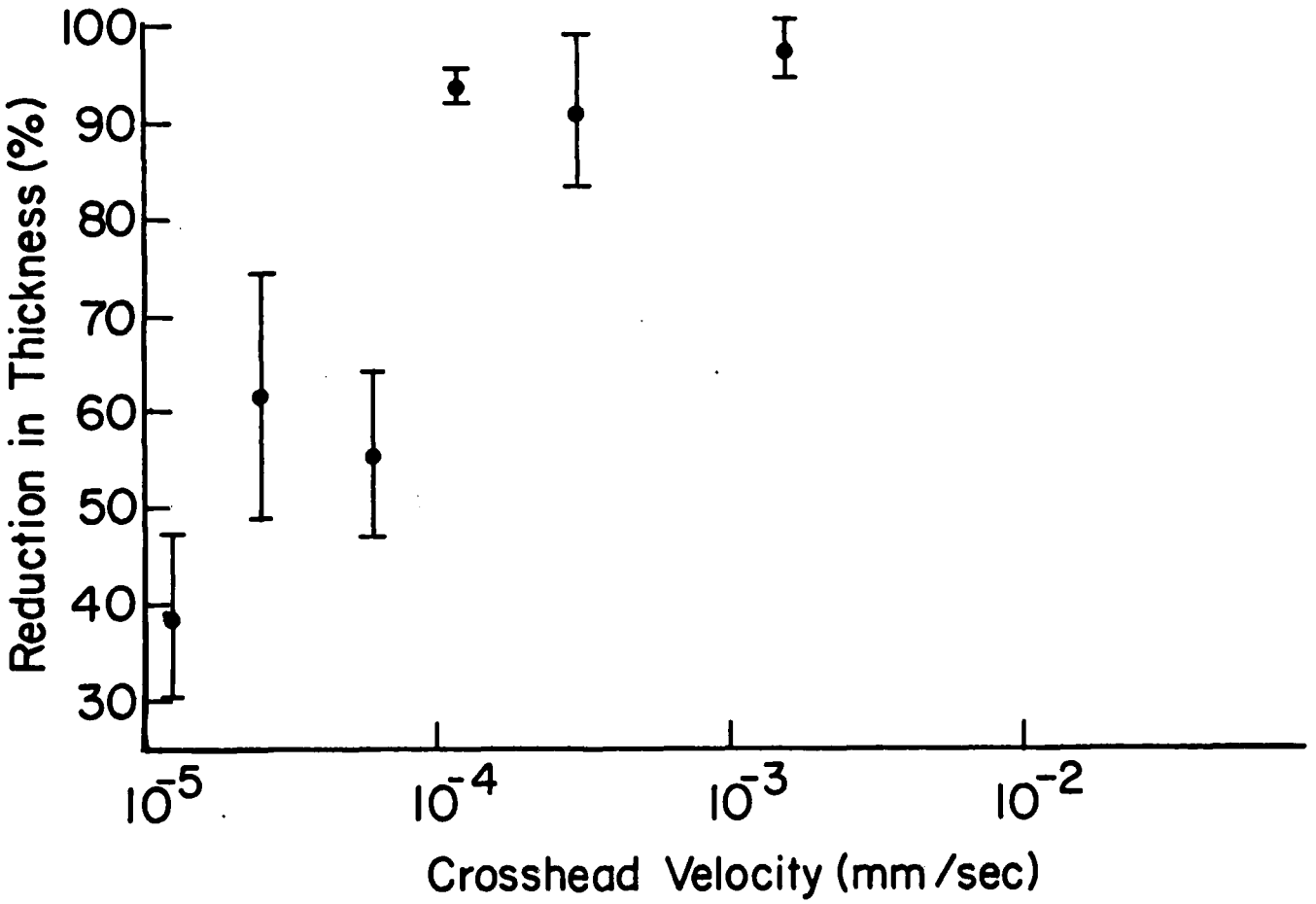

Figure 8. Reduction in thickness of the fracture surface. The error bars correspond to at least three specimens.

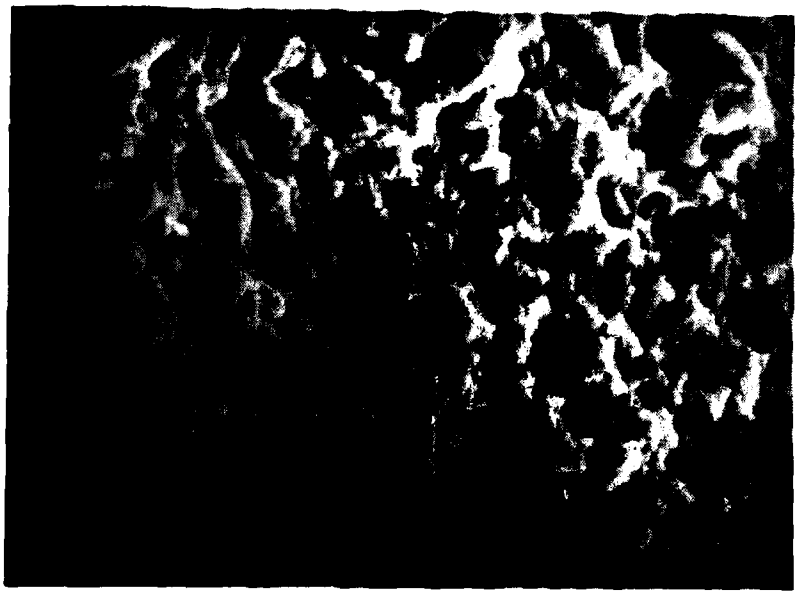

Figure 12. Specimen tested at an extension rate of 3.1×10^{-4} mm sec^{-1}. Small pyramid like areas comprise the fracture surface. This appearance resembles ductile zig-zag type of fracture as seen in HVEM environmental tests (51). Small secondary cracks directed at about 11 o'clock form striations.

Figure 13. Transgranular fracture in two neighboring grains, "A" and "B". Pictures a) and b) have been taken from the matching spots on the opposite fracture surfaces. The extension rate was 3.1×10^{-4} mm sec^{-1}. The fractographs were printed with reverse contrast to show the interlocking nature of the fracture surfaces.

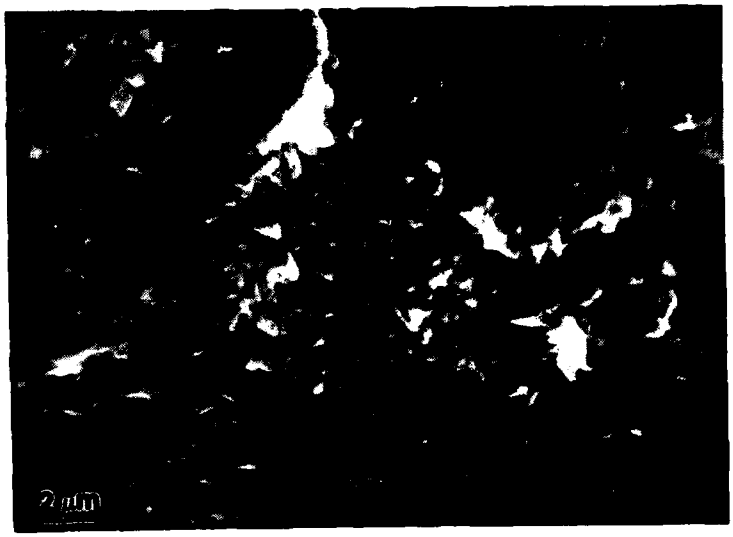

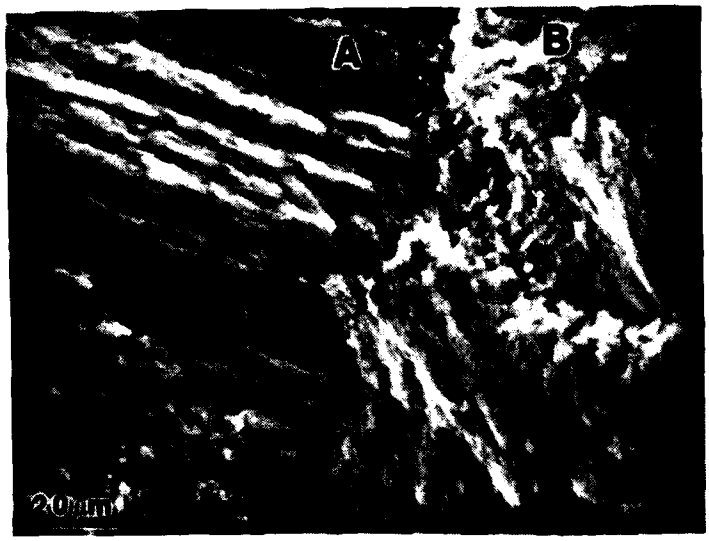

a

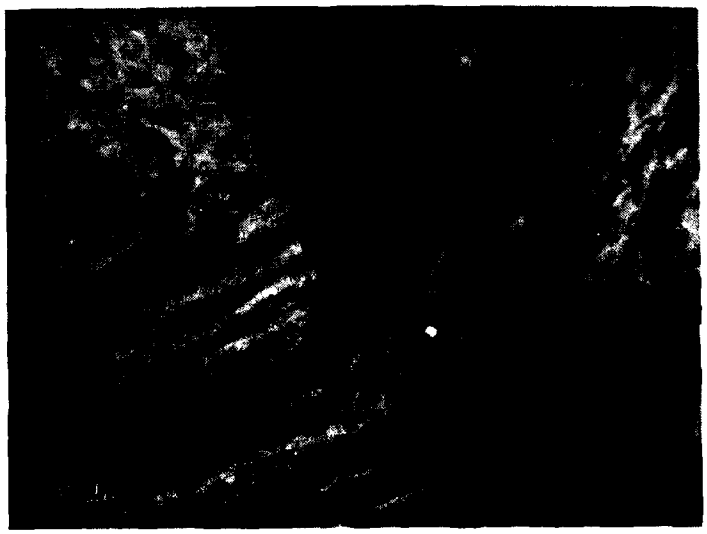

b

The transgranular fracture appearance generally seemed to depend more on the grain orientation than on the strain rate. An example of the fracture morphology difference in two adjacent grains is given in Figure 13. Fractographs 10 and 11 differ significantly and relate to two grains in the same specimen. It also can be seen from Figure 13 that the correspondence of the features on the opposite fracture surfaces is roughly of the "lock-in" type (peak to valley match). This was the general observation when the matching was carried out at magnifications of about 1,000 and below. The comparison of the fine details on the opposite fracture surfaces was difficult and no certain conclusions about the type of matching have been drawn in that case. The main distinct feature of the transgranular fracture commonly seen at the three lowest extension rates 6.2, 2.55, 1.25×10^{-5} mm sec^{-1} and not found at the three fastest 1.6×10^{-3}, 3.1×10^{-4} and 1.25×10^{-4} mm sec^{-1}, is the so-called "feather-like" pattern shown in Figure 14. The patches and steps between them which created the pattern on the fracture surface could be correlated with slip bands on the specimen side surfaces. Observed at higher magnifications, the patches were not flat and usually exhibited the same kind of fracture features which could be found outside the "feather-like" areas. Sometimes, numerous subpatches were seen on the main ones of the "feather-like" pattern as shown in Figure 15. This occurred when the main patches were inclined to the fracture surface. Once again, the inclination depended on the grain orientation. In many cases striations have been observed in the transgranular portion of specimens tested even at high strain rates as can be seen in Figure 16. The striations were perpendicular to the crack propagation direction. Additional examples of the striated fracture are shown in Figures 17 and 18.

Figure 14. A feather-like pattern on the transgranular part of the specimen tested at an extension rate of 1.25×10^{-5} mm/sec.

Figure 15. Example of the feather-like pattern observed at higher magnification.

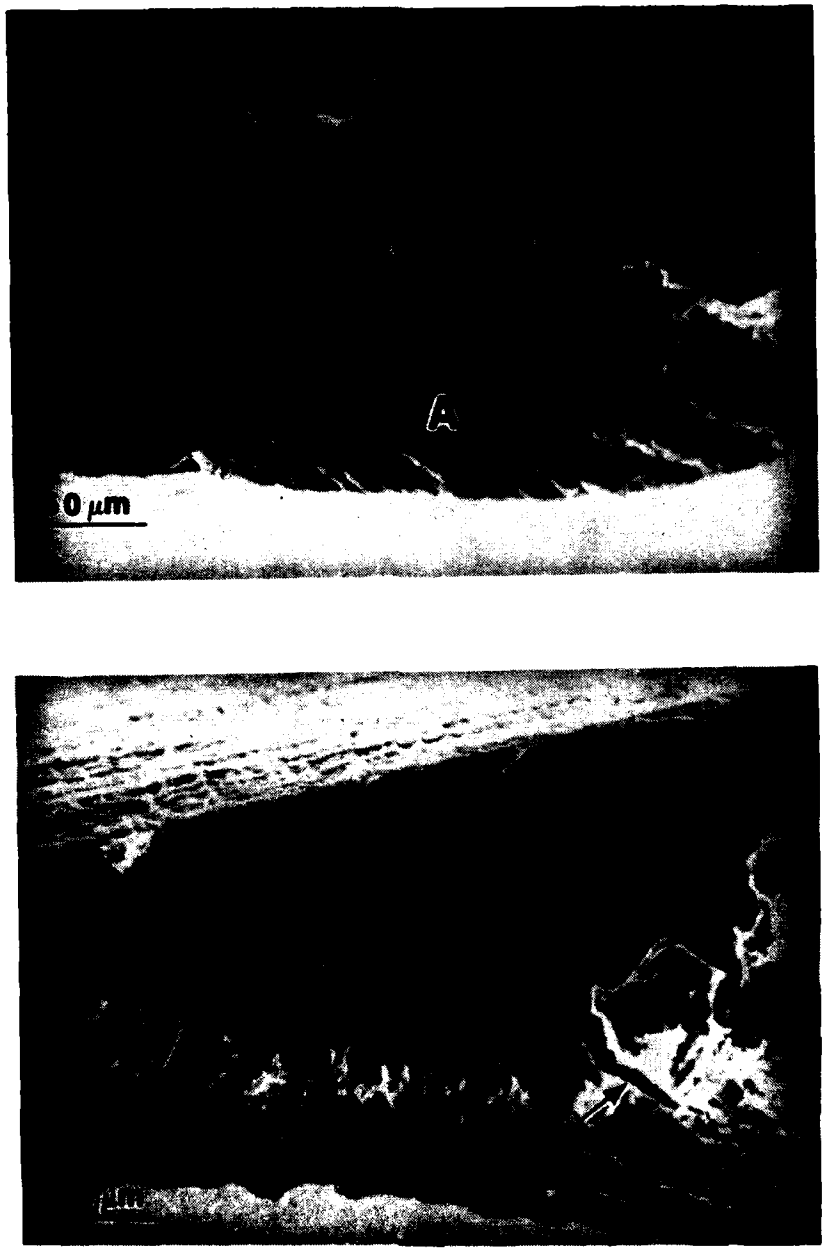

Figure 16. Transgranular fracture in the specimen tested at deflection rates of 3.1×10^{-4} mm sec^{-1}. Fractographs a) and b) were taken from the matching areas on the opposite fracture surfaces. Crack propagated from the left to the right. Notice striations on both fracture surfaces. A secondary crack is observed in Figure 16b shown with arrow. Area "A" in Figure 16a seems to be damaged mechanically.

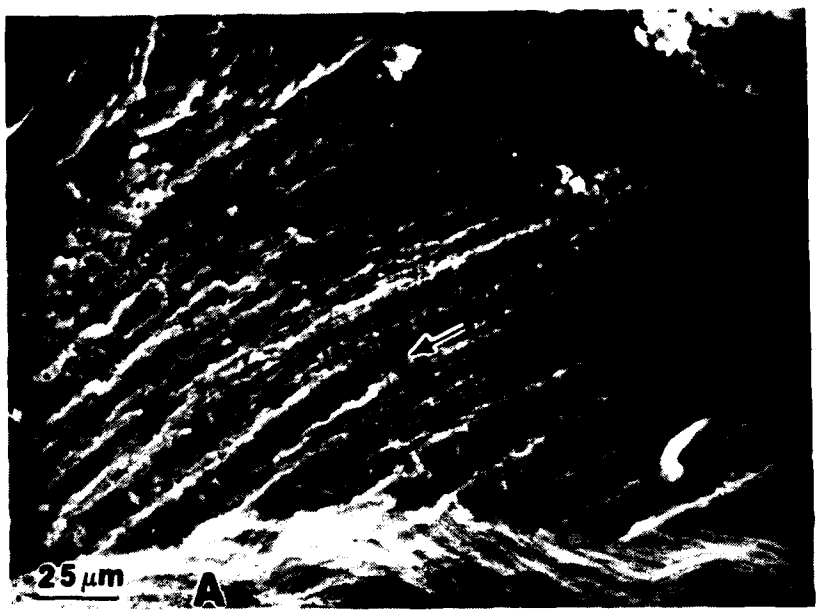

Figure 17. Example of the striated fracture region of the specimen tested in H_2O with an ultrasonic field at a 1.25×10^{-5} mm sec^{-1} extension rate. The assumed local direction of crack propagation is marked with an arrow. Area "A" is the side specimen surface.

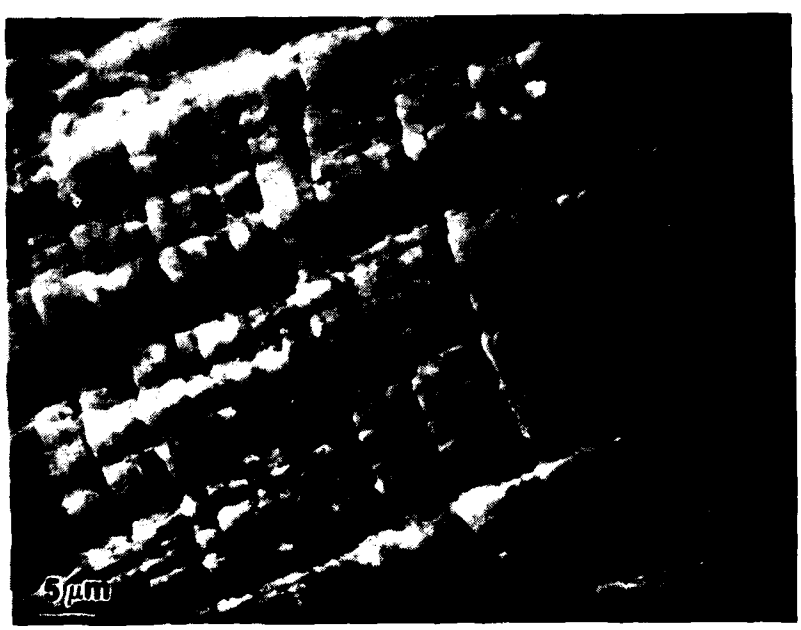

Figure 18. Striations as seen in Figure 17 shown at higher magnifications.

Another characteristic feature often observed on the fracture surfaces is areas appearing to be covered with a film, as shown in the lower part of Figure 16a. Surfaces having such an appearance appeared to be damaged mechanically. In samples tested at the slowest strain rates, a few of the areas which exhibited film-like features were observed to be fragmented by cracks (Figure 19). This so-called "mud crack" pattern has been usually reported in the literature as occurring on intergranular fracture surfaces while the present obervations are on transgranular fracture surfaces. No new features were found at higher magnification on the intergranular fracture compared to those seen in Figure 19.

Grain boundary facets were not flat and smooth but always exhibited some surface relief. Several tests were run with specimens fabricated from 0.25 mm thick sheet. This has been done to compare its fracture surfaces to those obtained in 0.5 mm thick sheets. The cracks were of the mixed transgranular-intergranular mode. Many areas with apparent films were observed. The general impression was that the film was formed on mechanically damaged areas as could be seen, for example, in Figure 20. The surface in the middle portion of the fracture exhibited a crack network. The matching area on the opposite fracture surface was checked and a similar looking area in the middle portion of the fracture was found. The areas with the apparent films were found most often and with the greatest clarity on the grain boundaries although the film was occasionally observed on the transgranular portion of the fracture (Figure 19). The grain facets were either relatively smooth or exhibited a relief consisting of cavities and elevations with an interlocking type of matching between opposite faces (Figure 22). The surfaces of the larger of those features clearly were the ductile fracture

Figure 19. Example of the mud crack pattern on the transgranular fracture of the specimen tested at a 1.25×10^{-5} *mm* sec^{-1} extension rate.

Figure 20. Example of the fracture surface presumably damaged mechanically. Notice crack network on the damage surface "A". The fracture path was in the vicinity of the grain boundary.

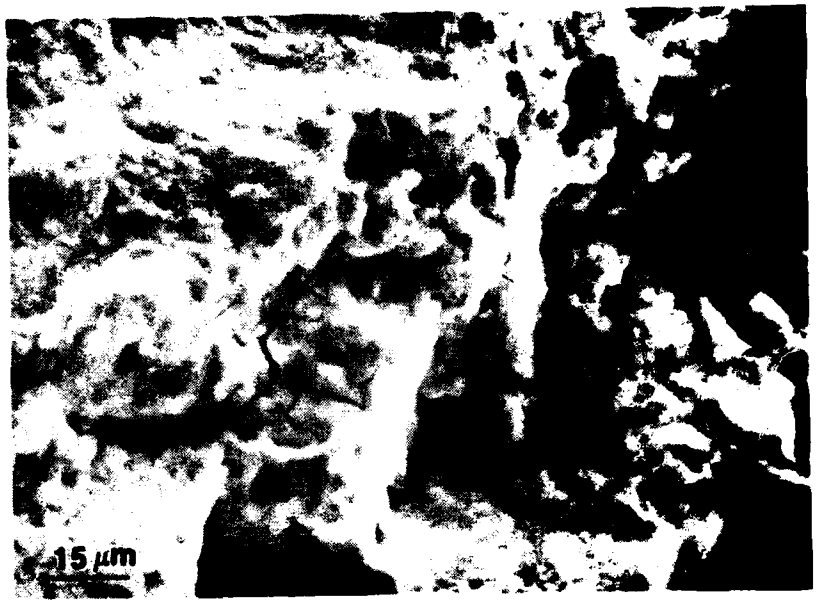
15 μm


A

Figure 21. Two matching fracture surfaces. View of the mixed transgranular-intergranular fracture. Grain facets appear as dark areas.

Figure 22. Grain boundary facet on the fracture of the 0.25 mm thick cantilever beam type specimen. (a) and (b) are two oppostite matching surfaces. Figure 22b is printed with a reverse contrast.


00 µm


3 µm

areas. They had a bright unfilmed appearance. Another example can be seen in Figure 23. In this case the system of the grooves and ridges presumably indicates the shift between the two opposite fracture surface with the corresponding mechanical damage. In spite of the specimens being tested in mode I, we assume that the crack actually propagated by alternative shear at the crack tip, which could cause sliding between two fracture surfaces. The system of the unfilmed elevations should, however, form after the sliding ceased, otherwise it would be smeared out. This apparent contradiction is eliminated if we assume that adhesion of the opposite sliding surfaces caused spots of cold welding. These cold welded junctions broke apart on the subsequent crack opening given the above system of cavities and elevations. Additional discussion of this point will be given later in section 5.5. An additional example of the filmed surface fragmented by network of cracks (mud crack pattern) is given in Figure 24. As can be seen, the crack network pattern is different for the matching surfaces and therefore formed after the film formation. The last observation was confirmed by comparing several more matching areas which exhibited fragmented films.

4.3 Slow Strain rate Tests of the Precharged Specimens in Silicone Oil

Hydrogen charging of type II specimens studied in these experiments was performed by exposure of the tensile specimens to sodium hydroxide solution with pH 12 in the absence of ultrasonic oscillations. This treatment resulted in hydrogen concentrations in the range of 1,000-1,500 appm as determined by vacuum extraction. Specimens were charged in large groups, typically of eight specimens, to ensure they experienced identical charging conditions. The charging typically lasted 12-14 hours. During this period

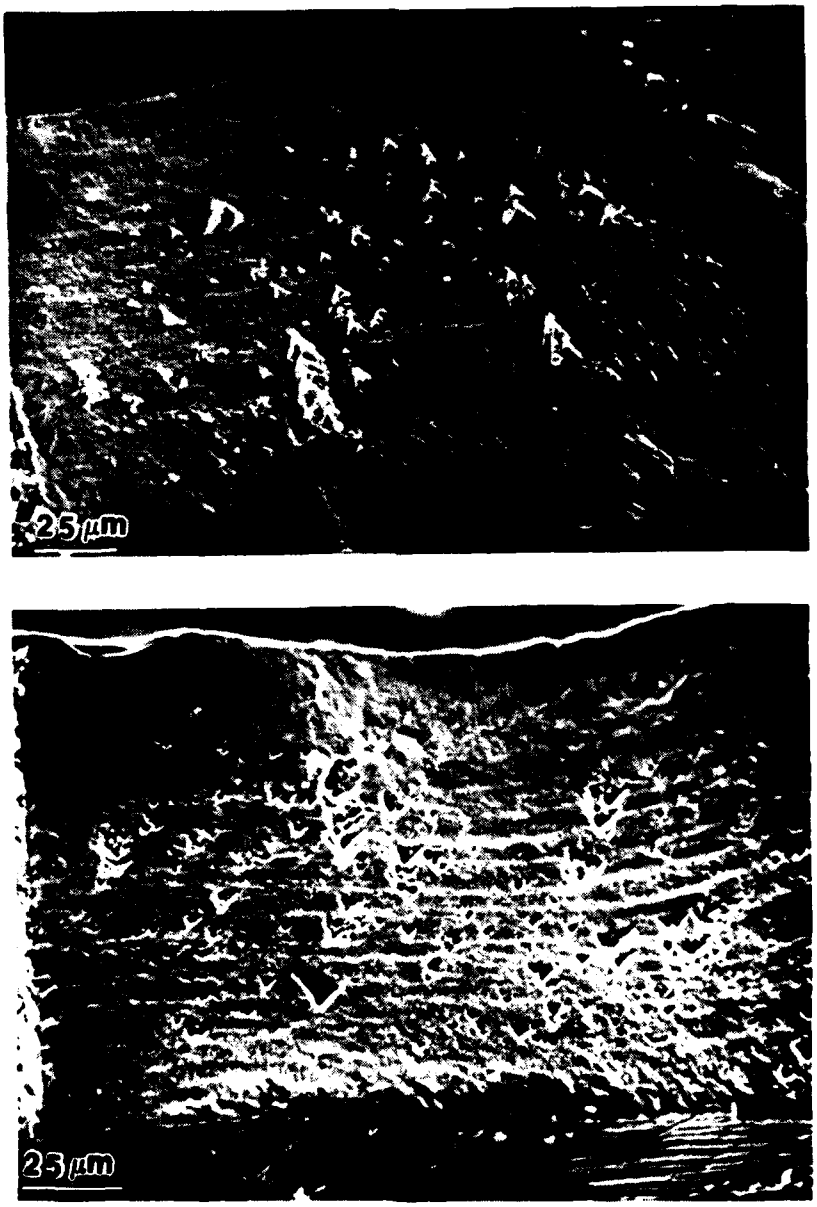

Figure 23. Grain facet on the fracture surfaces of the 0.25 mm thick cantilever beam specimen. (a) and (b) are two matching opposite surfaces. Notice the horizontal and ridges on both surfaces.

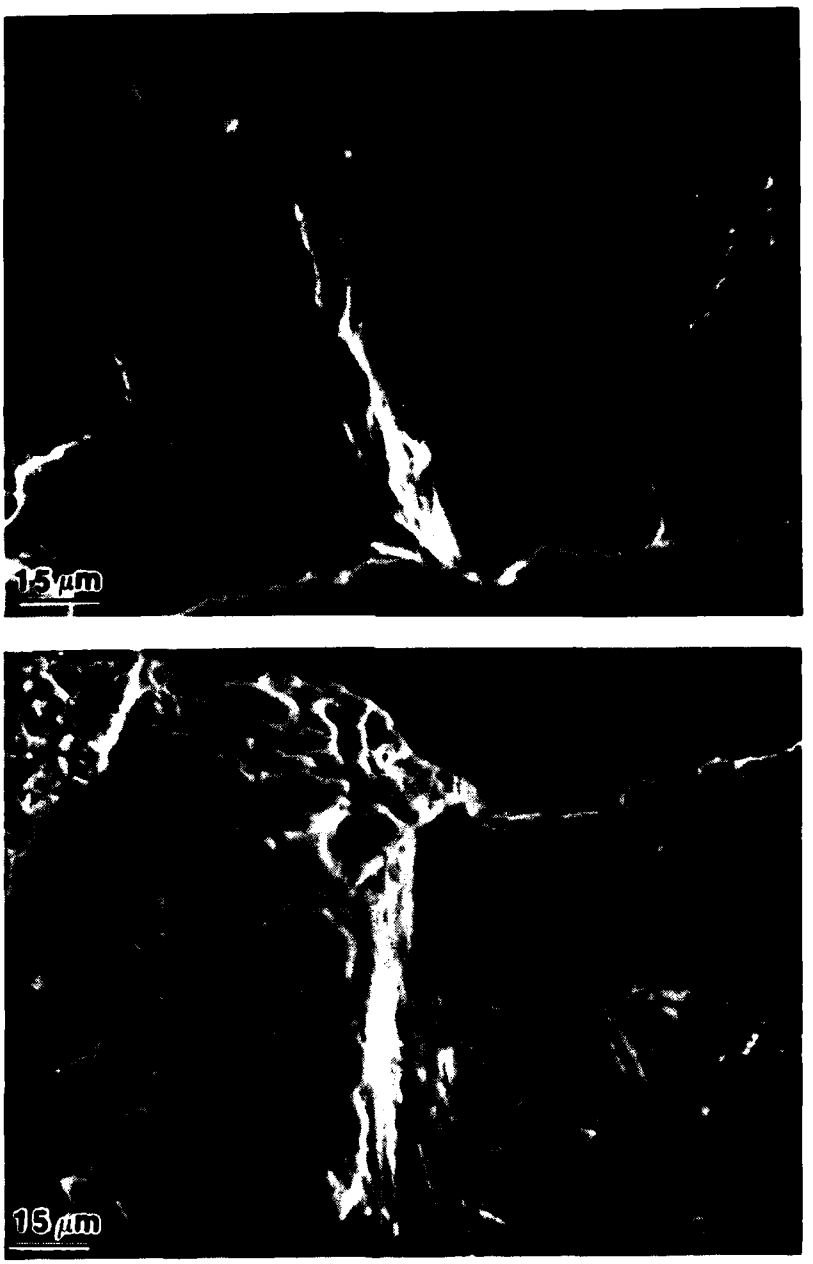

Figure 24. View of the matching fracture surfaces of an opened secondary crack. The specimen was of the double cantilever beam type made out of 0.25 mm thick sheet. Notice that the mud crack pattern is different on the opposite fracture surfaces.

the specimens were thinned from 0.5 mm to about 0.35 mm due to the corrosion reaction. The removal of the aluminum occurred relatively uniformly over the gauge length. Whereas details of the corrosion rection are unknown, it probably incorporates two basic processes; dissolving of the aluminum hydroxide and surface repassivation. Hydrogen bubbles forming on the surface were observed during the charging.

Efforts were undertaken to facilitate uniform surface dissolution to prevent pitting. Two measures were found to be effective, first, saturation of the solution with aluminum ions prior to the charging (pieces of aluminum scrap were immersed into the solution) and second, stirring the solution during the charging.

4.3.1 Macroscopic deformation behavior

4.3.1.1 Large grain size specimens

This group included specimens preannealed in vacuum at 600°C which resulted in a large grain size of about 1.5 mm, grains having diameters three times larger than the original specimen thickness.

In the first group, four type I specimens were precharged and tested at the 1.25×10^{-5} mm/sec deflection rate in the silicone oil bath. Two were tested in the as charged conditions and two were tested after annealing in vacuum for 48 hours at 350°C after the hydrogen charging. The results are given in Table 1. As can be seen, hydrogen charging caused a decrease in the ultimate tensile stress but had no effect on specimen deflection compared to the uncharged specimens. One possible complication in interpreting the decrease in UTS may arise from surface pitting which accompanied hydrogen charging. The group was charged before the optimal conditions of charging

Table 1

Results of the tensile tests of the precharged type I tensile specimens tested at 1.25×10^{-5} mm/sec deflection rate

Specimen condition	Deflection at the necking onset (mm)	Deflection during the necking development (mm)	Ultimate tensile strength (KPa)
uncharged	2.84±.56	1.13±.35	26.90±2.71
As charged	2.87±.35	1.17±.71	23.8±1.34
Charged and annealed at 350°C, 48 hrs	1.71 ± .52	1.21±.21	20.25±2.47

were found. In contrast to the above, annealing at 350°C had a very large effect both on decreasing the UTS and the uniform deflection. Behavior such as the above could be rationalized in terms of hydrogen bubble formation during the 350°C anneal.

On the basis of the above results, a series of type II specimens was similarly tested. The conditions of these specimens were a) uncharged, with a grain size at 1.5 mm; b) charged, by exposure to aqueous NaOH solution at pH 12; c) charged with hydrogen and annealed at 100°C, d) charged and annealed in vacuum at 200°C and e) charged and annealed in vacuum at 300°C. The annealing time at each of the temperatures was 48 hours. The tensile tests were performed at a 6.4×10^{-7} sec^{-1} initial strain rate and the specimen surfaces were coated with silicone oil during the tests. The stress-strain curves could be grouped into two scatter bands as shown in Figure 25. The deformation

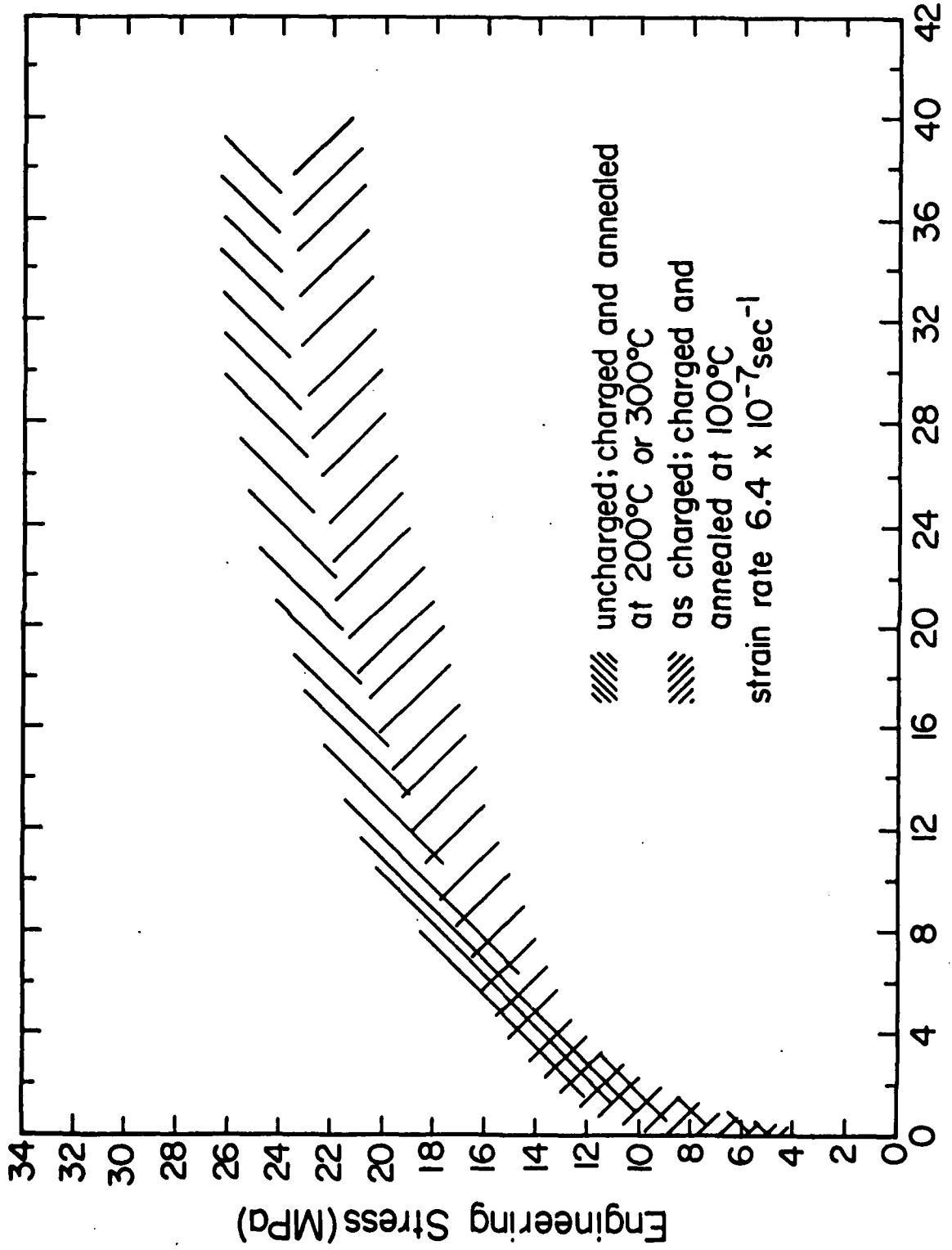

Fig. 25. Results of the slow strain rate tensile tests of the 600°C preannealed specimens.

curves for uncharged specimens and those charged with hydrogen and then annealed at 200°C and 300°C lie in the upper band while the data for specimens in the as charged and charged and annealed at 100°C states lie in the lower band of data. The scatter bands coincide at low strains and diverge at strains greater than 2%. Such behavior is consistent with a reduction of the strain hardening due to hydrogen in as charged and charged and annealed at 100°C specimens. While the observation that the curves for 200 and 300°C postannealed specimens fall within the scatter band of the uncharged specimens could be related to loss of hydrogen during the anneals, hydrogen analysis has shown that only about one third of hydrogen has been lost during the vacuum annealing at 300°C. Another possibility to rationalize apparent recovery of the flow stress of the 200 and 300°C postannealed specimens relates to the reduction of hydrogen in the solid solution by collection of hydrogen in gas bubbles, for example. We can postulate that annealing at 200 and 300°C causes formation of stable hydrogen-vacancy complexes. Some preliminary results from SAXS (small angle X-ray scattering) performed at Oak Ridge National Laboratory are indeed consistent with the assumption of hydrogen vacancy complexes in either as charged or charged and annealed material. Further study of the centers giving rise to SAXS is in progress and these results presumably will help to understand the relationship between postannealing and the flow stress of hydrogen charged specimens.

Fracture areas of the specimens were measured using an optical travelling microscope and the reduction in the cross sectional area at fracture was calculated. The measured values of the reduction of area and of the uniform elongation are given in Table 2 for specimens tested as described above.

Table 2

Results of the strain rate tensile tests of the specimens preannealed at 600°C

Specimen Condition	Reduction of area at fracture (%)	Uniform Elongation (%)
Uncharged	88±11	40.9±2.0
As charged	64±11	37.8±1.9
Charged and annealed at 100°C	82±5	40.3±5.1
Charged and annealed at 200°C	first specimen 57.3, second close to 100	38.4±0.9
Charged and annealed at 300°C	89±1	30.4±7.2

As seen from the data of Table 2, the uniform elongation did not exhibit significant sensitivity to the hydrogen charging or subsequent annealing at 100°C or 200°C. This is in contrast to the macroscopic ductility as measured by the reduction of area. As charged specimens fractured in a more macroscopically brittle manner than uncharged specimens. Annealing at 100°C, 200°C or 300°C after charging resulted in an increase of the reduction of area at fracture to the level observed in the uncharged specimens. These results are consistent with those for dynamically charged specimens and with precharged type I specimens. The decrease of the flow stress and macroscopic ductility (R.A.) caused by hydrogen charging appears to be recovered by low temperature anneals despite the observations reported above that these anneals did not result in any significant loss of hydrogen.

To ascertain that the softening effect caused by hydrogen is recoverable not only by annealing but also by fast straining, two pairs of specimens, charged versus uncharged, preannealed at 600°C were tested at about 10^{-2} sec^{-1} strain rate. The ultimate tensile strengths were measured and no difference was found between the two pairs: (40.1 ± 4.6) MPa and (40.6 ± 1.7) MPa for uncharged and charged specimens respectively.

4.3.1.2 Specimens with initially small grain size

This group included specimens prepared from the 600°C vacuum annealed sheets that were initially about 2-3 mm thick and were reduced by rolling at room temperature to thickness of 0.5 mm and were then stored in silicone oil. This treatment resulted in a recrystallized structure with a grain size of about 0.2 mm. Three specimens were charged in the NaOH solution in the same manner as the large grain size samples. The thickness was reduced to about 0.3 mm during the charging by etching. The specimens were then tested at a strain rate of 6.4×10^{-7} sec^{-1}. Very large differences in behavior were observed between uncharged and charged specimens. The ultimate tensile strength of the as-charged group was less than one half of that uncharged and the total elongation to fracture was in the range of (5.5-26.5%) and (4-5.5%) for the as-charged and uncharged group respectively. It has been observed that these large differences in tensile properties were caused by grain growth which occurred during the hydrogen charging. The grain size after hydrogen charging was non uniform with some grains as large as 1 mm compared to the 0.2 mm grain size of the uncharged specimens. For the specimens preannealed at 600°C no grain growth took place during subsequent hydrogen charging. This phenomena of the grain growth will be discussed separately in section 4.4.

To exclude the factor of the grain size differences, additional groups of specimens have been prepared as follows; a 0.7 mm thick cold rolled sheet was charged by dissolution in a NaOH solution with pH of 12 with a 0.1 mm loss in thickness and then cold rolled by 50% reduction of area to 0.3 mm thick sheet. The average grain size at that point was determined to be about 0.2 mm, equal to that for the uncharged cold rolled sheet. Results of the slow strain rate tensile tests for the three groups are given in Figure 26. It can be seen that the pronounced softening effect observed in the as charged specimens was still observed even though the grain size was kept constant by additional recrystallization at room temperature. The typical macroscopic appearance of the tested specimens is given in Figure 27. The uncharged specimen developed one intense slip band and necking occurred along that slip band. On the other hand charged and cold rolled specimens showed multiple, intensely concentrated slip bands as shown in Figure 27. While these appeared to form perpendicular to the tensile axis, at higher magnifications they were actually comprised of segments of slip bands inclined to the tensile axis. In both these specimens necking developed in a narrow region at these intense slip bands and no reduction in width could be observed. In contrast, as charged specimens exhibited more general necking with appreciable reductions in width. These results clearly demonstrate that hydrogen charging modified plastic deformation and the effect was large enough to be observed on the macroscopic scale. The total elongations to fracture were (4.9±0.6)%, (5.0±1.7%) and (14.1±10.9)% for uncharged, charged and cold rolled, and as charged groups respectively. To check whether the softening effect can be recovered during fast straining, pairs of specimens, uncharged versus charged and cold rolled, were tested at about 10^{-2} sec^{-1} and their ultimate tensile strength

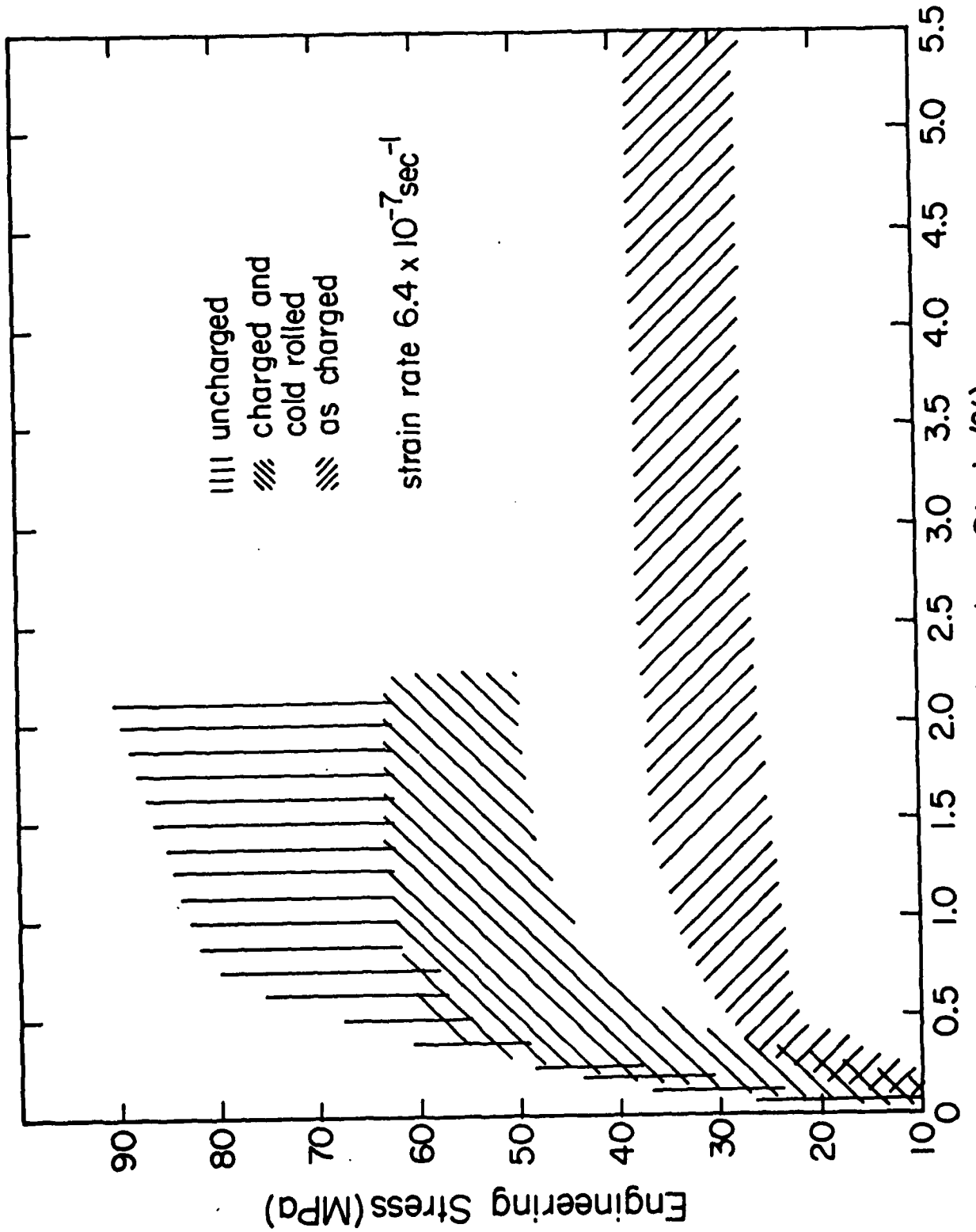

Fig. 26. Results of the slow strain rate tensile tests of the specimens recrystallized at room temperature.

Figure 27. Specimens tested at a slow strain rate of 2.64×10^{-7} sec^{-1}. All of the specimens had a small initial grain size of 0.2 mm. (A) uncharged, (B) charged and cold-rolled, (C) as charged specimen. The grain sizes prior to the tensile tests were in (A) and (B) about 0.2 mm and in (C) non uniform with largest grains up to 1 mm. The large extent of necking in the as charged specimen included a significant decrease in the specimen width. In the hydrogen charged and cold rolled specimens intense slip bands which appeared tranverse to the tensile axis were actually comprised of intense slip band sections inclined to the tensile axis.

measured. The following values were obtained: 97.9±18.2 MPa and 77.1± 14.7 MPa for uncharged and charged and cold rolled specimens. Thus, the softening effect persisted even at very high strain rates. For more complete characterization of the tensile properties at relatively fast strain rates, stress strain curves were measured at a strain rate of 6.4×10^{-4} sec^{-1} for each of the groups of specimens described above with the results shown in Figure 28. The total elongation to fracture was (9.3±1.4)%, (7.6±2.4)% and (10.1±3.0)% for uncharged, charged and cold rolled and as charged specimen groups respectively. As can be seen by comparison of Figures 26 and 28, the increase in strain rate was accompanied by an increase in the flow stresses for all three groups; but the relative positions of their flow stresses remained unaltered. As was the case for the specimens which were preannealed at 600°C, it appears that hydrogen charging reduced the strain hardening of the aluminum. This is shown by the observation that the difference in the flow stresses between uncharged and charged and cold rolled specimen groups occurs only at strain beyond the yield point, Figures 26 and 28.

4.3.2 Characterization of the plastic deformation as revealed by the surface relief

4.3.2.1 Large grain size specimens

Traces of the slip lines on the side surface of the tensile specimens were observed in the SEM. Both necked and uniformly strained sections of the specimens were analyzed. While there were some differences in the slip line appearance on each specimen surface, the micrographs shown in Figures 29-32 represent characteristic patterns. While many surface defects resulting from the cold rolling could be seen on the surface of the uncharged specimen, the specimens were not electropolished as it was observed that electropolishing

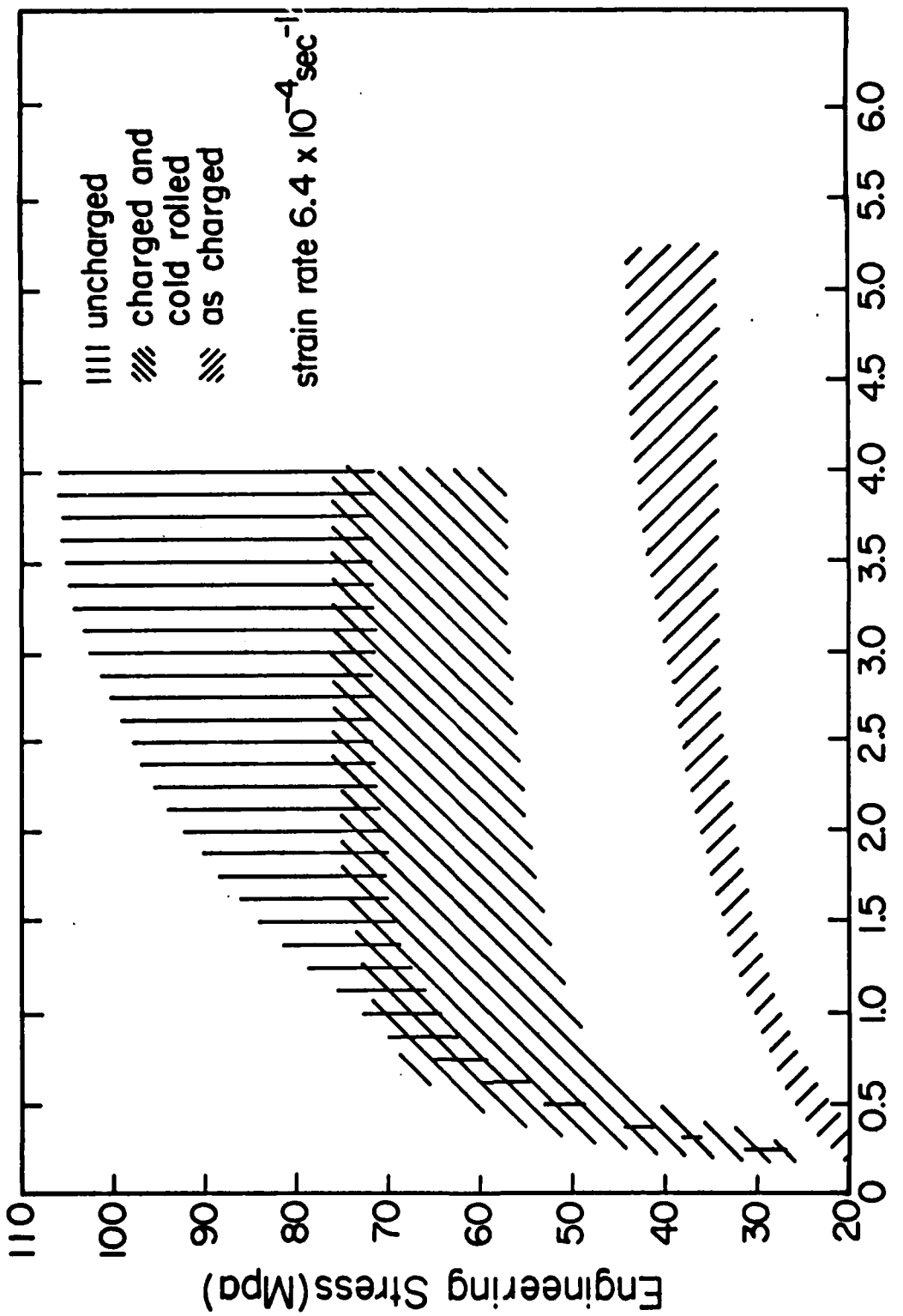

Fig. 28. Results of the fast strain rate tests of the specimens recrystallized at room temperature.

Figure 29. A side surface of the uncharged specimen close to the fracture surface.

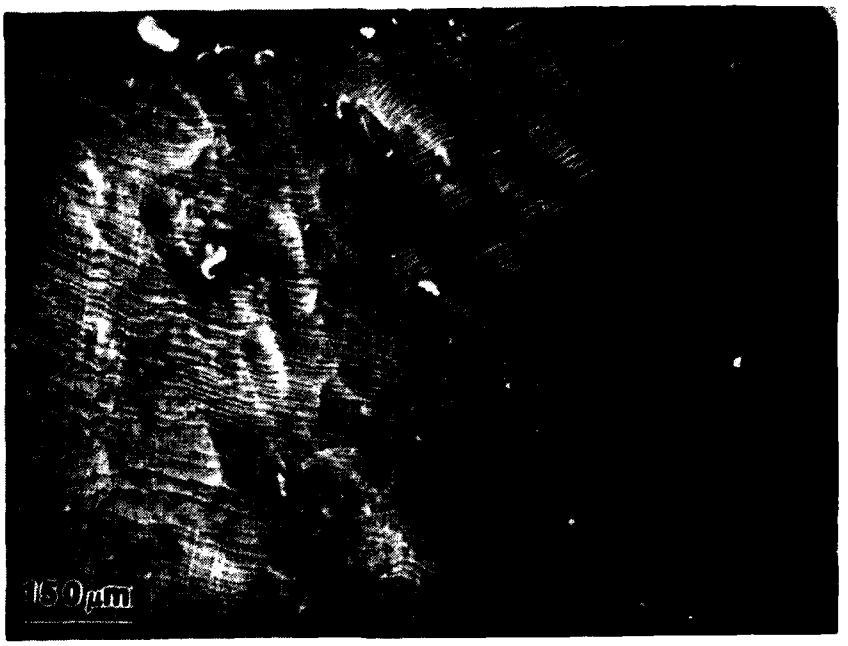

Figure 30. A side surface of the as charged specimen close to the fracture surface. Note the long intense slip lines.

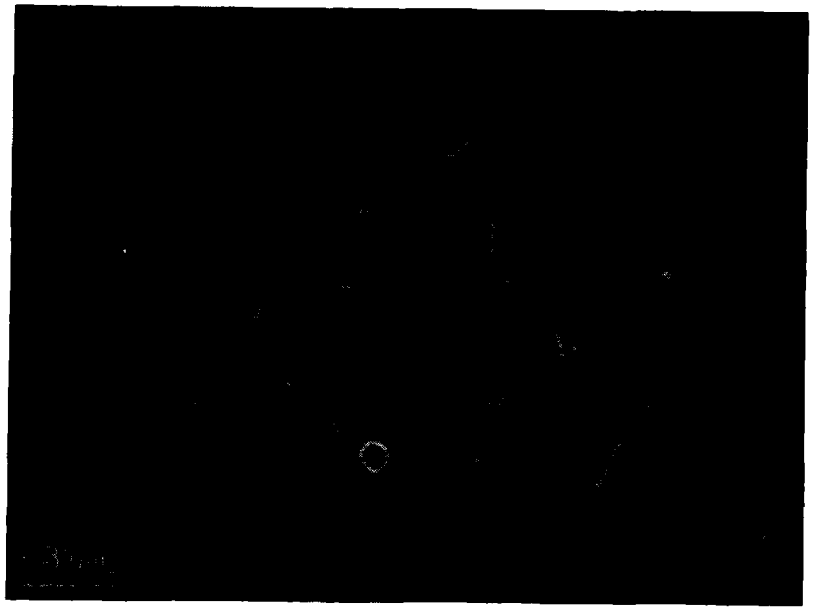

Figure 31. A side surface of the uncharged specimen in the uniformly deformed area. The slip line density is this picture is about 1.4 lines per millimeter.

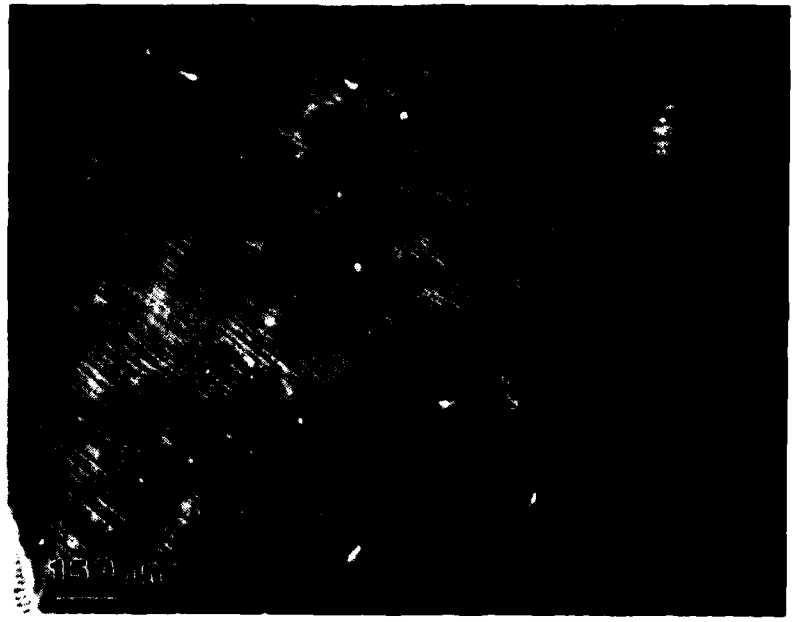

Figure 32. A uniform part of the as charged specimen. The slip line density in this picture is about 1 line per millimeter.

caused significant hydrogen absorption.

Significant differences between the slip line patterns of uncharged and charged hydrogen specimens are clearly shown. Slip lines in the hydrogen charged specimens (Figures 30 and 32) are coarser, longer, more intense and their density on the surface is smaller than in uncharged specimens. While a complete analysis of the slip line spacing was not performed, it can be seen from comparison of Figures 31 and 32 that the slip line spacing in hydrogen charged specimens is about 30% larger than in the uncharged condition. The appearance of the slip lines observed on specimens in the hydrogen charged and any of the annealed conditions was similar to those of specimens in the as charged conditions. Figures 33 and 34 give an example of the slip line pattern in the charged and 300°C annealed condition.

To compare slip patterns between hydrogen charged and uncharged specimens in conditions where almost all the plastic deformation relates to a propagating crack, two double cantilever specimens 0.25 mm thick were used. Both specimens were preannealed at 600°C and one of them was then hydrogen precharged. After crack propagation the appearance of the slip bands near the fracture surface are shown in Figures 35-38. The difference in the slip pattern between uncharged and hydrogen charged specimens can be summarized as follows. (a) The general amount of plastic deformation which accompanied crack propagation appeared to be greater in the uncharged specimens as can be judged from the slip bands distributed in large areas around the crack path. (b) The waviness of the slip pattern is much more pronounced in the as charged specimen. This could be seen at low magnifications as coarse, bundled appearing slip lines, Figure 37, and at higher magnification as more uniformly distributed wavy slip lines, Figure 38. The increase in the slip lines' waviness appeared in the hydrogen charged tensile specimens, as well as in the vicinity of the crack surfaces.

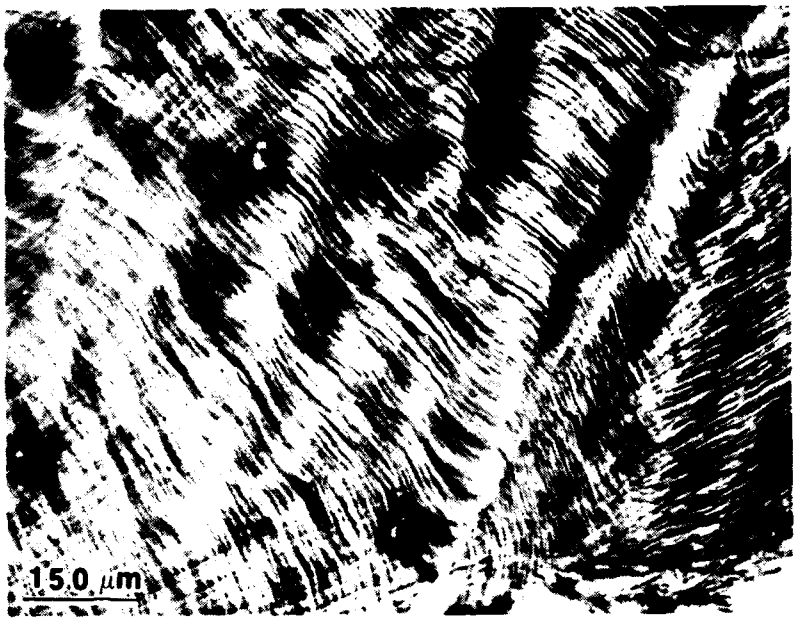

Figure 33. A side surface of the charged and 300°C annealed specimen.

Figure 34. As in Figure 33, but in more detail.

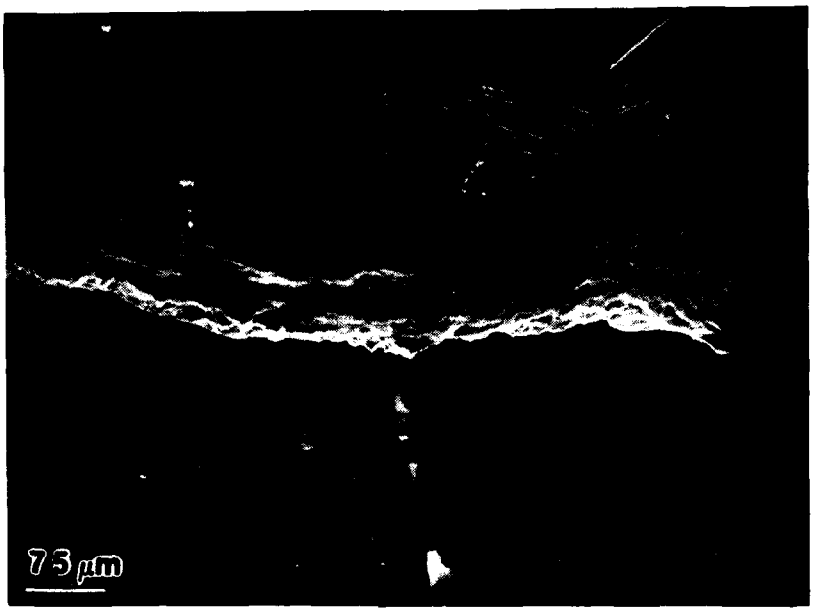

Figure 35. A side surface of the uncharged sheet in the vicinity of the crack tip. Notice intense plastic deformation spread far from the crack path.

Figure 36. More detail in the region adjacent to the crack surface.

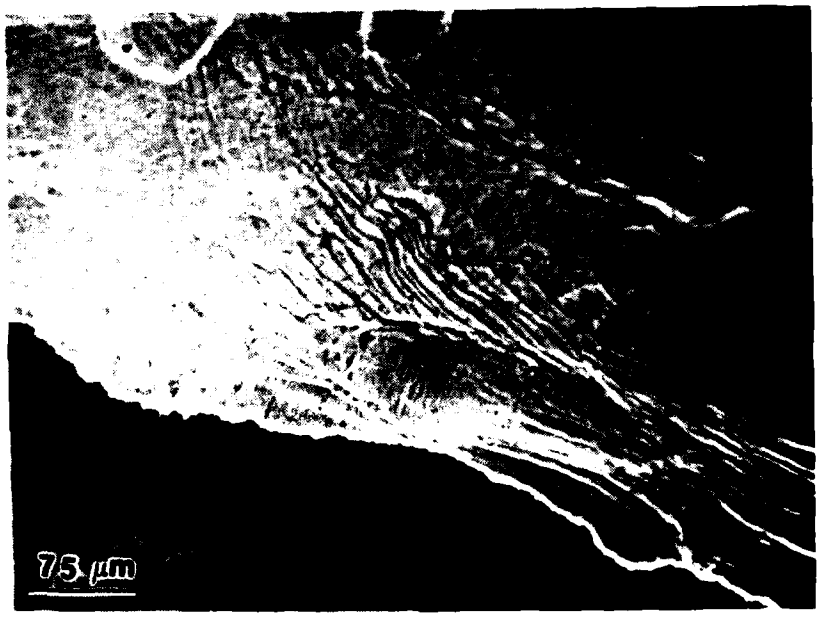

Figure 37. Slip band patterns on the side face of a hydrogen charged specimen near the fracture surface.

Figure 38. As in Figure 37, but at higher magnification. Notice coarse wavy slip lines approximately perpendicular to the crack direction.

In the case of the double cantilever beam specimens, the increase in the slip band waviness in hydrogen charged specimens compared to uncharged specimens could be clearly seen. The extent of the slip band waviness related to the ease of cross slip and, therefore, suggests that hydrogen promotes cross slip. This conclusion is consistent with the softening observed in hydrogen precharged tensile specimens as the greater the extent of cross slip, the lower is the strain hardening. Another softening mechanism will be discussed later in section 5.4.

An additional example of the intense bundled like slip line pattern in hydrogen charged specimens is given in Fig. 39. In this case the pattern was observed at the tip of a secondary non-propagating crack in a Type I unnotched hydrogen precharged specimen.

4.3.2.2 Specimens with an initially small grain size

The surface relief on samples which were recrystallized at room temperature was much shallower compared to that observed on large grained specimens which were preannealed at 600°C. The major reason for this observation is probably that a much smaller deformation to failure is observed in the small grain specimens. Basic differences between uncharged and either as hydrogen charged or hydrogen charged and cold rolled specimens were the extent of localization of the plastic deformation. Surface relief resulting from plastic deformation was difficult to resolve in the uncharged specimen group, suggesting a uniform slip distribution. The slip pattern was clearer on the surface of the uncharged specimens tested at higher strain rates, e.g. 6.4×10^{-4} sec^{-1} compared to 6.4×10^{-7} sec^{-1}. An example of the deformation surface relief for the uncharged specimen is given in Figures 40 and 41 at a

Figure 39. Coarse slip pattern at a crack tip marked with an arrow in a Type I specimen tested in laboratory air at 2.55×10^{-5} mm/sec. The specimen has been precharged in NaOH solution. The original thickness of 0.5 mm was reduced to 0.4 mm during the precharging.

Figure 40. Uncharged specimen tested at 6.4×10^{-4} sec^{-1}. Appearance of the slip bands on the uniform part of the gauge length.

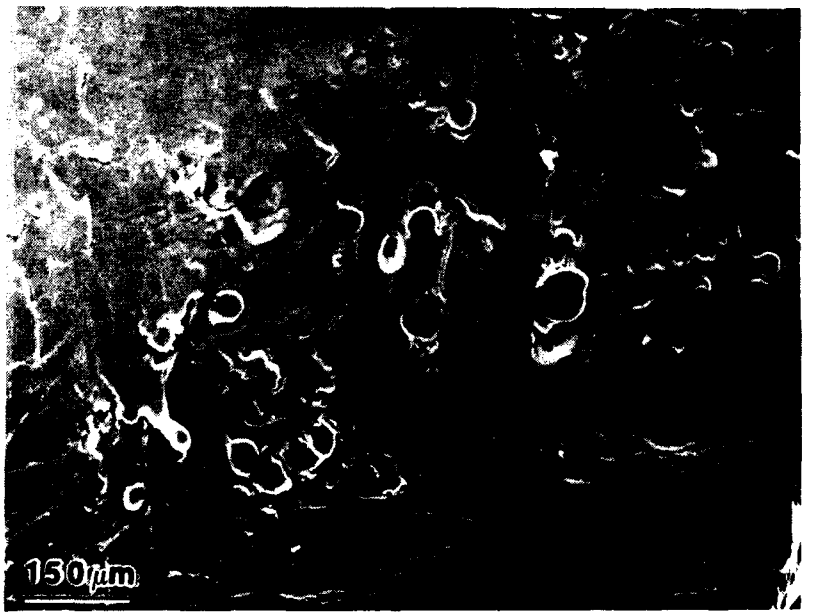

Figure 41. Same specimen as in Figure 40. The distance from the fracture is 0.4 mm and the specimen is in the necked region. The slip bands are more pronounced compared to those in the region of uniform strain.

strain rate of 6.4×10^{-4} sec^{-1}. As already discussed, intense slip band formation was observed in the as hydrogen charged and cold rolled specimens as shown in Figure 42. This type of highly concentrated bands was seen at the higher strain rates as well but these specimens also exhibited more diffuse bands (Figure 43). The distribution of deformation on the uniform part of the as charged specimen was highly non uniform as shown in Figure 44, and no long slip bands were found at strain rates of 6.4×10^{-7} sec^{-1}. The large amount of local deformation seen in Figure 44 appears to delineate a large grain grown during the charging period. At higher strain rates, 6.4×10^{-4} sec^{-1}, slip bands appeared on the as charged specimens as shown in Figure 45. In the slip region shown in Figure 45 it is possible to trace between wavy, braid like coarse slip bands and patches of parallel finer slip lines which extend through several grains.

Since hydrogen affects both fracture and the plastic deformation, the question arises about the relation between the fracture path and the slip bands. Observations made on several cracks suggest that cracks propagated along the edges of intense slip bands in hydrogen charged specimens as shown in Figures 46 and 47. This conclusion is supported by the micrograph, Figure 39, where the crack is located on one side of the coarse slip band. Such preferential crack paths could be rationalized in terms of stress concentration at the border between the concentrated slip band and the adjacent less deformed region. Another possible factor is the lattice rotation which occurs within slip bands and which gives rise to stresses at the border between the rotated and unrotated lattice. The stresses in such regions can assist crack propagation.

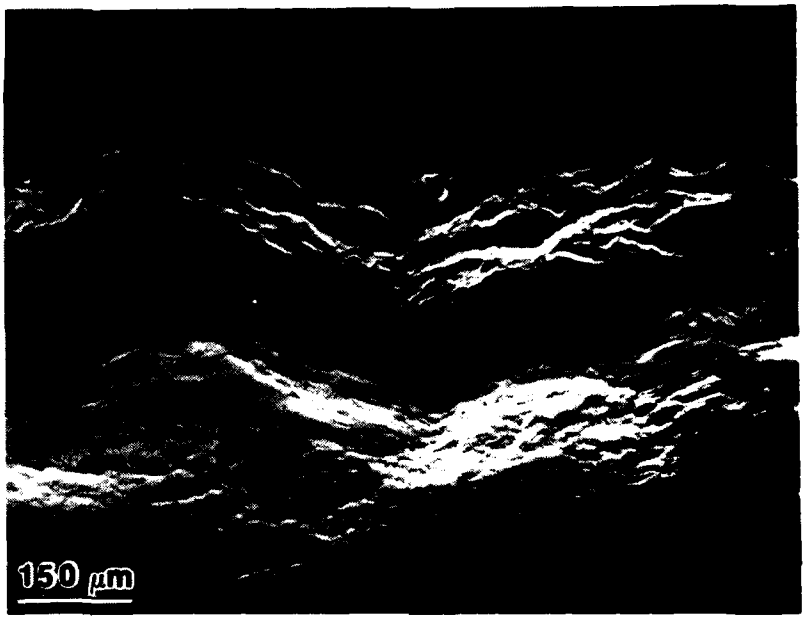

Figure 42. A slip band region in a hydrogen charged and cold rolled specimen tested at 6.4×10^{-7} sec^{-1}. The tensile axis is vertical.

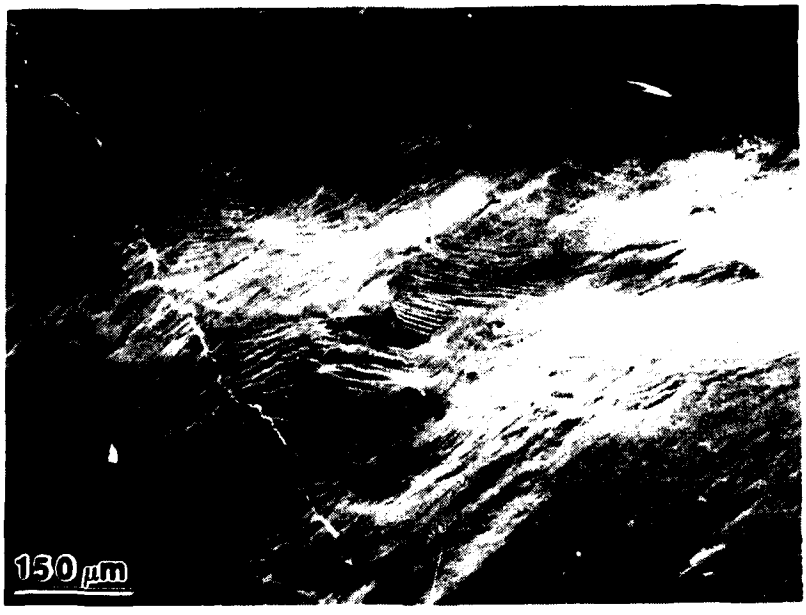

Figure 43. A slip band region in a hydrogen charged and cold rolled specimen tested at 6.4×10^{-4} sec^{-1}. The tensile axis is vertical.

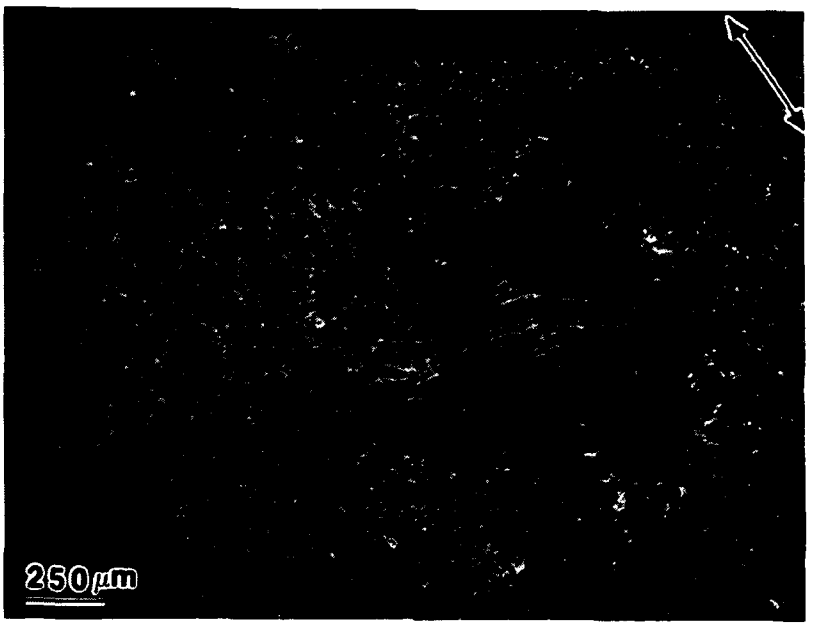

Figure 44. Uniform part of the as charged specimen tested at 6.4×10^{-7} sec^{-1}. Notice strong local deformation which probably developed in a large grain. Tensile axis marked with an arrow.

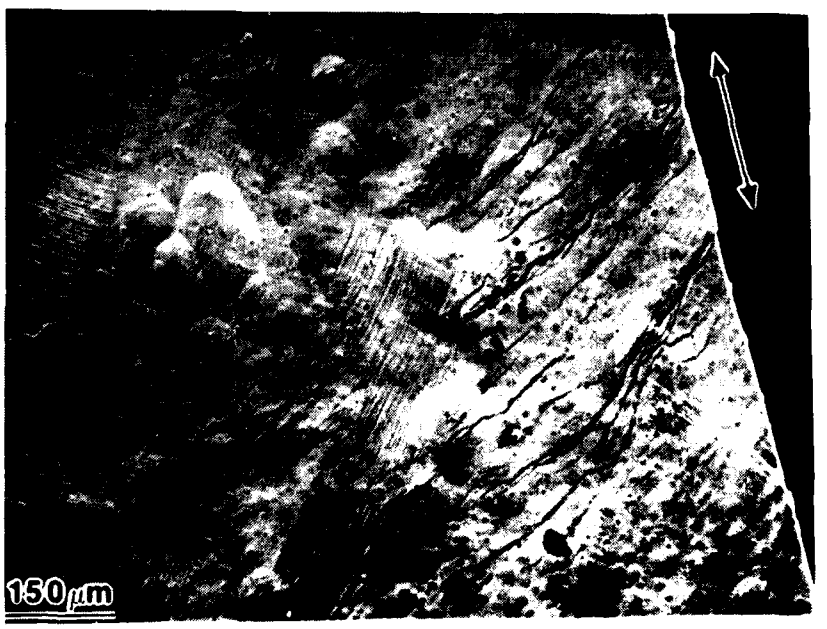

Figure 45. Slip bands on the uniform part of the as charged specimen tested at 6.4×10^{-4} sec^{-1}. Notice the coarse slip line alternating with patches of finer parallel slip lines lying about 45° to the tensile axis. Tensile axis is marked with an arrow.

Figure 46. As charged specimen tested at 6.4×10^{-7} sec^{-1}. Notice that the crack propagates in the border region between slip band and the more uniformly deformed region.

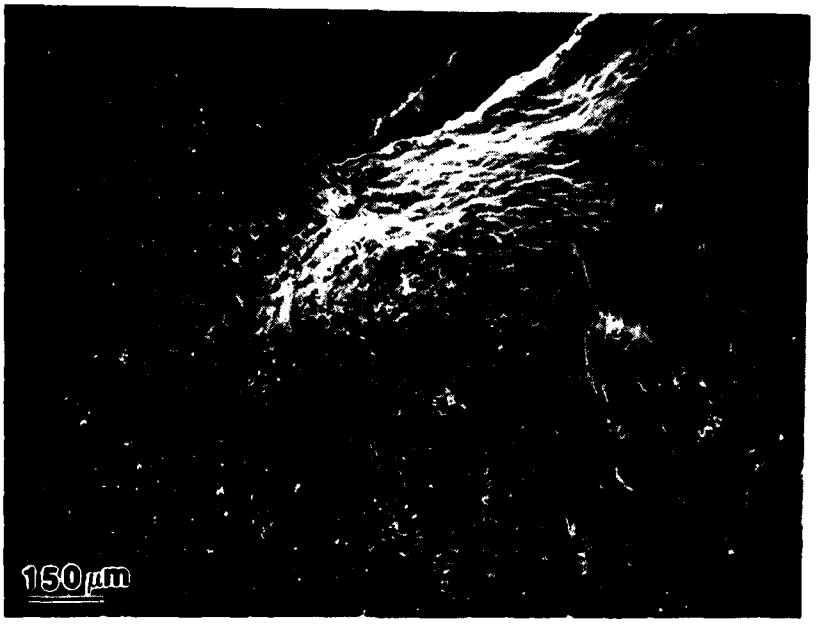

Figure 47. Another example of the crack propagating along the edge of an intense slip band in an as charged specimen tested at 6.4×10^{-7} sec^{-1}.

4.3.3 Fracture appearance

4.3.3.1 Pre-charged large grain size specimens

Reductions in cross sectional areas at fracture were measured at low magnifications and are given in Table 2 of section 4.3.1.1. These are in qualitative agreement with the SEM observations.

A majority of the fracture surfaces, including those for uncharged specimens, appeared to be covered with a film, probably resulting from mechanical damage. Some typical examples are given in Figures 48-50. All of the fractures were ductile in nature. The surface film could not be removed by prolonged cleaning in the ultrasonic cleaning bath. The film had a very different secondary electron yield in the SEM than that which characterizes the metal adjacent to the fracture. As will be discussed later in Section 5.4, it appears that this film results from mechanical damage similar to that of fretting corrosion. In one case, black colored product in silicone oil that coated a side surface was observed coming out of the crack tip. It is known that product of fretting wear in aluminum alloys is a black powder, mainly containing aluminum oxide. If so, the film should be composed of aluminum and aluminum oxide as is consistent with the lower secondary electron yield observed. No damage or films on the fracture surfaces were found in the small grain size specimens. This observation will be discussed further in Section 5.

4.3.3.2 Specimens with small grain size

A greater reduction of area at fracture was observed for small grain size specimens as compared to those of large grain size specimens. Uncharged specimens fractured with a chisel point fracture or one very close to a chisel point (Figure 51). Charged and cold rolled specimens fractured in a

Figure 48. Fracture "A" and a side surface "B" of the uncharged specimen preannealed at 600°C. The fracture surface looks damaged and covered by a film.

Figure 49. Fracture surface of a specimen preannealed at 600°C and charged with hydrogen. The fracture surface is of the shear type and exhibits small dimples.

Figure 50. Fracture surface of a specimen preannealed at 600°C, charged with hydrogen and postannealed at 200°C. A surface film "A" covered the surface. This film remained unchanged after ultrasonic cleaning in hot acetone in ten minutes.

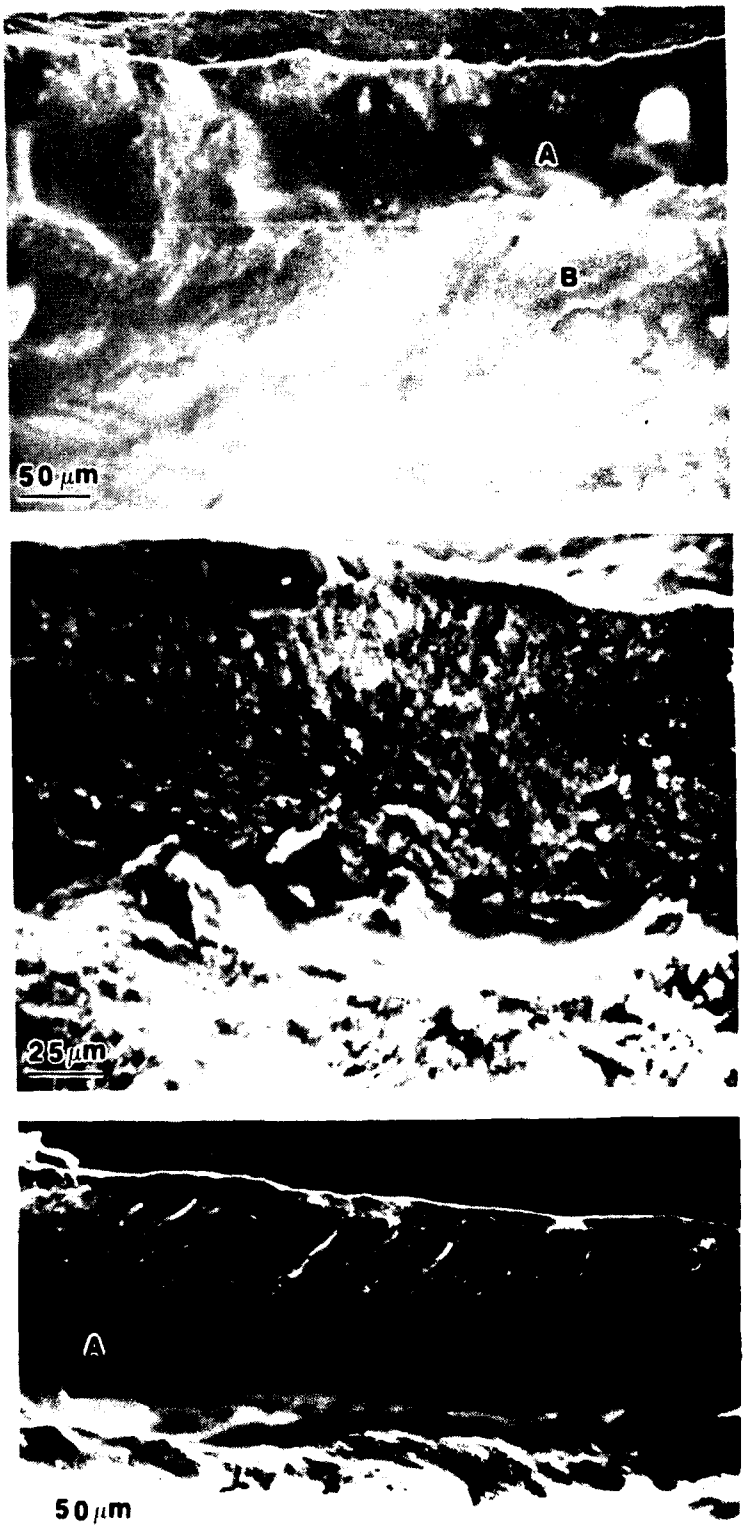
A
B
50 μm
25 μm
A
50 μm

Figure 51. Small grain size, uncharged specimen tested at 6.4×10^{-7} sec^{-1}. The fracture marked with arrows was a chisel point type of fracture.

Figure 52. Charged and 50% cold rolled specimens tested at a strain rate of 6.4×10^{-7} sec^{-1}. The specimen is tilted to allow the fracture "A" and side surface "B" to be seen.

Figure 53. Fracture surface of Figure 52 shown at higher magnification. This fractograph resembles that seen in dynamically charged specimen; compare to Figure 12.

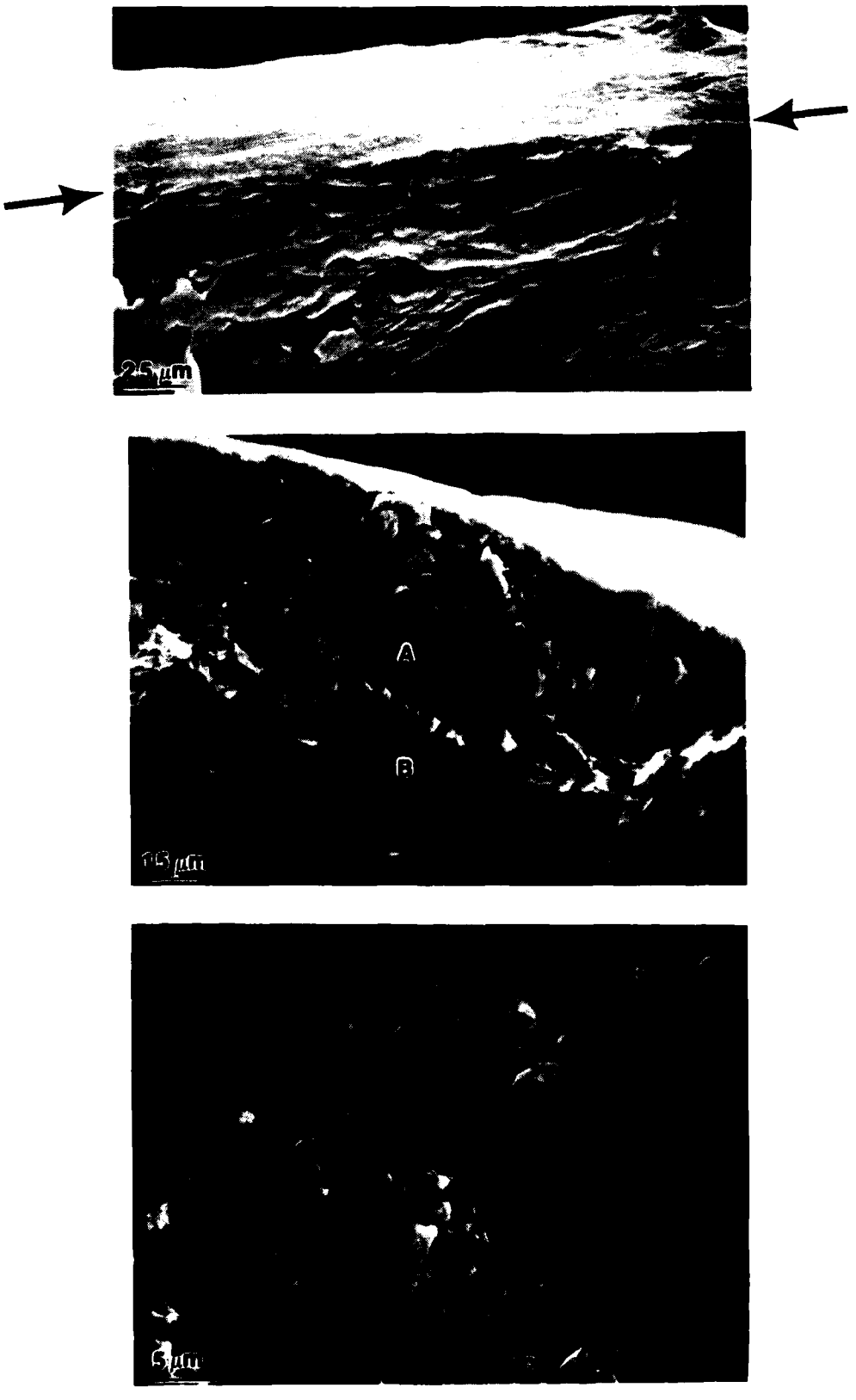
2.5 µm
A
B
5 µm

transgranular ductile manner (Figures 52 and 53). Fracture of the as charged specimens was preceded by a large amount of localized strain, i.e. necking. However, once the fracture was initiated it was accompanied by a very limited amount of macroscopic deformation as can be judged from the large proportion of intergranular fracture (Figures 54 and 55). Grains observed on the fracture surface are small, smaller than those originally present. These grains probably resulted from recrystallization during the tensile test. All the specimens tested at 6.4×10^{-4} sec^{-1} exhibited a chisel point type of fracture.

4.4 Grain growth during hydrogen charging

During examination of the slip markings produced by tensile deformation of specimens which were recrystallized at room temperature and charged with hydrogen, unusually large grains were observed. Many grains had diameters of about 1 mm whereas the as-recrystallized grain size was 0.2 mm as revealed by anodization in 2% fluoboric (HBF_4) acid. The process of revealing the grains was technically not easy. The best results were obtained in the largest sheets with the distance between anode and cathode about 10 mm, applied voltage of about 40 V and an anodization time of about 3 min. We found that saturation of the anodizing solution with aluminum ions (aluminum scrap was put in solution) improves the results. Under polarized light, grains appeared colored differently and on black and white photographs they appear as dark and light areas. Examples of the grain structure as revealed by the anodization and observed under polarized light are given in Figures 56-58. Some of the grain contrast remained almost unrevealed in these black and white pictures. Extended dark areas, especially in Figure 57 contained other grains when observed under polarized light.

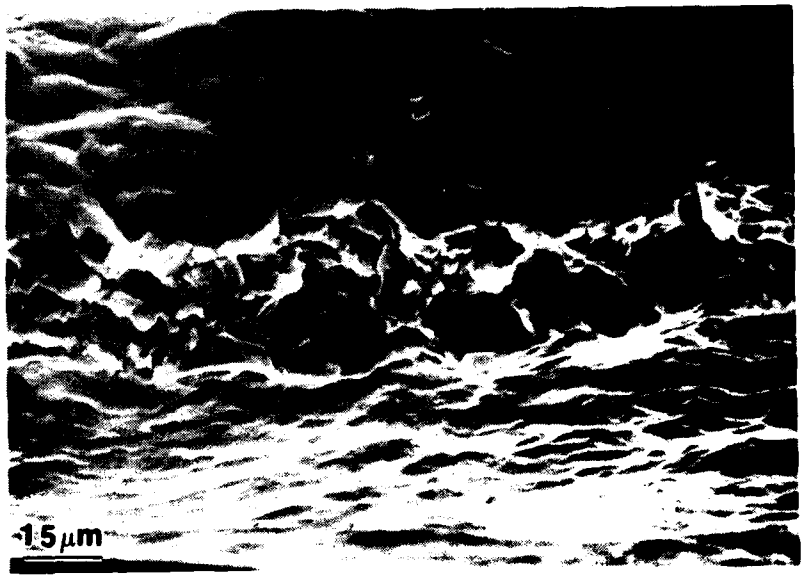

Figure 54. As charged specimen tested at a strain rate of 6.4×10^{-7} sec^{-1}. A mixed transgranular and intergranular fracture is observed. The reduction in thickness at the fracture surface is greater than 70%.

Figure 55. The fracture surface of Figure 54 at a higher magnification.

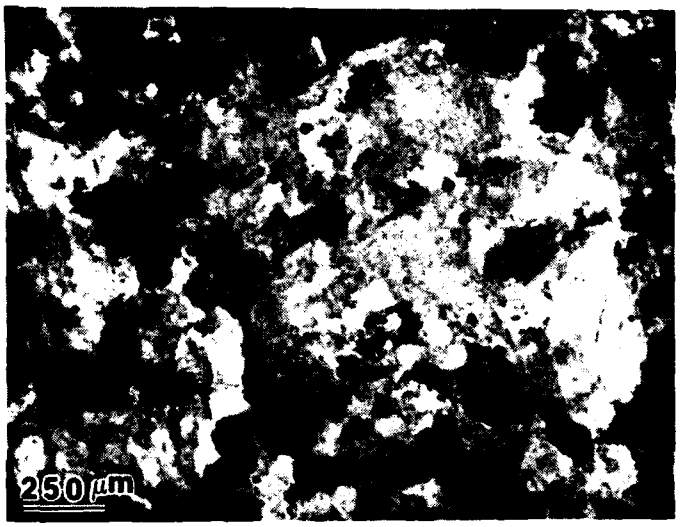

Figure 56. Grain structure of the cold rolled uncharged sheet.

Figure 57. Grain structure of the cold rolled and charged sheet. The surface topography formed in the charging process is seen as irregular fine structure.

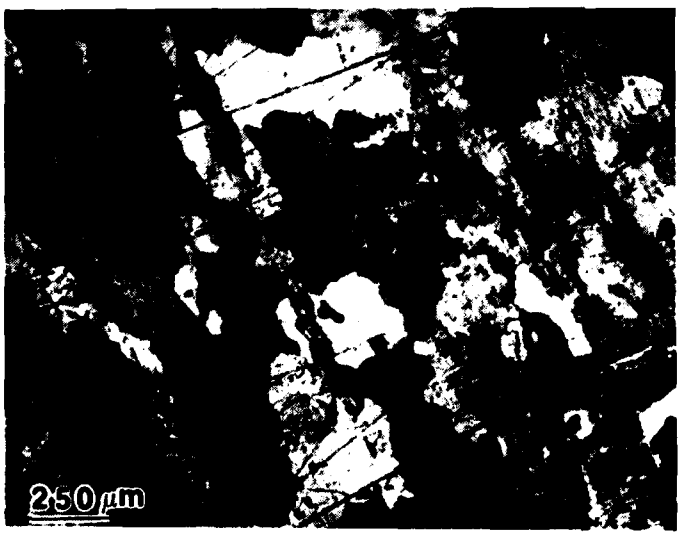

Figure 58. Grain structure of the charged and then cold rolled sheet with a 50% reduction of thickness.

On many occasions very large grain like structures have been revealed after the anodizing treatment (Figure 59). These structures, however, did not correlate with the surface slip line structure produced by tensile deformation and were assumed to be persistent impurity related cell structures formed in the solidification process (13).

No grain growth was observed in specimens which were preannealed at 600°C and then charged with hydrogen. These specimens had an initial grain size of 1.5 mm which was 3 times the sheet thickness and hence the annealed grain structure was quite stable. No large grains were observed when hydrogen charging was followed by cold rolling with a 50% thickness reduction and recrystallization occurred at room temperature. This grain structure appeared fully recrystallized, Figure 58, with a grain size about equal to that produced on recrystallization at room temperature in the absence of solute hydrogen. Thus the effect of hydrogen on the recrystallized grain size appears to be significant only during the introduction of hydrogen into the recrystallized structure, Figure 57. The grain growth during hydrogen charging cannot be attributed to the temperature rise due to corrosion reaction in the pH 12 NaOH solution. The reaction was not violent and the solution always remained at room temperature. To confirm that no heating of the samples occurred, one sheet was left in the solution with a portion extending above the solution level. No temperature rise could be detected in the extended part of the aluminum specimen.

Grain boundaries act as sinks for supersaturated vacancies and vacancy absorption at the grain boundaries has been shown to cause grain boundary motion (56). The above observations of grain growth during hydrogen charging of specimens recrystallized at room temperature can be rationalized on the basis of a high vacancy supersaturation formed by vacancy injection from the

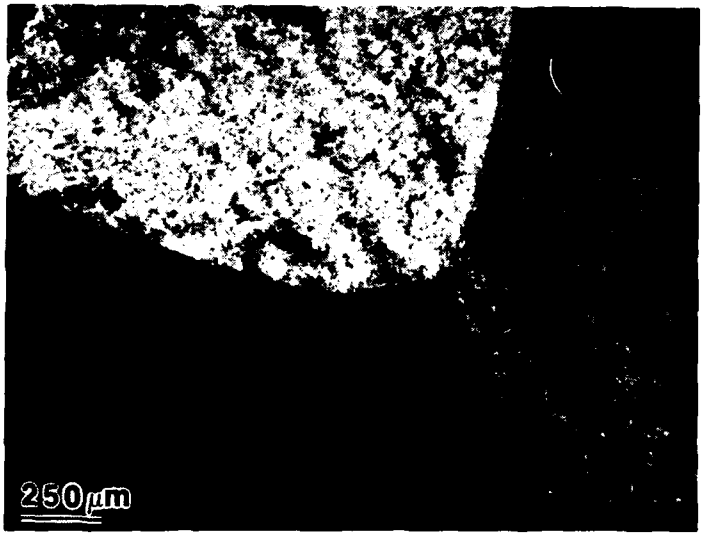

Figure 59. Example of the large "grain like" structure that is not related to the actual grain size. Each of the three blocks seen in the picture was more than 5 mm in diameter.

surface during the corrosion process which introduces hydrogen into the specimen. In the specimens which were recrystallized at room temperature and then hydrogen charged, absorption of vacancies at the grain boundaries could be expected to cause exaggerated grain growth as observed. Exaggerated grain growth is not expected, nor observed in specimens which had been recrystallized at 600°C as these had large diameter grains and a very stable grain structure (grain sizes equal to about 3 x the sheet thickness).

4.5 Measurement of Linear Dimensional Change During the Hydrogen Charging Process

In view of the large hydrogen concentrations in the charged specimens, it was important to ascertain the manner by which hydrogen is accommodated in the aluminum lattice. Hydrogen atoms in interstitial positions are expected to cause an expansion of the surrounding lattice (57). This lattice expansion can, in principle, be revealed by measuring shifts in the position of x-ray diffraction peaks. In the present experiments, lattice parameter changes were studied in hydrogen precharged specimens and during the charging process using in-situ charging methods. No changes in the x-ray peak positions have been observed. Since no data concerning the volume change due to dissolved hydrogen are available for aluminum, we estimated the necessary precision required for the x-ray peak position measurement using pertinent data for other metals. It has been found for many other metals that the volume expansion per hydrogen atom is 2.8 A^3 (57). The average volume per aluminum atom is 16.64 A^3 which results in a relative lattice expansion per hydrogen atom of 0.175. Since the linear expansion is one third of the relative volume

expansion a hydrogen concentration of about 10^{-3} results in $\Delta a/a = 5.8 \times 10^{-5}$. From the relation, $\delta\theta = \frac{\delta d}{d}/\tan\theta$, where θ is the Bragg diffaction angle and d is the diffracting atomic plane spacing, detection of $\delta d/d = 5.8 \times 10^{-5}$ requires an angular precision for the (111) reflection of $\delta\theta = 10^{-4}$ radians. This required precision is greater than that readily available with the available apparatus.

As a result the linear dimension change was measured directly, using a travelling optical microscope with a measuring resolution of 0.01 mm. The required 10^{-4} precision is thus obtained for a measuring length of 100 mm. Several 0.1, 0.15, 0.20 and 0.25 mm thick strips were prepared in the form shown schematically in Figure 60. The strips were placed between perforated parallel plexiglass plates which served to keep the aluminum specimens flat. The two inner strip corners served as fiducial marks and were kept above the charging solution which was an aqueous NaOH solution at a pH of 12. The area of the inner corners was painted with a lacquer to prevent corrosion. The aluminum specimens were preannealed in vacuum at 600°C. Room temperatures during the test were measured to be constant within ± 2°C. Using the coefficient of linear expansion of aluminum, 2.36×10^{-5}/°C, the $\Delta L/L$ due to room temperature fluctuation is $\approx 4 \times 10^{-5}$, too small to be measured with the technique used.

In contrast to the expansion expected to accompany hydrogen entry, a contraction was observed in all the specimens. The length change ceased after several hours, whereas specimen thinning due to aluminum solution was continuous. The greater the specimen thickness, the greater was the time to reach the saturation in the length change. The average contraction which

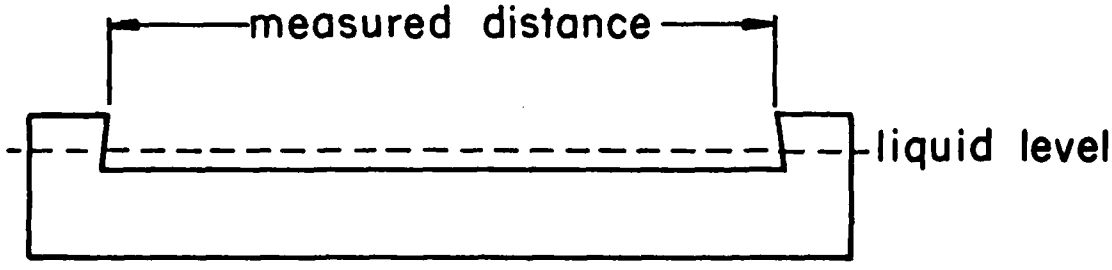

Figure 60. Schematic of the strip used for length change measurements.

resulted from hydrogen charging was $\Delta l/l = 3 \times 10^{-4}$ and was independent of the specimen thickness.

Both the contraction and its saturation during hydrogen charging can be rationalized based on a model in which hydrogen atoms are generated by reaction of aluminum with the H_2O at the surface in the absence of an oxide film while simultaneous formation of vacancies occurs. At the surface of the specimen the vacancy formation can occur without interstitial formation as the atom can be added to the lateral surface where it does not contribute to the length change. The hydrogen interstitials can be expected to form complexes with the vacancies (15) and are expected to diffuse in from the surface coupled with a vacancy (10).

Vacancies can also be formed by the oxide growth process as discussed in Section 5. In this case vacancies are trapped by single hydrogen ions that diffuse from the external surface through the oxide.

The volume change due to the vacancy formation in the above process is given by:

$$\frac{\Delta V}{V} = -C_V \delta_V$$

where $\Delta V/V$ is the fractional volume change

C_V is vacancy concentration

δ_V is the volume change due to material relaxation around the vacancy.

Since both hydrogen and vacancies are introduced, the volume change is given by:

$$\frac{\Delta V}{V} = C_H \delta_H - C_V \delta_V$$

and the length change by:

$$\frac{\Delta L}{L} = \frac{1}{3} (C_H \delta_H - C_V \delta_V) \qquad (A)$$

where C_H is the hydrogen concentration and δ_H is the volume change due to relaxation around the H interstitial. Aluminum specimens yielded values for C_H = 1,200-1,400 appm. Using the value of δ_H = 0.175 and δ_V = 0.49 (73,74), the measured value of $\Delta L/L = -3 \times 10^{-4}$ yields (from Eqn. A) $C_V = 2.3 \times 10^{-3}$ and $C_V/C_H \approx 1.8$.

The above should be regarded as order of magnitude estimates as values of the lattice relaxation around the hydrogen interstitial in aluminum and details of the hydrogen-vacancy configurations are not known. Furthermore the model did not account for precipitation of hydrogen atoms and vacancies into large clusters as has been suggested by the preliminary SAXS results. Formation of vacancy clusters from isolated vacancies is expected to result in a decrease in the volume if Frank loops are formed. In view of these uncertainties, additional measurements, performed at higher precision and at various temperatures are required and in progress.

One other process that can cause material contraction during hydrogen charging in alkaline solution is surface oxide dissolution. Aluminum oxide possesses a smaller density than metallic aluminum and therefore the surface oxide is elastically stressed in compression and the aluminum lattice beneath the oxide is elastically stressed in tension. Dissolution of the oxide would bring about elastic relaxation and resulting contraction. However, this

contraction is expected to be much smaller than that measured in these experiments. The oxide is of the order of 5-10 nanometers in thickness and hence can support stresses in the aluminum only near oxide surface. Hence, the length changes observed should be sensitive to the specimen thickness, which was not observed. Furthermore, changes in length due to oxide dissolution should be essentially instantaneous whereas the observed $\Delta L/L$ changes were observed to occur as a function of time. Based on these preliminary measurements, the formation of hydrogen-vacancy complexes appears to be the most consistent explanation of the observed contraction during the charging process.

5. DISCUSSION

5.1 Source of Hydrogen

In all our experiments hydrogen was introduced into the metal from aqueous solutions. In the following discussion we address the mechanism of hydrogen entry into aluminum. The equilibrium equation for hydrogen solubility extrapolated from high temperature measurements (1) is:

$$\log S = -\frac{2080}{T} + 0.788 + \frac{1}{2}\log f_{H_2} \qquad (1)$$

where S = solubility in $\frac{cm^3}{100\ g\ Al}$ and

f_{H_2} = hydrogen fugacity in atm.

After substitution of a typical value of 53.54 $\frac{cm^3}{100\ g\ Al}$ (1,300 appm) for S, Equation 1 indicates a fugacity of $10^{15.84}$ atm is necessary to charge 1,300 appm of hydrogen into aluminum at room temperature. As the aqueous solution is the source of hydrogen, the hydrogen gas pressure in equilibrium with aqueous solution for any particular corrosion potential should be calculated. Hydrogen evolution reaction from solution and its electrochemical reversible potential may be expressed as:

$$H_2 = 2H^+ + 2e^- \qquad (2a)$$

$$E_o = -0.0591\ pH - 0.0295 \log f_{H_2} \qquad (2b)$$

where pH is the pH of the solution. When no corrosion takes place, the equilibrium hydrogen fugacity above the solution is very small. This

implies that immersion of aluminum in an aqueous solution will result in little hydrogen charging in the absence of an applied cathodic potential if no corrosion takes place.

The possible corrosion reactions of aluminum can be considered using reference (55) for all necessary data. According to the Pourbaix diagram for aluminum, the stable product in the alkaline solution is the AlO_2^- ion. The possible corrosion reactions leading to this product are:

$$Al_2O_3 + H_2O = 2AlO_2^- + 2H^+ \quad (3)$$

$$Al^{+++} + 2H_2O = AlO_2^- + 4H^+ \quad (4)$$

$$Al + 2H_2O = AlO_2^- + 4H^+ + 3e^- \quad (5)$$

Reactions (3) and (4) do not produce electrons as necessary for hydrogen ion discharge and therefore cannot account for hydrogen charging. Reaction (5) results in a cathodic potential and hence can result in hydrogen entry into aluminum. This reaction implies a bare aluminum surface corroding in an alkaline solution. While the existence of a bare aluminum surface at the bottom of a surface pit was postulated (75), the presence of oxide (or hydroxide) was expected and found experimentally on "flat" corroding aluminum surfaces (76,77). The surface layer which resulted from different corrosion conditions (cathodic polarization in low pH chloride solution, exposure to distilled water at 373 K and prolonged etching in a 1.5 mol. l^{-1} sodium hydroxide solution at 293 K) was of duplex nature. The outmost layer, loosely connected to the surface, was assumed to grow by dissolution and precipitation from the aqueous solution. The inner layer, adherently connected to the aluminum substrate, was assumed to form by a solid-state reaction (76,77).

The solid-state reaction presumes that Al^{+++}, $(OH)^-$ and H^+ ions diffuse through an oxide film prior to a chemical reaction.

Under the above conditions, the corrosion dissolution of aluminum can be considered as a process involving oxide (or hydroxide) formation and its subsequent dissolution, with the latter step, described by reaction (3), bringing about a thermodynamically stable product AlO_2^-. It appears that the former step, which results in a thermodynamically unstable product, is responsible for the hydrogen charging according to the following reaction:

$$Al + 3H_2O = Al(OH)_3 + 3H^+ + 3e^- \qquad (6a)$$

with a reversible potential

$$E_o = -1.471 - 0.0591\ pH \qquad (6b)$$

The reversible potential of reaction (6a) in our charging solution of sodium hydroxide with pH 12 is -2.18 V, as derived from Eq. (6b). Such a reversible potential would provide very high equilibrium hydrogen fugacity, $f_{H_2} = 10^{49.86}$ atm, as calculated from Eq. (2b). However, the actual cathodic potential of the corrosion reaction is defined by the hydrogen evolution process;

$$2H^+ + 2e^- = H_2.$$

According to Equation (2b) at $f_{H_2} = 1$ atm (atmospheric pressure), the reversible hydrogen potential for the hydrogen evolution reaction is about -0.71 v. If this reaction has occurred at the reversible potential, it would

result in an equilibrium hydrogen fugacity of 1 atm and practically no hydrogen charging would take place. The reaction of hydrogen evolution at a metallic surface occurs at a potential lower than the reversible cathodic potential; the deviation of the actual potential of the hydrogen evolution reaction from the reversible potential is called hydrogen overpotential. Aluminum belongs to a group of metals with a large overpotential (55) . The hydrogen over-potential varies with the rate of the corrosion reaction; the faster the reaction, the larger the hydrogen overpotential is. As was estimated from Equation (1), we need to attain a hydrogen fugacity of $10^{15.84}$ atm necessary to charge 1,300 appm of hydrogen in aluminum, equivalent to a hydrogen potential of -1.18 v as calculated from Equation (2b). This implies about -0.47 v of overpotential (-1.18 v-(-.71)v = -0.47v). From the diagram connecting the hydrogen overpotential to the corrosion rate (p. 116 in Ref. (55)) we deduced that a -0.47 v overpotential can be expected for the fast corrosion reaction of aluminum as expected for the charging conditions used (an active alkaline solution stirred mechanically). The above calculation of the necessary overpotential should not be overemphasized because we extrapolated Eq. (1) obtained in a high temperature range to the room temperature; a procedure that almost inevitably causes a significant error.

In the case of charging in pure water (pH = 7) with application of weak ultrasonic oscillations, the driving force for hydrogen entry is still a corrosion reaction. The role of the ultrasonic field is to provide disruption of the passive oxide film and to allow corrosion to proceed. The disruption of the protective oxide is provided by cavitation erosion; that normally used for surface cleaning and for which the ultrasonic bath was designed. When ultrasonic fields were applied in either the alkaline or acidic pH range, no

increase of the hydrogen concentration in the charged aluminum was observed due to the ultrasonic oscillations. The hydrogen content of specimens charged using the aqueous NaOH or acidic technique without an applied ultrasonic field was always higher than that obtained when an ultrasonic field was used for otherwise the same charging conditions.

It may be expected that cathodic polarization should provide a driving force for hydrogen charging and hence no corrosion process should be necessary to attain high hydrogen concentrations in solid solution.

It was reported, however, that a hydrogen pre-embrittlement effect in a 7075 aluminum alloy was observed after cathodic precharging only in those cases which were accompanied by surface corrosion and pre-embrittlement was not found if no surface dissolution took place (60). One possible explanation of this finding is based on a possible reduction in the enthalpy for solution of hydrogen in aluminum when vacancies are produced in corrosion reaction. This effect will be considered in Section 5.2.

A few comparative experiments were made in which charging in HF and HCl solutions were compared to charging in sodium hydroxide solutions. Corrosion of 0.5 mm thick aluminum in an aqueous NaOH solution at pH = 12 for about 12 hours resulted in a hydrogen concentration of 1,000-1,500 appm. Charging under similar conditions in a solution of HF or HCl at a pH = 1.5 resulted in a hydrogen concentration of 200-300 appm. However, the aluminum used in these experiments was stored over a long period of time in laboratory air (since 1961) and were not vacuum annealed prior to tests. As was found later, about 200 appm of hydrogen was present in the stored material, probably due to corrosion reaction with humid air. In view of this finding, actual hydrogen charging from acid solutions could be much smaller than that determined from

hydrogen analysis. Reasons for such a different hydrogen charging ability of acid and alkaline solutions are unknown.

5.2 The State of Hydrogen in Aluminum

As was mentioned earlier in Section 2, there is direct experimental evidence of a hydrogen bound to a vacancy in the aluminum lattice (17). However, the exact value of the bonding enthalpy between a hydrogen atom and a lattice vacancy is unknown and different values of H_B(H-Vac) in the range of (0.5-1.0) eV were suggested from theoretical calculations and interpretations of experimental results (10,15,16,78). The most recent result is H_B(H-Vac) = 0.5 eV (78). If the hydrogen-vacancy binding enthalpy is higher than the vacancy formation enthalpy, H_f(Vac) = 0.66 eV (79), a vacancy is produced next to a hydrogen atom when it is situated at a vacancy source. In this case hydrogen atoms would induce vacancy production at bare aluminum surfaces during hydrogen charging as shown schematically in Figure 57a. If H_B(H-Vac) < 0.66 eV, hydrogen atoms would trap vacancies produced by any other process such as plastic deformation, radiation damage, etc. A process of vacancy production and their trapping by hydrogen atoms during surface corrosion is schematically shown in Figure 57b. In this case a vacancy is left behind an aluminum atom diffusing outward through a surface oxide film. A vacancy trapped by a hydrogen atom may disappear when the hydrogen-vacancy pair diffuses and arrives at a vacancy sink such as a dislocation, a grain boundary or a disk of collapsed vacancies. The remaining "equilibrium" concentration of vacancies trapped with hydrogen will be many orders of magnitude higher than the equilibrium concentration of vacancies in a crystal free of atomic hydrogen.

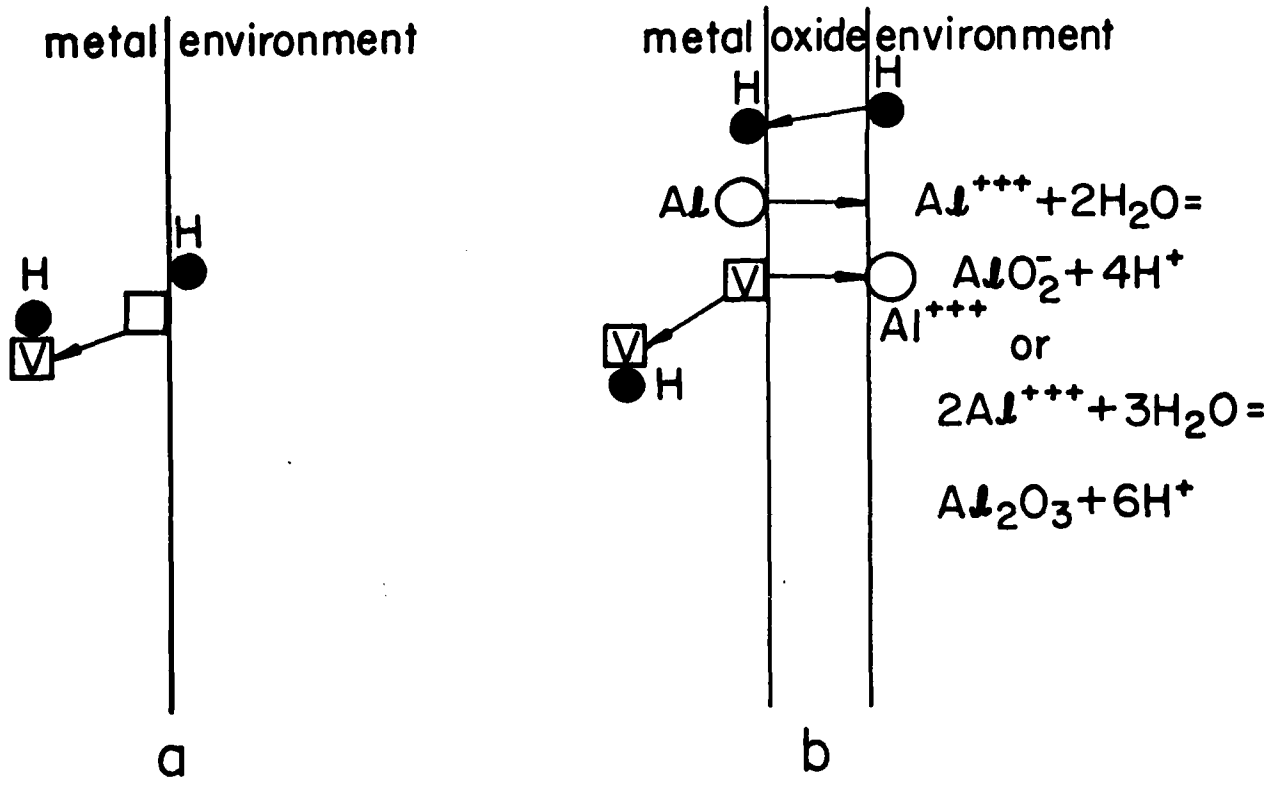

Fig. 57. Schematic of hydrogen atom-lattice vacancy pair formation at an aluminum surface.

Assuming that the equilibrium concentration of free vacancies is small, as appropriate for low temperature, the vacancy supersaturation due to hydrogen atoms in the solid solution at concentration C_H can be estimated as $8\ C_H \exp \frac{H_B(H\text{-}Vac)}{kT}$. The factor of 8 stems from the assumption that a single interstitial hydrogen atom resides in an octahedral position and is surrounded by 8 nearest neighbors where vacancies can reside. Adapting $H_B(H\text{-}Vac) = 0.5$ eV, the vacancy supersaturation is 2×10^3 per 1 appm of hydrogen in the solid solution at room temperature.

Two observations made in the present study bring additional indirect evidence for hydrogen-vacancy interactions. These observations are the linear shrinkage of aluminum during hydrogen charging and a finding of vacancy clusters in SAXS experiments in the interior of hydrogen charged aluminum. A high concentration of vacancies at the surface layer is produced during the corrosion reaction which introduces hydrogen into the aluminum. If the vacancies were free they would collapse into disks or voids (see Section 2) very close to the surface and no bulk effects would be observed. The linear shrinkage observed during hydrogen charging was not caused by a surface phenomenon as shown in section 4.5. Vacancies bound to hydrogen atoms are expected to be stabilized and diffuse to the interior of the charged aluminum where they can cause the decrease of $\Delta L/L$ as previously discussed.

Observation of grain growth during the corrosion reaction, as described in Section 4.4, provides additional indirect evidence for vacancy production during hydrogen charging. The relation of this phenomenon to the hydrogen vacancy interaction is not clear since the excess vacancies produced have a poorly established or understood effect on grain growth.

The kinetics of hydrogen-vacancy diffusion in the charged specimen can be estimated using the relationship

$$(\frac{x}{2})^2 = 2\ Dt$$

where x is the sheet thickness

D is the hydrogen diffuson coefficient and

t is the charging time.

A hydrogen diffusivity of about 10^{-11} cm^2/sec can be estimated by extrapolation of diffusivities measured using permeation methods at elevated temperatures (10). This value results in a penetration distance of about 8 micrometers in 10 hrs; a value that is inconsistent with the observation that this charging time was sufficient to saturate 0.5 mm thick sheet specimens with hydrogen. Two diffusion coefficients, $2x10^{-7}cm^2/sec$ and $2.2 \times 10^{-10}cm^2/sec$, have been reported from room temperature permeation studies (10,62). The latter value recently reported is not consistent with the hydrogen charging time required to saturate 0.5 mm thick sheet as observed in the present work. The former diffusion coefficient implies that 0.5 mm thick sheet would be charged in 26 min. While the saturation time for hydrogen charging of 0.5 mm thick sheet was not established, the lower diffusivity measured at 300 K would require a charging time of 394 hours for saturation; considerably longer than experimentally observed. A diffusion coefficient in the range of $(10^{-9}$-$10^{-8})$ cm^2/sec would be consistent with our experimental observations.

Hydrogen in solid solution at the concentration introduced in the present experiments is in a thermodynamically unstable state and should eventually

AD-A171 214 EFFECT OF HYDROGEN ON THE MECHNICAL PROPERTIES AND FRACTURE BEHAVIOR OF H..(U) ILLINOIS UNIV AT URBANA DEPT OF MATERIALS SCIENCE F ZEIDES ET AL. JUL 86 2/2

UNCLASSIFIED N00014-83-K-0468 F/G 11/6 NL

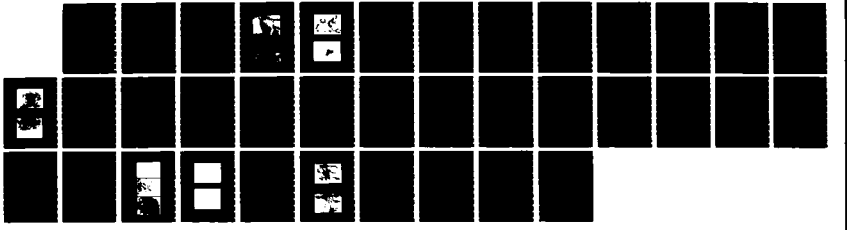

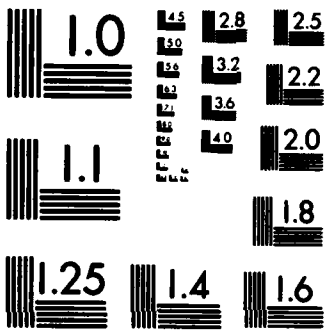

precipitate into gaseous bubbles. Vacancies clusters on (111) planes, which were found in SAXS experiments could be either a metastable phase containing atomic hydrogen or disk shaped hydrogen bubbles. The former possibility seems to be more likely since hydrogen bubbles are expected to precipitate first at the specimen surface and would provide perfect sinks for migrating hydrogen atoms, resulting in a low bulk hydrogen concentration and bubbles lying close to the surface. This was not the case since surface removal by mechanical polishing to the depth of more than 0.1 mm did not cause reduction in scattering intensity in SAXS experiments.

Regardless of the nature of hydrogen-vacancy precipitates, the solid solution concentration of hydrogen should be significantly smaller than the total hydrogen concentration. If the kinetics of hydrogen precipitation is fast enough to allow hydrogen clusters to occur during hydrogen charging one consequence is that the thermodynamical driving force to introduce 1,300 appm of hydrogen is much smaller than that estimated in Section 5.1.

In the following discussion, nucleation of hydrogen bubbles is considered using classical nucleation theory. According to this approach (61), the critical nucleation size (smallest number of vacancies to form a stable nuclei), n^* is as follows:

$$n^* = (32\ \pi\Omega^2\sigma^3)/3[kT \ln C_v/C_e + p\Omega]^3 \qquad (7)$$

where Ω = surface energy, 16.6×10^{-30} m^3

σ = surface energy, 1.22 J/m

C_v = vacancy concentration

C_e = equilibrium vacancy concentration

p = hydrogen gas pressure in the bubble

To calculate C_v we assume that all hydrogen is in the solid solution and each hydrogen brings one vacancy i.e. $C_v = C_H$. To calculate C_e we choose an equilibrium hydrogen fugacity $(f_{H_2})_1 = 0.5 \times 10^{-6}$ atm (81) equal to the atmosphere hydrogen fugacity. The equilibrium solute hydrogen concentration $(C_H)_1 = 5.06 \times 10^{-10}$ cm^3/100 g Al is calculated from equation (1) in Section 5.1. The vacancy equilibrum concentration is calculated as $C_e = 8\ (C_H)_e - \frac{H_f(Vac) - H_B(H\text{-}Vac)}{kT}$, where $H_f(Vac) = 0.66$ eV and $H_B(H\text{-}Vac) = 0.5$ eV. This gives $\frac{C_v}{C_e} = 6.45 \times 10^{12}$ at room temperature. The ideal gas law may be used to calculate the gas pressure in the bubble, p, leading to $p = \frac{kT}{2\Omega}$. The factor of 2 in the denominator reflects the assumption that the void is formed by vacancy-hydrogen pair condensation and one hydrogen molecule corresponds to two vacancies. The critical nuclei size, n^*, calculated from equation (7) is about 9 vacancies. This result means that homogeneous bubble nucleation in the absence of a positive binding enthalpy between vacancy-hydrogen pairs is unlikely at room temperature for experimental conditions used. The above calculations should not be overemphasized since extrapolation of Eq. (1) to room temperature almost inevitably will result in a significant error. In addition, Eq. (7) treats vacancies as independent defects, ignoring any positive binding energy between them. In fact, homogeneous bubble nucleation was observed in electron irradiation experiments at about 150 K (63). We will refer to these experiments later in this section. It appears, however, that heterogeneous nucleation is more likely to occur either at low temperatures or upon anneals following hydrogen charging. Grain boundaries are potential sites for the nucleation.

Evidence for the formation of large bubbles was obtained in the present study. Large facetted voids were observed on grain boundaries of the fractured specimens. Typical examples are shown in Figures 58-60. The

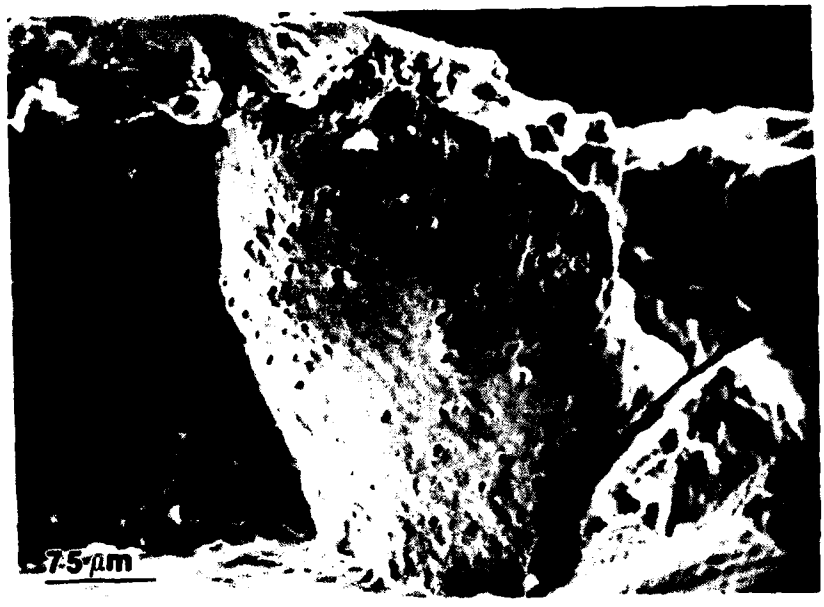

Fig. 58. Example of grain boundary fracture with facetted voids that are believed to form from preexisting hydrogen bubbles. The specimen was tested in ultrasonic water bath at a 1.25×10^{-5} mm/sec extension rate.

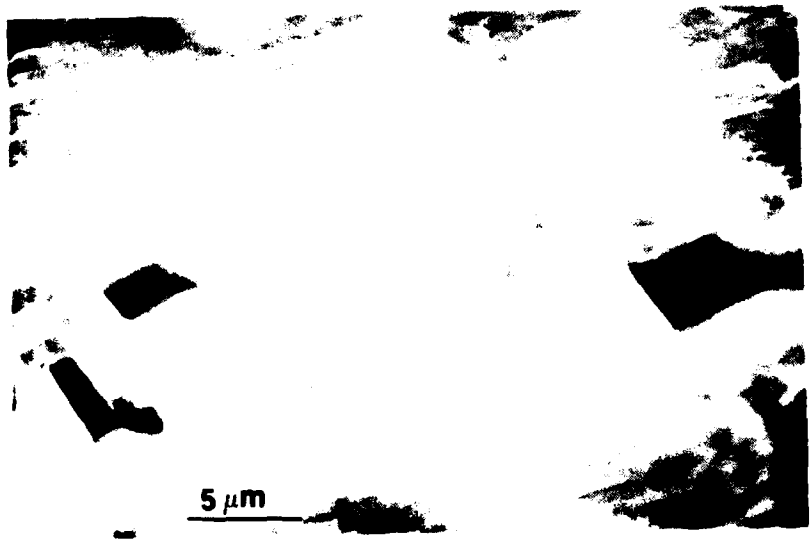

Fig. 59. An example of individual facetted voids on the grain boundary fracture surface.

Fig. 60. An additional example of facetted voids on a grain boundary fracture.

Fig. 61. A side surface of the type I specimen tested in ultrasonic water bath at a slow deflection rate of 1.25×10^{-5} mm/sec. Notice two cracks and an intense shear band which developed between them.

occurrence of hydrogen bubbles on the grain boundaries was, however, not the usual case. The tensile specimens of type I, which exhibited the grain boundary bubble formation, were prepared without a vacuum anneal at high temperatures. As was later determined, the source aluminum ingots contained about 200 appm of hydrogen as result of a prolonged storage (since 1961) in laboratory air. This material was cold rolled with intervening anneals at about 300°C. In addition to the observed facetted voids on fracture surfaces, all samples prepared in this manner revealed a great tendency towards delamination. No grain boundary voids or delamination were observed in specimens that were cold rolled without intervening anneals or which were given a vacuum anneal. We may conclude, therefore, that the hydrogen bubbles formed during the annealing periods after cold rolling and that these bubbles caused delamination during subsequent cold rolling. The formation of large facetted hydrogen bubbles on grain boundaries is facilitated by the ease of bubble nucleation at the grain boundary and the vacancies produced by cold work and during the elevated temperature anneals. The high temperature annealing is also expected to cause growth of the hydrogen bubble which is driven by surface energy.

Stimulation of hydrogen bubble nucleation by the electron beam in a transmission electron microscope, see for example Ref. (52), can be accounted for in the light of the above analysis. It was observed in the present research (and subsequently further studied (63)) that hydrogen drastically reduced the threshold for electron irradiation damage and that damage is produced at accelerating voltages as low as 80 keV; lower than commonly used in modern TEMs. Therefore, high vacancy supersaturation can be assumed to form in the hydrogen precharged samples under electron beam during TEM study. This effect

together with expected local heating is assumed to cause accelerated hydrogen bubble nucleation. The increased sensitivity of aluminum to the electron irradiation damage due to dissolved hydrogen was used to establish the hydrogen presence in the solid solution of specimens which were precharged and annealed in vacuum at 300°C. Intense electron beam induced radiation damage developed in these specimens indicating that hydrogen was still present in the lattice in significant amounts.

5.3 Hydrogen Storage

In Section 5.1 it was shown that an extremely high hydrogen fugacity is required to charge aluminum to hydrogen concentrations of the order of 1,000 appm. Therefore, a very high driving force for the loss of hydrogen is expected when the aluminum is stored in dry air or in vacuum. It was observed however, that charged specimens could be stored at room temperature for at least several weeks while retaining hydrogen at about the level of the freshly charged samples. In contrast, only a few hours were sufficient to charge hydrogen into the aluminum. One possible explanation for the above asymmetry relates to the hydrogen-vacancy clustering which results in a signficant reduction of the hydrogen solid solution concentration and, therefore, in a reduction of the thermodynamic driving force for the outgassing process. In addition, removal of hydrogen from the aluminum requires dissociation of the hydrogen-vacancy clusters. The activation enthalpy of this process is higher than migration enthalpy of hydrogen-vacancy pair and, therefore, the overall kinetics of hydrogen loss should be slower than in the absence of the hydrogen-vacancy clusters. Another possible cause for the slow degassing kinetics relates to a surface phenomena. Since the surface oxide is an ionic

compound a hydrogen-vacancy pair arriving at the lattice-oxide interface should dissociate before hydrogen atom diffusion through the oxide. The activation energy of this process in a metallic lattice is expected to be high since it is equal to the sum of the vacancy-hydrogen binding enthalpy and vacancy migration enthalpy. If the migration enthalpy of the hydrogen interstitial atom is smaller than that of vacancy it should be substituted in the sum for the vacancy migration enthalpy. We, however, don't know the migration enthalpy for hydrogen interstitial atoms. As was mentioned earlier, the binding enthalpy is of the order of 1 eV (15) or 0.5 eV (78) and the vacancy migration enthalpy is 0.62 eV (84) or 0.66 eV (80), resulting in 1.66 eV or 1.16 eV as the activation enthalpy of the dissociation process. If the lattice-oxide interface is a perfect vacancy sink, the vacancy-hydrogen dissociation enthalpy would be reduced by the value of the vacancy formation enthalpy, 0.66 eV (79). Since the lattice-oxide interface is not a perfect vacancy sink (58) the actual situation lies between the two bounds.

5.4 Influence of Hydrogen on the Plastic Deformation Process

During the deformation process hydrogen atoms either remain in the metallic lattice or form atmospheres and move with the dislocations. Hydrogen atoms in interstitial solid solution are expected to cause solid solution hardening due to the elastic interaction with moving dislocations. In the presence of other impurity atoms solution softening is possible due to relaxation of the elastic fields around the impurity atoms by trapped hydrogen atoms. Aluminum is a FCC metal and the resistance to dislocation movement by impurities is expected to contribute to the flow stress only at small strains, i.e. at the onset of plastic deformation. As our tensile test equipment was

not suited for precise yield stress determinations, no conclusions can be drawn about possible hydrogen effects in this small strain range.

In addition to interstitial solute hydrogen, atmospheres of hydrogen are expected in the vicinity of the dislocations. The binding enthalpy between hydrogen and dislocations is not known, but the binding enthalpy between grain boundaries and hydrogen atoms was estimated to be 0.15 eV from solubility data (14). This value can be taken as characteristic of the hydrogen-dislocation binding enthalpy. A softening effect caused by hydrogen was observed in both dynamically charged and precharged aluminum specimens as discussed in Sections 4.2.1 and 4.3.1. From the form of the stress-strain curves we concluded that the effect was due to a reduction in the strain hardening rate and hence any explanation should consider the dislocation cutting process which occurs as a result of interactions of dislocations on different slip systems. We propose the following mechanism to account for the hydrogen-related strain hardening reduction: i) moving dislocations sweep hydrogen-vacancy pairs from the lattice and they diffuse to the jogs; ii) a) dislocation jogs produce interstitials as the dislocations move. In the presence of hydrogen, hydrogen-vacancy pairs at the jog dissociate; the vacancies annihilate at the jog allowing the jog to move with dislocation without producing interstitials and hydrogen single atoms move with the dislocation; b) dislocation jogs produce vacancies as the dislocations move. In this case hydrogen-vacancy pairs exchange their place with atoms at the jog allowing the jog to move with the dislocation. The hydrogen-vacancy pairs stay behind, in the lattice and no vacancies are produced at the jog. The above mechanisms lead to a reduction in the jog dragging force. Jogs are expected to form as a result of the dislocation intersection reactions and therefore a reduction in the jog

dragging force is equivalent to a reduction in the latent hardening of non-coplanar slip systems. This should lead to slip on each system persisting for a larger amount of deformation before it ceases due to interactions with dislocations on intersecting slip systems. Hence, a coarser slip structure is expected in the presence of hydrogen than in the uncharged material. This coarse slip relief on the precharged specimen surfaces was observed as discussed in Section 4.3.2 as was increased amount of slip line waviness and cross-slip. The rate limiting step in the proposed mechanism of softening is hydrogen-vacancy diffusion along dislocations. This process is expected to be rapid due to enhanced vacancy diffusion along dislocations. The vacancy migration enthalpy along dislocations, 0.2 eV (82) is much lower than that in the perfect lattice, 0.62 eV (84) or 0.66 eV (80). The reduction in the jog dragging force does not account for the enhanced cross slip. The reason for the latter apparently stems from the increase in the vacancy concentration in presence of solute hydrogen. As was mentioned in Section 5.2., H_B(H-Vac) = 0.5 eV leads to a vacancy supersaturation of 2×10^3 per 1 appm of solute hydrogen. These vacancies are trapped by hydrogen but the complex should be easily dissociated by reactions with the dislocations since H_B(H-Vac) < H_f(Vac) and vacancies are consumed by dislocations in the non-conservative slip process. In addition to an increase in this "equilibrium" vacancy concentration, there should be an additional vacancy supersaturation due to the vacancy production by moving dislocation jogs. Since these vacancies can also interact with hydrogen, annihilation of these vacancies at jog sinks should be reduced by the trapping at hydrogen atoms as the thermodynamic driving force for the vacancy anneal is reduced. The reduced vacancy annihilation rates follow from the expression

$$\frac{dC_v}{dt} \propto (C_v - C_e)$$

where C_v is the vacancy concentration and C_e is the equilibrium vacancy concentration. Since C_e is increased by the presence of hydrogen atoms by several orders of magnitude, the rate of disappearance of the supersaturated vacancies should slow down significantly in the presence of hydrogen atoms.

Softening effects in aluminum due to hydrogen have not been previously reported. There are however published results which are consistent with the softening effect. Many investigators have reported a drop in the flow stress of aluminum when the surface layer was removed by electropolishing (65). Strain hardening reductions were observed in all three stages of plastic deformation. These results were generally interpreted in terms of the removal of surface hardened layers. We found in our study that electropolishing caused significant hydrogen charging by the aluminum. Assuming that electropolishing caused hydrogen charging in other studies as well, the observed softening effects may be associated with the hydrogen introduced by electropolishing.

5.5 Influence of Hydrogen on the Fracture Behavior

Crack nucleation and propagation took place in the range of general macroscopic plastic instability which occurred after large plastic deformation whether hydrogen was introduced dynamically, during the tensile test or precharged. This observation strongly suggests that the effect of hydrogen on the mechanism of fracture lies in its effect on the plastic deformation process. The stress state during plastic instability does not appear to play a significant role in the process of fracture. While triaxial stresses are generated as a result of necking, the degree of necking is small in the

aluminum sheet speciments. Furthermore, notches of different sharpnesses did not cause cracking before the onset of macroscopic plastic instability. As discussed in Section 4, the width of the plastic deformation region around a propagating crack was significantly reduced in the hydrogen charged specimens. Cracks propagated close to the edge of the slip bands. Whereas a chisel point type of fracture was common for tensile specimens free of hydrogen, fracture in hydrogen charged specimens was accompanied by a significantly smaller reduction in area and the slower the strain rate, the smaller the reduction in area was. Fracture paths were commonly transgranular but intergranular fracture was also observed. Some intergranular fracture occurred in dynamically charged specimens strained at the three slowest strain rates used and in the precharged and then cold rolled tensile specimens. The morphology of the transgranular fracture depended on both strain rate and grain orientation relative to the tensile axis. At the faster strain rates the fracture mode appeared to be similar to the dimpled rupture type. Hydrogen charging did not change the amount of macroscopic deformation preceding development of necking.

It appears that localization of plastic deformation is related to the fracture process. A great deal of attention has recently been directed towards the plastic instability induced fracture under flow localization conditions and the possible role of hydrogen in this process is reviewed in Ref. (83). According to this model, shear band development first precedes and then activates the fracture process. The strain localization begins after significant homogeneous plastic deformation. The role of hydrogen in the plastic instability development is still unclear, however, such phenomena as hydrogen induced reduction in strain hardening and void nucleation appear to

be very important. The role of hydrogen on the void nucleation process was studied mainly on steels. There is a controversy about the amount of general plastic deformation preceding hydrogen induced void nucleation. According to the recent studies, void nucleation starts after the onset of necking, giving rise to the fast local plastic instability development and triggering fracture. When the void nucleation process starts, it develops and is rapidly followed by fracture; making experimental observation of the hydrogen induced void formation difficult. The nature and distribution of second phase particles is very important in the process of hydrogen induced plastic instability.

As was mentioned in Section 5.2 hydrogen supersaturation in aluminum exerts a strong thermodynamic driving force for void nucleation. The void nucleation does not appear to occur during uniform deformation; if it did, an earlier onset of necking would occur in hydrogen charged specimens compared to uncharged specimens. Earlier development of necking did occur when charged specimens were annealed at 300 and 350°C prior to the tensile test; in this case hydrogen bubbles presumably formed in these anneals. To test the assumption that hydrogen induces void formation close to onset of fracture a type I specimen noched from both sides has been tested in the following sequence; slow strain rate (displacement rate = 1.25×10^{-5} mm/sec) tension was applied with an applied negative potential relative to a Pt electrode in ultrasonic water bath until necking began and cracks started from the two opposite notches. At this point the specimen was dismantled and taken for SEM observation. An intense shear band developed between the two cracks as shown in Figures 61 and 62. After the SEM observation the specimen was fractured at a very fast strain rate and very large dimples were observed on the fracture surface as shown in Figure 63. This fracture surface differs from other specimens which

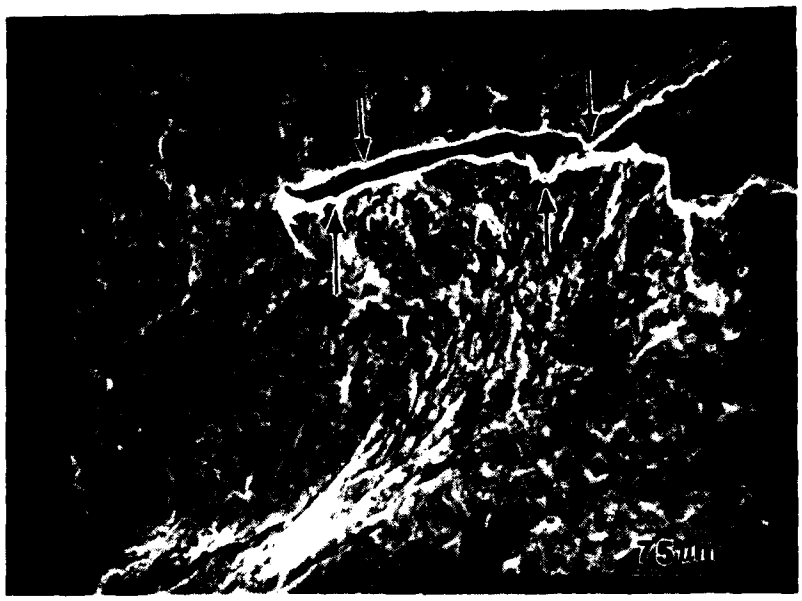

Fig. 62. Area "A" from Fig. 61. Notice the intense slip band matching points on the opposite crack surfaces are marked with arrows. The shift along crack path between the matching points suggests local mode II deformation whereas the specimen was strained in mode I. The small crack opening is consistent with this suggestion.

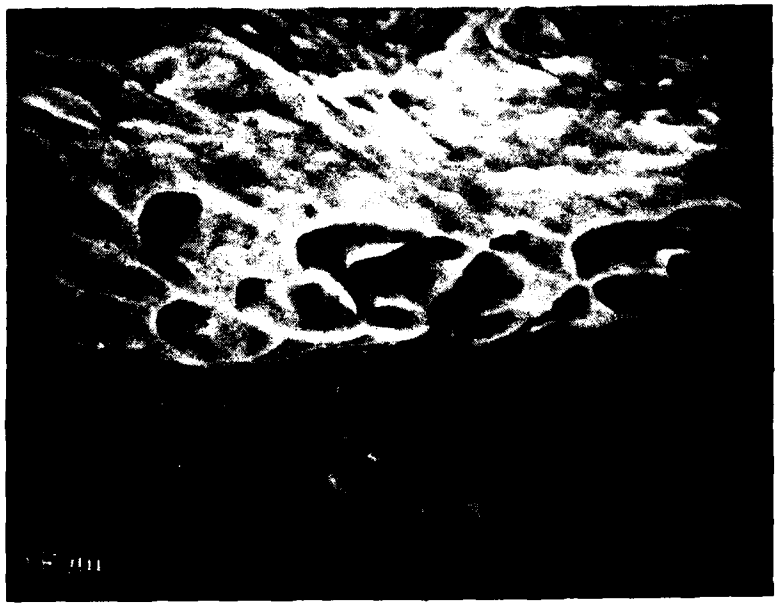

Fig. 63. Specimen tested in two stages as described in text. Well developed dimples are seen.

were hydrogen charged or uncharged and tested at the fast strain rates; these all exhibited a chisel type of fracture like that seen in Figure 51. All uncharged specimens of type I tested at the slow strain rate equal to that used in the above test also gave rise to chisel point fracture. The above test suggests that hydrogen induced void formation occurred before the fast straining stage.

As was discussed in Section 4.2.2 the fracture appearance of the dynamically charged specimens was sometimes flat apparently suggesting that a process other than microvoid coalescence governed the fracture process. However, it was shown by Lynch (40) that even cleavage like fracture in Al-6%Zn-3%Mg obtained in LME was composed of shallow dimples. Based on the experimental observations it appears that the fracture mechanism in our tensile tests with hydrogen charged specimens was governed by void nucleation, growth and coalescence processes. The presumed role of hydrogen in the void nucleation process was already discussed. It is possible that hydrogen facilitates both void growth and coalescence processes in aluminum due to its softening effect as was found in the present study. The coalescence process can be also accelerated by the new microvoid formation along shear band between growing voids.

As was mentioned in Section 2, an alternative fracture mechanism based on hydride formation was proposed (71,72). A feature on the fracture surface which was suggested to be an aluminum hydride was found on fracture surfaces of hydrogen precharged specimens. It had the appearance of a film and was sometimes fragmented by a crack network. As was discussed earlier in Section 4.5., x-ray diffraction patterns were obtained from the surfaces of either precharged sheets or during the hydrogen charging in NaOH solution. Hydride

formation at the surface should be facilitated by the high hydrogen concentration and by the ease of stress relaxation due to the lattice mismatch between aluminum and aluminum hydride. However, only aluminum diffraction peaks were found and no evidence was obtained for hydride formation.

Fracture surface having a filmed appearance was often found in the present study. The formation of the filmed fracture surfaces was facilitated by decreasing the strain rate in dynamically charged specimens. It occurred both on transgranular and intergranular portions of the fracture but was more often observed on the grain boundaries fracture facets. The occurrence of the filmed fracture was much more common in double cantilever beam specimens made from 0.25 mm thick sheets than in type I specimens used in dynamical charge tests. The crack network pattern was always different on the matching fracture surfaces as shown in Figure 24. In the hydrogen precharged specimens, filmed fracture surfaces were common in the large grain size specimens in both uncharged and hydrogen precharged conditions not found in the precharged small grain size specimens (uncharged small grain size specimens fractured in completely ductile chisel type of fraction). In many cases the filmed product was found on fracture surfaces which had the appearance of a mechanically damaged surface. Very often unfilmed pyramidal elevations and depressions on the filmed surfaces were found. The lock-in correspondence between these features was found on the matching fracture surfaces. These features appeared to have formed after the occurrence of mechanical damage on the surrounding filmed areas as was discussed in Section 4.2.2. In some cases a black "product" was observed to be spreading out of the crack tip during the tensile test of large grain size precharged specimens. The last three observations suggest that the film product

formation relates to the wear process between opposite fracture surfaces.

Smooth metal surfaces fragmented by the network of fine cracks or surfaces with a flaking appearance are common observations in wear processes including small amplitude wear; fretting (66,67). The smooth surface is formed by the smearing out of the debris. The wear product in aluminum and its alloys is black and contains about one fourth metallic aluminum and three fourths of oxide. The oxide is either amorphous alumina or cubic γ-alumina as based on two studies (67). Adhesion and cold welding between the surfaces are very important at the first stages of the process. Surface delamination and flaking then proceed. Flakes are often transferred between two opposite surfaces during wear.

The reasons for wear processes between fracture surfaces are poorly understood and we will consider several possibilities. As was shown (68) ductile cracks propagate by alternative shear and by void growth processes. This alternative shear could in principle cause fretting action on surfaces behind the crack tip. Such "fretting" would be most likely if the crack opening is suppressed as would occur when small cracks form ahead of the main one or when a crack front advances by smaller cracks penetrating ahead of the main crack. Another possible action causing surface wear is mode II or mode III type of crack loading. While the tensile specimens were loaded in mode I, mode III was clearly seen in the 0.25 mm thick double cantilever beam specimens due to their lack of rigidity. While a clear indication of a mode II component was not available, two observations suggest its occurrence during the crack propagation. First, substantial offset was often seen at the crack root in the precharged type II specimens (in these cases cracks were inclined

to the tensile axis). Secondly, matching features on the opposite fracture surfaces were in some cases shifted along crack path as shown in Figure 62. Finally, the reason for the fretting motion may stem from the vibrations in the testing equipment. Two types of vibration were present in the MTS machine, one due to the hydraulic pump and second was applied to overcome frictional forces in the machine especially during slow straining.

The role of hydrogen in promoting fracture surface damage resides in the localization of plastic deformation at the crack tip and therefore, in the reduction of the crack opening displacement. The second possibility lies in the hydrogen induced softening effect. As we could see from the tensile tests, the larger the strain, the more pronounced softening is. In the wear process the extent of the deformation attained is much higher than the average strain in the tensile test and more softening is expected. The softer the material is the more it is prone to adhesive wear (66). It may be interesting to investigate the use of hydrogen softening effects in industrial cold welding processes. Also it is expected that hydrogen reduces resistance of aluminum against wear.

Filmed surfaces were commonly observed in stress corrosion failures (69,70) and in hydrogen preembrittled specimens (29,54,71,72) of aluminum base alloys. The film products were identified as amorphous aluminum oxide or hydroxide (69). Aluminum with some γ-Al_2O_3 (70), aluminum hydride (72), aluminum (71) and boehmite with diaspore, mixture of aluminum hydroxide and oxide (54). In reference (71) a suggestion was made that the filmed product was originally aluminum hydride that decomposed to aluminum. The method of identification of the film product was the same in (70) and (71), electron diffraction pattern from the fracture knife edges. Despite that in the former

case stress corrosion fracture was investigated, in both studies an almost exclusively aluminum diffraction pattern was reported. The diffraction pattern was of the polycrystalline type for the hydrogen embrittlement fracture; an observation that could not be explained in view of the small diameter of the electron beam. Unfortunately no information of this type has been given in the case of stress corrosion fracture. There are number of additional difficulties in interpretation of observations made in the studies (54,71,72), which stem from the assumption that the filmed product existed in the metal prior to the mechanical test. These difficulties, mainly pointed out by the investigators themselves are a) mechanical properties can be totally recovered by a re-heat treatment process; b) mechanical properties can be restored totally or partially by the use of a fast strain rate; c) no film products were found in internal structure of material; d) film product are more voluminous than the host lattice, however, no wedge effect like that in exfoliation corrosion was found.

All these difficulties are resolved in a self evident way if fracture surface wear approach is taken. The only evidence in favor of the aluminum hydride nature of the film product is an observation of a diffraction pattern claimed to correspond to aluminum hydride. Some doubts about this finding exists. As pointed out by Tuck (54), lines reported by Ciaraldi (72) are in the range shared by number of different substances. Another point refers to the fact that aluminum hydride is very unstable in TEM observation and decomposes totally in 20-50 seconds (27), whereas the film product was stable during the TEM study in (72).

6. SUMMARY AND CONCLUSIONS

1. Pure aluminum absorbs large amounts of hydrogen, in excess of 1,000 appm, during corrosion in aqueous corrosive environments; especially in the alkaline range.
2. There is indirect evidence that hydrogen introduced by corrosion is bound with lattice vacancies in aluminum. Evidence for this is bulk vacancy clusters and a decrease in the length of aluminum during a corrosion reaction in an alkaline solution. Vacancies are produced in the corrosion reaction and additional evidence for this is grain growth during the hydrogen charging.
3. The rate of hydrogen degassing from aluminum which was charged by corrosion is extremely low at temperatures up to 300°C.
4. Absorbed hydrogen alters the plastic deformation behavior of pure aluminum as can be observed on both the macroscopic and microscopic scale. Hydrogen causes softening due to a reduction in strain hardening. The softening is increasingly pronounced as the amount of plastic deformation increases. Hydrogen causes localization of plastic deformation. This effect manifests itself macroscopically in coarse slip band formation in hydrogen precharged tensile specimens and in a narrowing of the plastic deformation region adjacent to a propagating crack in double cantilever beam specimens. The plastic localization effect is also seen as a coarsening of slip lines and an increase in their spacing. In addition to the slip structure coarsening hydrogen precharged specimens show more wavy slip pattern indicating greater extent of the cross slip than in uncharged aluminum.

5. Absorbed hydrogen did not cause an earlier onset of localized deformation, i.e. necking. A decrease of the extent of uniform plastic deformation was observed for specimens annealed at 600°C followed by hydrogen charging and then by anenaling at 300°C or at higher temperature. This decrease in the uniform strain did not occur when the final annealing temperature was 200°C or lower.
6. Absorbed hydrogen did not cause a reduction in amount of plastic deformation in precharged tensile specimens during necking development. This is believed to be a result of the fact that the fracture process occurred only at final stage of the necking development. The amount of macroscopic plastic deformation in the necking stage was reduced when hydrogen was charged dynamically, i.e. during tensile test. Fracture in this case started shortly after onset of localized necking.
7. Fracture of either charged or uncharged tensile specimens always occurred during plastic instability even in specimens which were pre-notched. The amount of plastic deformation during crack propagation was reduced by the absorbed hydrogen as judged from the reduction in area of the fracture surface of the tensile specimens. The slower the strain rate the greater the extent of the "brittle" fracture. The morphology of the fracture surface changes from a chisel point fracture in uncharged specimens to transgranular and/or intergranular fracture in hydrogen charged specimens. Transgranular fracture was observed more commonly in these hydrogen charged specimens.
8. Macroscopic hydrogen embrittlement which manifested itself as a reduction in the amount of necking preceding fracture, as a reduction of

macroscopic plastic deformation during fracture, and as a change in fracture morphology is consistent with a plastic deformation modification mechanism and is not consistent with lattice decohesion theory and with hydride induced brittleness.

9. The film that sometimes covered fracture surfaces and that often was fragmented by a crack network (mud crack pattern) is a post fracture phenomenon believed to be a result of adhesive wear between fracture surfaces.

REFERENCES

1. C.E. Ransley and H. Neufeld, J. Inst. Metals, 74, 599 (1948).
2. W.R. Opie and N.J. Grant, Trans. AIME, 188, 1237 (1950).
3. W. Eichenaeur, Z. Metallkunde, 59, 613 (1968).
4. M. Ichimura, M. Imabayashi and M. Hayakawa, J. Jpn. Inst. Met., Vol. 43, 9, 876 (1979).
5. W. Eichenauer and J. Markopolous, Z. Metallkunde, 65, 649 (1976).
6. C.E. Ransley and D.F. Talbot, Z. Metallkunde, 46, 326 (1955).
7. K. Papp and E. Kovacs-Csetenyi, Scripta Met., 15, 161 (1981).
8. A. Csanady, K. Papp and E. Pasztor, Mat. Sci. and Eng., 48, 35 (1981).
9. R.A. Outlaw, D.T. Peterson and F.A. Schmidt, Scripta Met., 16, 287 (1982).
10. E. Hashimoto and T. Kino, J. Phys. F, Met. Phys., 13, 1157 (1983).
11. L.A. Andreev et al., Izv. Vuz. Cvetn. Met., 5, 123 (1975).
12. K. Papp and E. Kovacs-Csetenyi, Scripta Met., 11, 92 (1977).
13. L.M. Foster, T.H. Jack and W.W. Hill, Met. Trans., 1, 3174 (1970).
14. R.A.H. Edwards and W. Eichenauer, Scripta Met., 14, 971 (1980).
15. D.S. Larsen and J.K. Norskov, J. Phys. F, Met. Phys., 9, 1975 (1979).
16. H.F. Ades, A.L. Companion, Solid State Commun., Vol. 48, 4, 337 (1983).
17. J.P. Bugeat and E. Ligeon, Phys. Lett., 71A, 93 (1979).
18. Y. Shimomura, K. Yamakawa, K. Kitagawa and H. Oda, in "Point Defect Interactions in Metals," p. 712, Yamada Science Foundation, 1982, University of Tokyo Press.
19. R.J. Gest and A.R. Troiano, Corrosion-NACE, Vol. 30, 8, 274 (1974).
20. J. Albrecht, I.M. Bernstein and A.W. Thompson, Met. Trans., 13A, 811 (1982).
21. Y. Shimomura and S. Yoshida, J. Phys. Soc. Jpn. 22, 319 (1967).

22. M.L. Sundquist and J.M. Donhowe, Nucl. Tech., 30, 4 (1976).

23. S.K. McLaurin, G.L. Kulcinski, J. Nucl. Mater., 117, 208 (1983).

24. M. Victoria, W.V. Green, B.N. Singh and T. Leffers, J. Nucl. Mater., 122,123, 737 (1974).

25. J.W. Turley, H.W. Rinn, Inorganic Chemistry, 8, 18 (1969).

26. P.J. Herley, O. Christofferson and R.H. Irwin, J. Phys. Chem., 85, 1874 (1981).

27. P.J. Herley and W. Jones, J. Mat. Sci. Lett., 1, 163 (1982).

28. M. Appel and J.P. Frankel, J. Chem. Phys., 42, 3984 (1965).

29. S.W. Ciaraldi et al., in "Hydrogen Effects in Metals," I.M. Bernstein and A.W. Thompson, eds., TMS-AIME, p. 437 (1981).

30. J.C. Scully, in "Treatise on Materials Science and Technology," vol. 23, Academic Press, (1983) p. 103.

31. M.H. Kamdar, ibid. p. 362.

32. W.J. Barnett, A.R. Troiano, J. Met. Trans. AIME, 209, 486 (1957).

33. C.D. Beachem, Met. Trans., 3, 437 (1972).

34. J. Eastman et al., Acta Met., 30, 1579 (1982).

35. T. Tabata and H.K. Birnbaum, Scripta Met., 18, 231 (1984).

36. I.M. Robertson et al., Scripta Met., 18, 841 (1984).

37. J. Eastman et al., in "Hydrogen Effects in Metals," I.M. Bernstein and A.W. Thompson, eds., AIME, Warrendale, PA, 1980, p. 397.

38. D.G. Westlake, Trans. ASM, 62, 1000 (1969).

39. L. Peeters et al., Mem. Sci. Rev. Met., 69, 81 (1972).

40. W. Rostoker et al., "Embrittlement by Liquid Metals, " Van Nostrand Rheinhardt, New York, 1960.

41. S.P. Lynch, Acta Met., 28, 325 (1981).

42. R.B. Mears, Symp. on Stress Corrosion Cracking of Metals, ASM, 1945, Philadelphia.

43. L. Montgrain, P.R. Swahn, "Hydrogen in Metals," I.M. Bernstein and A.W. Thompson, eds., 1974, p. 575, ASM, Metals Park.

44. J.A.S. Green et al., in "Effects of Hydrogen on Behavior of Metals," I.M. Bernstein and A.W. Thompson, eds., 1976, p. 200, AIME, New York.

45. M.D. Speidel, in "Hydrogen in Metals," ASM, 1974, p. 249.

46. M.D. Speidel, Met. Trans., 6, 631 (1975).

47. N.J.H. Holrody and D. Hardie, Corros. Sci., 21, 129 (1981).

48. M.R. Louthan et al., Mater. Sci. Eng., 10, 357 (1972).

49. M.R. Louthan, Jr. and A.H. Dexter, Met. Trans., 6A, 1655 (1975).

50. J.E. Draley and W.E. Ruther, Corros., 12, 480t (1956).

51. G. Bond et al., "The Influence of Hydrogen on Deformation and Fracture Processes in High-Purity Aluminum," to be published.

52. G.M. Scamans, J. Mater. Sci., 13, 27 (1978).

53. R. Alani and P.R. Swann, Br. Corros. J., 12, 80 (1977).

54. C.D.S. Tuck, Met. Trans., 16A, 1502 (1985).

55. M. Pourbaix, "Atlas of Electrochemical Equilibria in Aqueous Solutions," Pergamon Press, 1966.

56. R.W. Balluffi, in "Grain Boundary Structure and Kinetics," 1982, p. 297, ASM.

57. H. Peisl, p. 53 in "Hydrogen in Metals I" ed. by G. Alefeld and J. Volkl, Springer-Verlag (1978).

58. H.Q. Lam, H.A. Hoff, P.R. Okamoto and R.W. Siegel, Acta Met., 27, 799 (1979).

59. Encyclopedia of Electrochemistry of the Elements, (A.J. Bard, ed.), Vol. VI, Chap. VI-3, Marcel Dekker, Inc.

60. F.T. Klimowicz and R.M. Latanision, Met. Trans., 9A, 597 (1978).

61. M.V. Speight in "Vacancies '76,", p. 118. The Metal Society (1977).

62. T. Isikawa and R.B. McLellan, Acta Metall., Vol. 34, No. 6, 1091 (1986).

63. G. Bond et al., "Sub-threshold electron irradiation damage in hydrogen-charged aluminum," to be published.

64. L.A. Andreyev and A.F. Vytkin, Fiz. Metal. Mealloved., 49, No. 3, 611 (1980).

65. S.J. Basinski and Z.S. Basinski in Dislocation in Solids (F.R.N. Nabarro, ed.), Vol. 4, p. 278 (1979).

66. R.B. Waterhouse, "Fretting Corrosion," Pergamon, Oxford (1972).

67. R.B. Waterhouse, "Fretting," in "Treatise on Material Science and Technology, " Vol. 13, Academic Press (1979).

68. H.G.F. Wilsdorf, Scripta Met., 17, 1209 (1983).

69. D.A. Meyn, Corrosion-NACE, Vol. 26, No. 10, 427, October (1970).

70. W.R. Middleton and R.N. Parkins, Corrosion-NACE, Vol. 28, No. 3, March (1972).

71. J.L. Nelson, PhD thesis, Urbana, Illinois (1976).

72. S.W. Ciaraldi, PhD thesis, Urbana, Illinois (1980).

73. K.M. Miller and P.T. Heald, Physica Status Solidi (b), 67, 569 (1975).

74. R. Bullough and J.R. Hardy, Phil. Mag., 17, 833 (1968).

75. T.H. Nguen and R.T. Foley, J. Electrochem. Soc., 126, 1855 (1979).

76. R.S. Alwitt. Oxides and Oxide Films, Vol. 4 (Ed. J.W. Diggle and A.K. Vijh), p. 169, Marcel Dekker, New York (1976).

77. R.C. Furneaux et al, Corros. Sci., 18, 853 (1978).

78. F. Besenbacher, S.M. Myers and J.K. Norskov, cited in (62).

79. R.W. Siegel, J. Nucl. Mater. 69-70, 117 (1978).

80. K. Ono and T. Kino, J. Phys. Soc. Japan, Vol. 44, No. 3, 875 (1978).

81. American Institute of Physics Handbook, Third Edition, McGraw-Hill..

82. K. Sassa, W. Petry and G. Vogl, Phil. Mag. A, Vol. 48, No. 1, 41 (1983).

83. O.A. Onyewuenyi, in Hydrogen Degradation of Ferrous Alloys (R.A. Oriani, J.P. Hirth, M. Smialowski eds.) Noyes Publications (1985).

84. H. Ullmaier and W. Schilling, Physics of Modern Materials, IAEA-SMR-46/105 (Vienna: International Atomic Energy Agency), 301 (1980).

Appendix A

Hydrogen Absorption During Electropolishing

Electropolishing in a perchloric acid solution (Section 3.4) was employed for macroscopic electropolishing at temperatures of about -15°C. Platinum wire was used as a cathode with a potential drop of about 30 V between the electropolished specimen and the cathode. Direct evidence from hydrogen analyses and indirect evidence from observed decreases in the flow stress of tensile specimens and from the blistering of thin electropolished sheets, showed that electropolishing was accompanied by hydrogen charging of the aluminum. About 300 appm of hydrogen was found in 0.5 mm thick tensile specimens electro-polished for 3-4 min.

Surface blistering developed during SEM observation of electropolished thin (less than 0.1 mm thick) sheets of aluminum. Blisters formed in less than one minute of observation under the SEM electron beam (25 kV) held on the same spot on the specimen surface. When nearby blisters grew they merged giving rise to large size blisters as shown in Figure A1. Blister formation is assumed to result from the surface heating of the hydrogen charged surface by the electron beam. It is not generally observed if the electron beam is rastered across the usual specimen area. In thicker electropolished sheets fine network of cracks formed and grew during the SEM observation as shown in Figures A2 and A3. The crack pattern was sometimes formed very quickly, but usually required maintaining the electron beam on the same spot for several minutes. No cracks or blisters were observed in the optical microscopic examination before SEM observation nor were any seen at the beginning of the SEM observation. The nature of the cracks is unclear. If hydrated oxide

formed during electropolishing, cracks could form due to its dehydration under the SEM electron beam. Cracks, however, were not observed in the optical microscope after the electropolished surface was locally heated to about 200°C using a localized electrical heater. Figures A4 and A5 show a case where cracks were observed in the blister shell. Blisters first formed and grew under the SEM beam. Other areas of the same sample were then studied. When the beam was returned to the original areas, the blister shell was found to be cracked and to have collapsed onto the specimen surface.

Hydrogen charging during electropolishing is not a phenomenon exclusively confined to electropolishing in perchloric acid solution as can be seen from the following example. Two 0.25 mm thick aluminum sheets were placed in an alkaline (NaOH) solution with pH 12 and a potential difference of 4 V was applied between them. After overnight exposure we found the surface of the anodic sheet to be "mirror-like" i.e. electropolishing took place. Hydrogen analyses of the anodic sheet showed 1,570 appm of hydrogen.

Figure A1. Blisters formed under an electron beam on the surface of thin electropolished sheet. The largest blister in the center formed by the merging of smaller ones.

Figure A2. A crack network formed on the surface of electropolished sheet under SEM electron beam.

Figure A3. Area "A" in Figure A-2 at higher magnification.

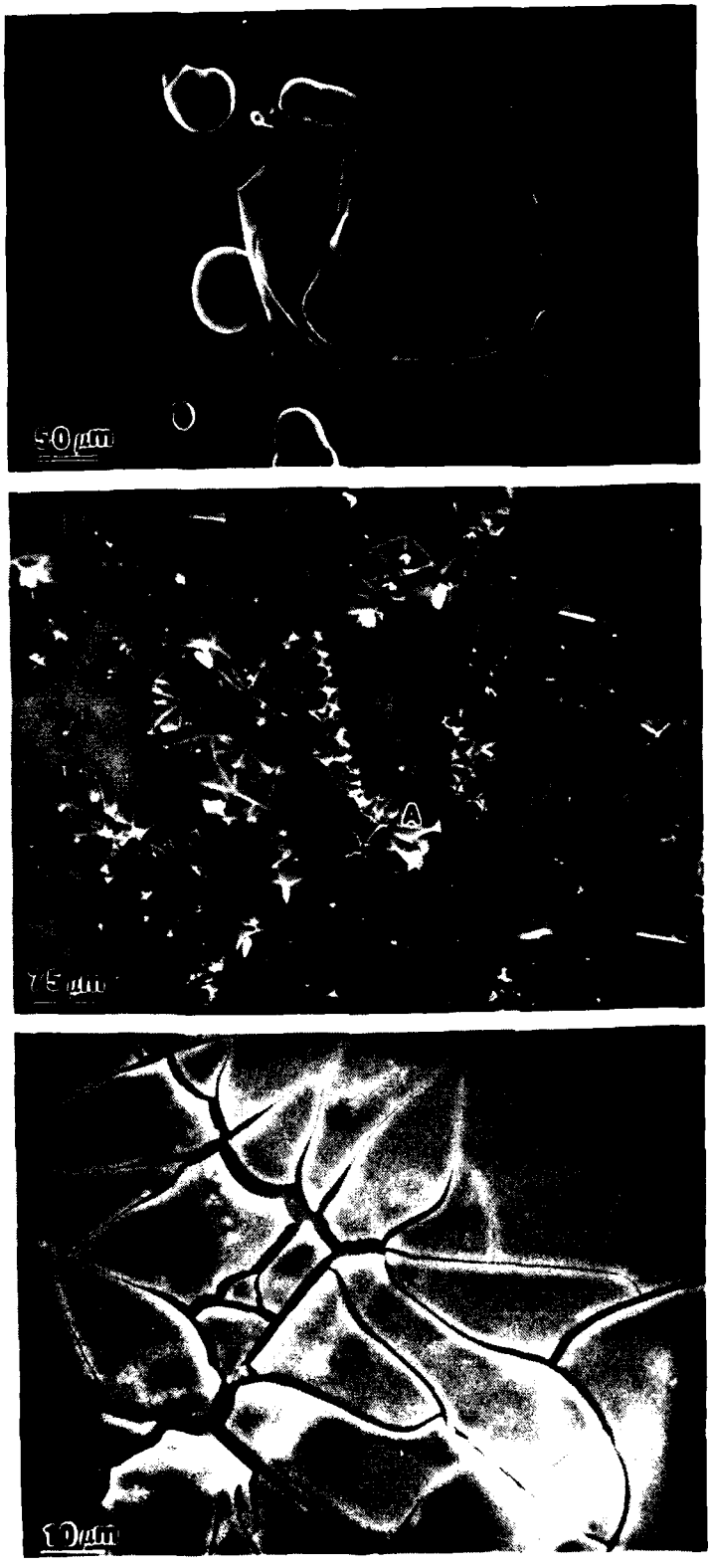
50 μm
A
75 μm
10 μm

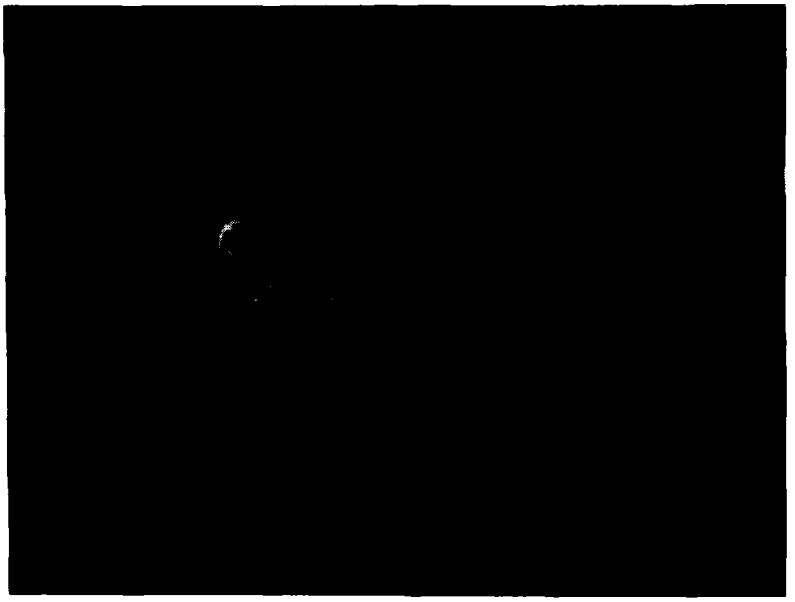

Figure A4. A group of merged blisters formed and grown under the SEM beam.

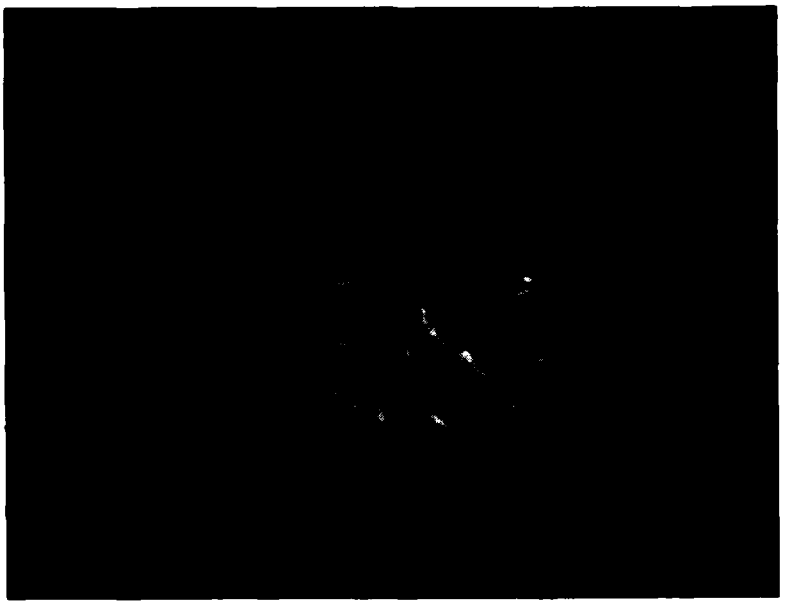

Figure A5. Same area as in Figure A4. Other areas were observed for about 30 min after the blister formation and before the SEM beam was returned to this area. Multiple cracks had formed in the collapsed blister shell in the interim period.

Appendix B

Localized Aluminum Dissolution

One group of the Type I tensile specimens was slowly extended until fracture in an ultrasonic bath with a cathodic potential of 10 V relative to a Pt anode applied to the specimens. Long, branched tunnels developed from the side surfaces and these were exposed on the fracture surface when a crack propagated through the tunnels. Typical examples are shown in Figures B1 and B2. The increase in alkalinity of the corrosive solution resulting from a cathodic reaction is a known phenomenon, see, for example, (60), and was also observed in the present work. Alkalinity increases presumably due to the following reactions (60):

$$O_2 + 2H_2O + 4\mathrm{I} \rightarrow 4OH^-$$

or

$$2H_2O + 2e \rightarrow H_2 + 2OH^-.$$

We assume that the tunnel's formation resulted from alkaline local attack and from the surface film disrupture by ultrasonic field. When aluminum sheets are used to produce capacitors, pitting is introduced on purpose to increase surface area and, hence, capacitance. It seems interesting to investigate the observed tunnel formation phenomenon for this purpose.

Figure B1. Fracture surface of the specimen tested in ultrasonic water both under a cathodic potential. Branched tunnels are marked with arrows.

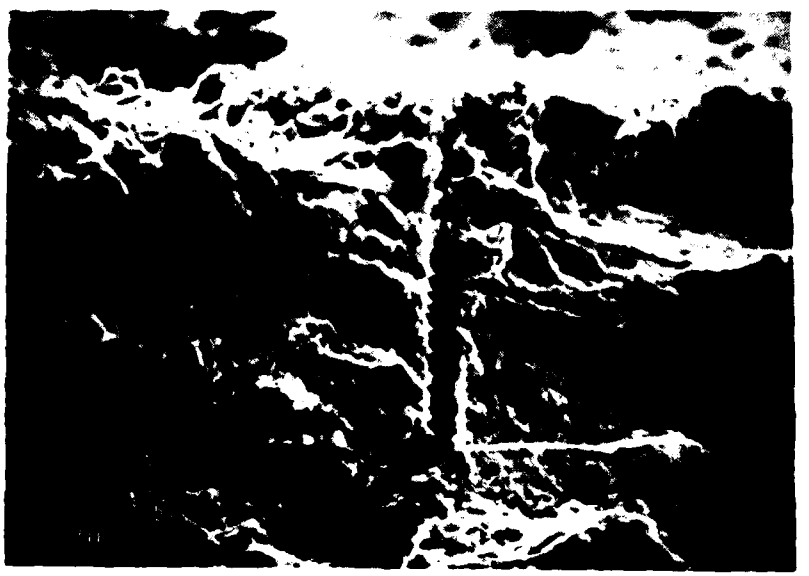

Figure B2. The fracture surface opposite to that shown in Figure B1.

VITA

Felix Zeides was born on July 22, 1948 in Simferopol, USSR. He graduated from the Polytechnical Institute of Tomsk, USSR as a metallurgical engineer in June, 1972 and then worked for two years as an industrial engineer. In 1974 he emigrated to Israel where he worked until 1982 in an aircraft industry. Since 1982 he has been a graduate student in the Department of Metallurgy and Mining Engineering at the University of Illinois.

He is co-author of the following publications:

1. "Sub-Threshold Electron Irradiation Damage in Hydrogen-Charged Aluminum", G.M. Bond, I.M. Robertson, F.M. Zeides and H.K. Birnbaum, presented for publication in Phil. Mag. Journal.
2. "Some Recent Advances in the Field of Fatigue and Stress-Corrosion of Aluminum Alloys for Aircraft", B. Cina, T. Kaatz, F. Zeides, I. Eldror and B. Ranish, published in "Aluminum Alloys in the Aircraft Industries", Proceedings of a Symposium held in Turin 1-2 October, 1976.

Unclassified

SECURITY CLASSIFICATION OF THIS PAGE (When Data Entered)

ADA 171214

REPORT DOCUMENTATION PAGE		READ INSTRUCTIONS BEFORE COMPLETING FORM
1. REPORT NUMBER	2. GOVT ACCESSION NO.	3. RECIPIENT'S CATALOG NUMBER
4. TITLE (and Subtitle) Effect of Hydrogen on the Mechanical Properties and Fracture Behavior of High Purity Aluminum		5. TYPE OF REPORT & PERIOD COVERED Technical Report 6. PERFORMING ORG. REPORT NUMBER
7. AUTHOR(s) F. Zeides and H.K. Birnbaum		8. CONTRACT OR GRANT NUMBER(s) USN N 00014-83-K-0468
9. PERFORMING ORGANIZATION NAME AND ADDRESS University of Illinois, Dept. of Materials Science, 1304 W. Green St., Urbana, IL 61801		10. PROGRAM ELEMENT, PROJECT, TASK AREA & WORK UNIT NUMBERS
11. CONTROLLING OFFICE NAME AND ADDRESS Office of Naval Research, Materials Division, 800 N. Quincy St., Arlington, VA		12. REPORT DATE July 1986 13. NUMBER OF PAGES 126
14. MONITORING AGENCY NAME & ADDRESS(if different from Controlling Office)		15. SECURITY CLASS. (of this report) Unclassified 15a. DECLASSIFICATION/DOWNGRADING SCHEDULE

16. DISTRIBUTION STATEMENT (of this Report)

This document is unclassified. Reproduction and distribution is permitted for any purpose of the U.S. Government.

17. DISTRIBUTION STATEMENT (of the abstract entered in Block 20, if different from Report)

18. SUPPLEMENTARY NOTES

19. KEY WORDS (Continue on reverse side if necessary and identify by block number)

Aluminum
Hydrogen
Hydrogen Embrittlement
Fracture
Plastic Deformation

20. ABSTRACT (Continue on reverse side if necessary and identify by block number)

see reverse side

DD FORM 1 JAN 73 1473 EDITION OF 1 NOV 65 IS OBSOLETE
S/N 0102-LF-014-6601

Unclassified

SECURITY CLASSIFICATION OF THIS PAGE (When Data Entered)

#20

ABSTRACT

A study of hydrogen effects was conducted on 99.999% pure aluminum. Hydrogen was introduced into the material by means of a corrosion process. Two corrosive media were used; deionized pure water and an alkaline solution. The former was used for dynamic hydrogen charging during mechanical tests and the latter for hydrogen precharging. The corrosion reaction in the dynamic charging was intensified by application of weak ultrasonic oscillations.

It was found that hydrogen changed the response of the material to plastic deformation causing softening and plastic deformation localization on the macroscopic and slip line coarsening as well as an increase in their waviness on the microscale. Hydrogen did not cause an earlier onset of the macroscopic plastic instability, i.e. necking.

Hydrogen modified the fracture mode, changing it from a totally ductile, chisel point type to a more brittle transgranular or intergranular fracture. The fracture started only after the onset of necking. The hydrogen induced fracture modification is believed to result from the plastic deformation modification and from the effect of hydrogen on microvoid nucleation. Some fracture surfaces were covered with a film, that was occasionally fragmented by a network of cracks ("mud crack pattern"). This phenomenon is believed to be a post fracture effect caused by adhesive wear between opposite fracture surfaces.

Hydrogen charging resulted in the formation of bulk vacancy clusters, a linear dimensions shrinkage and grain growth. This was interpreted as evidence for vacancy production during the corrosion reaction and for a significant hydrogen-vacancy binding enthalpy.

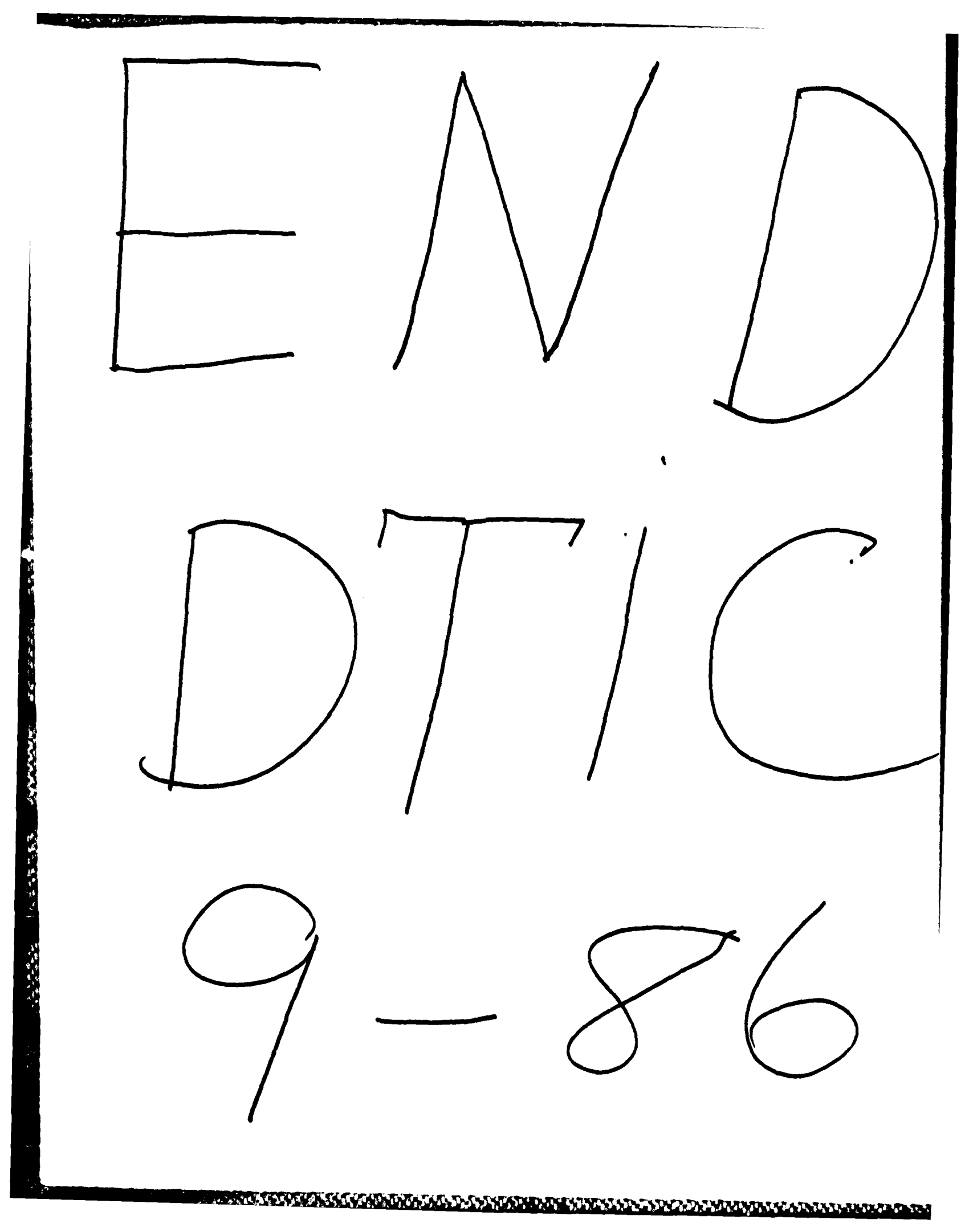
END
DTIC
9-86